True meaning of pseudocapacitors and their performance metrics: Asymmetric Vs Hybrid Supercapacitors

*Nilesh R. Chodankar,[1] Hong Duc Pham,[2, 3] Ashok Kumar Nanjundan, [3] Joseph F. S. Fernando,[2, 3] Kolleboyina Jayaramulu,[4] Dmitri Golberg,[2, 3] Young-Kyu Han,[1] Deepak P. Dubal [2, 3]***

Dr. Nilesh R. Chodankar and Prof. Young-Kyu Han
Department of Energy & Materials Engineering,
Dongguk University, Seoul, 100-715,
Republic of Korea

Dr. Hong Duc Pham, Dr. Joseph F.S. Fernando, Prof. Dmitri Golberg and Dr Deepak P. Dubal
Centre for Materials Science,
Queensland University of Technology (QUT),
2 George Street, Brisbane, QLD 4001, Australia

Dr. Hong Duc Pham, Dr. Ashok Kumar Nanjundan, Dr. Joseph F. S. Fernando, Prof. Dmitri Golberg and Dr Deepak P. Dubal
School of Chemistry and Physics, Queensland University of Technology (QUT),
2 George Street, Brisbane, QLD 4001, Australia
Email: dubaldeepak2@gmail.com, deepak.dubal@qut.edu.au

Dr. Kolleboyina Jayaramulu
Department of Chemistry, Indian Institute of Technology Jammu,
Nagrota Bypass Road, Jammu & Kashmir, 181221, India

This is the author manuscript accepted for publication and has undergone full peer review but has not been through the copyediting, typesetting, pagination and proofreading process, which may lead to differences between this version and the Version of Record. Please cite this article as doi: 10.1002/smll.202002806.

Abstract

The development of pseudocapacitive materials for energy-oriented applications have stimulated considerable interest in recent years due to their high energy-storing capacity with high power-outputs. Nevertheless, the utilization of nano-sized active materials in batteries leads to fast redox kinetics due to the improved surface area and short diffusion pathways, which shifts their electrochemical signatures from battery-like to the pseudocapacitive-like behaviour. As a result, it becomes challenging to distinguish "pseudocapacitive" and "battery" materials. Such misconceptions have further impacted on the final device configurations. This review is an earnest effort to clarify the confusion between the battery and pseudocapacitive materials by providing their true meanings and correct performance metrics. We have outlined a method to distinguish battery-type and pseudocapacitive materials using the electrochemical signatures and quantitative kinetics analysis. Taking solid-state supercapacitors (SSCs, only polymer gel-electrolytes) as an example, we have discussed the distinction between asymmetric and hybrid supercapacitors. The state-of-the-art progress in the engineering of active materials is summarized, which will guide for the development of real-pseudocapacitive energy storage systems.

Keywords- Pseudocapacitive materials, Battery materials, Asymmetric supercapacitor, Hybrid supercapacitor.

1. Introduction

The modern world is incomplete without the portable and wearable electronic devices that have transformed our lifestyles. For instance, mobile phones with several functions and applications, activity trackers (smartwatches and sensors), healthcare, and implantable medical devices (pacemakers, insulin pumps, and many more) have made our lives convenient.[1-3] Nevertheless, the increased energy consumption of these smart electronic devices obliges efficient energy storage systems. Notably, the supercapacitors (SCs), among diverse electrochemical energy storage (EES) systems pave a way towards the development of portable electronic appliances due to their high power and rate capability, long cycle and calendar life with safe-operations.[4-6] The traditional electric double-layer capacitors (EDLC) that store charges electrostatically at the electrode/electrolyte interface (a non-Faradaic process) enable excellent power-delivery compared to other devices such as batteries. Nevertheless, using the state-of-the-art carbonaceous materials, the SCs typically deliver high power densities (~15 kW/kg) with poor energy storage capability (5-10 Wh/kg), which restricts their further applications.[7-10] Several recent and upcoming applications, including electric vehicles and renewable energy storage, are in enormous demand for high energy besides the high-power supply.

In the pursuit of simultaneous high energy and high power devices, pseudocapacitive materials emerged into the picture with completely different electrochemical features where the current response is neither purely capacitive nor bulk Faradaic (like-batteries).[11-13] Yet, these materials undergo fast and reversible surface-controlled redox reactions at the electrode surface through either intercalation or adsorption of electrolyte-ions; therefore, they offer a pathway for achieving both high energy and high power densities. Although pseudocapacitive

materials display very high-rate capability similar to that of double-layer capacitive materials, they differ from EDLC due to the involvement of battery-like redox reactions for charge storage. Besides, they are distinct from traditional battery materials as the kinetics of the redox reactions are extremely fast and not limited by semi-infinite diffusion.[14] In other words, pseudocapacitors can be considered as a complementary form of EDLC despite not being electrostatic in origin. They display similar electrochemical signatures (cyclic voltammetry and charge/discharge profiles) to EDLC. Brousse and co-workers have very well explained the background and Conway's intention to use the word "pseudocapacitance" for labelling such materials.[15] Accordingly, the prefix "pseudo" with "capacitor" is used to describe the properties of an electrode that shows the features of a capacitor in its electrochemical signature (CV and CDs) and to differentiate them from EDLC in regards to the charge storage mechanism.

Nonetheless, the recent advancements in nanotechnology enable the utilization of nanomaterials in energy storage systems, especially in batteries (electrodes) as a route for increasing power density. This size reduction (nano-structuring) improves the surface area of the materials, shortens the ion diffusion lengths, and sometimes suppresses the phase transformations in battery materials.[16] As a result, the electrochemical signatures of such battery materials in the bulk-state shift to pseudocapacitive outputs (quasi-rectangular CV and quasi-triangular CD curves). Studies have shown that crystal structures, surface functionalization, or interfacial effects may contribute to pseudocapacitance creating new challenges and misunderstandings about the battery and pseudocapacitive materials.[17-19] New terminologies such as "intercalation pseudocapacitance" and "extrinsic pseudocapacitance" with methods to distinguish battery and pseudocapacitive materials are helpful to some extent. Still, many researchers unintentionally misunderstand them, creating more confusion in the scientific community.

This review attempts to clarify some of the confusions mentioned earlier, by providing different definitions of pseudocapacitance with their kinetic signatures and charge storing mechanisms. Also, it draws clear boundaries between pseudocapacitive and battery materials. It begins with the outline of the traditional supercapacitors such as EDLC and pseudocapacitors, followed by the true meaning of new terms such as extrinsic and intercalation pseudocapacitance with their electrochemical signatures. Later, the methods proposed to distinguish pseudocapacitive and battery materials accurately using quantitative kinetics analysis are outlined. To the end, the progress on the design and development of nanostructured electrode materials in both asymmetric and hybrid supercapacitors is summarized, taking solid-state supercapacitors as an example.

2. Details of charge storing mechanisms

Previous review articles have already provided accounts concerning the traditional charge storage mechanisms at the interface of the electrode/electrolyte and their fundamental electrochemistry [20-22], which is not the scope of the present article. Nevertheless, we have discussed the recent confusion about materials, their charge-storing mechanisms, and the terminology used in the SCs. It is known and understood that SCs store charges through two different mechanisms, such as electric double-layer (EDLCs) and pseudo-capacitance.[23] Thanks to the cutting-edge characterization techniques and theoretical modelling tools, we could differentiate the energy storage properties of the materials and categorise them appropriately. This section provides a guide to identify and differentiating rubrics of EDLC, pseudocapacitors and faradic energy storage systems.

2.1 Double-layer capacitors

Electric double-layer capacitor (EDLC) is the most common and thoroughly studied form of SCs where the capacitance arises due to the adsorption of both anions and cations at the electrode/electrolyte interface (Figure 1a)[24]. The capacitance of the EDLCs strongly

depends on the surface properties of the electrode materials (e.g. specific surface area and pore-size distribution) that is accessible to the electrolyte ions. During the charging process, the electrons move from the negative electrode to the positive electrode through the external loop, with anions moving to the positive electrodes. In contrast, the cations move towards the negative electrode. The moving direction of the electrons and ions would be reversed in the discharging process.[25,23] The Helmholtz model is the simplest model to describe this process as double-layer capacitance using the equation for a parallel plate capacitor:

$$C = \frac{\varepsilon A}{d} \qquad (1)$$

where C is the double-layer capacitance, ε is the permittivity of the dielectric separating the charges, A is the surface area of the electrode, and d is the distance between the electrode and electrolyte ions. Typically, carbon-based porous materials such as activated carbon,[26-28] xerogels,[29-32] carbon nanotubes (CNTs),[33-35] carbon nanofibers (CNFs),[36-38] graphene,[39-41] and carbide-derived carbons[42-44] show EDLC type behaviour owing to their high specific surface area and good conductivity. The charge/discharge process in EDLCs is associated with the purely non-Faradaic reactions; thus, responds immediately to potential changes. The electrochemical signatures of EDLC-based material are shown in Figure 1 (b, c). Cyclic voltammetry (CV) curves are rectangular-box-type in nature, while galvanostatic charge/discharge (GCD) profile shows a symmetric triangular pattern. The lower energy density values (especially volumetric energy density) for the carbon-based SC is the limitation for their successful practical implementation. Therefore, research needs to focus on the synthesis condition to enhance the performance-enhancing factors such as the specific surface area, surface energy, electrical conductivity and pore size distribution.

2.2 Pseudocapacitors

The term "pseudocapacitance" was firstly defined by Conway to describe the materials that exhibit electrochemical signatures (CV and CD) similar to those of traditional capacitors (EDLC), which however involve different charge storing mechanism.[15] Unlike EDLC, the pseudocapacitive reactions are faradic in origin and store electrical energy through fast and reversible redox processes at the electrode surface. In other words, pseudocapacitive materials exhibit battery-like redox reactions that happens at very high rates similar to a capacitor, and reflect their electrochemical features (quasi-rectangular CVs and quasi-triangular GCD curves).[9, 45] The charge storage mechanisms in pseudocapacitive materials can involve either i) at or near surface-redox reactions; or ii) intercalation-type reactions, which are briefly discussed in the following sections.

2.2.1 Surface redox or intrinsic pseudocapacitors

In surface-redox pseudocapacitors, the charge storage is mainly attributed to the charge transfers (or redox reactions) occurring at the surface of the electrode. As revealed from Figure 1d-f, the CV and the GCD profiles for surface-redox pseudocapacitors are closely resembling those of carbon-based materials (Figure 1a-c), suggesting the linear dependency of the charge storage along with the whole potential window. This does not mean that pseudocapacitors store the charges only via double layer mechanism. However, they can store the charges via surface faradic and double layer mechanism.[46] The materials exhibiting such in-build electrochemical features are referred to as intrinsic pseudocapacitive materials.[45] Various surface-redox pseudocapacitive materials such as transition metal oxides have been investigated since 1971. Trasatti and Buzzanca[47] first reported the pseudocapacitance of RuO_2 in SC. It is an intrinsic (redox) pseudocapacitive material due to the fast proton and electron-conducting properties. Likewise, other transition metal oxides such as MnO_2 and Fe_3O_4 are also exhibiting intrinsic (redox) pseudocapacitance. Owing to their multiple valence states, they can initiate the fast and reversible redox reactions at the

electrode surface, which makes them better than the EDLCs as they store much high energy at high charge-discharge rate. The charge storage mechanism and electrochemical signatures of redox pseudocapacitors are displayed in Figure 1 (e-f) with MnO_2 as an example where MnO_2 stores charges through the surface or bulk redox reactions in between the +4 and +3 oxidation states of Mn [48].

$$MnO_2 + xA^+ + xe^- \leftrightarrow A_xMnO_2 \quad (2)$$

In the above reaction mechanism, the symbol '*A*' embodies an alkali metal cation (Li^+, Na^+, K^+). The pseudocapacitive properties of Mn-oxides strongly depend on their crystallinity and crystallographic structures.[49] Based on the different arrangements of the MnO_6 octahedra, the Mn-oxides can be classified in the diverse crystalline structures such as α, β, γ, δ, and λ forms[50] where α, β, and γ phases have 1D tunnels, δ and λ show 2D layered and 3D spinel structures, respectively[51].

The different physical processes and the electrode materials are responsible for these two distinct mechanisms (EDLC and pseudocapacitance). Nevertheless, the similarities in their electrochemical signatures can be ascribed to the relationship between potential and the amount of charges developed at the electrode/electrolyte interface or within the inner surface due to adsorption/desorption processes. Thus, without such electrochemical features (signatures), the materials cannot be qualified as pseudocapacitive, and it is not appropriate to calculate the capacitance values. Typically, conductive polymers (CPs) and transition metal compounds (TMCs) are the fundamental candidates explored as pseudocapacitive electrode materials [52-55]. It must be eminent that these explanations related to the pseudocapacitive nature of materials must only be applied to an individual electrode and not to the device.

2.2.2 Intercalation pseudocapacitors

Apart from surface redox reactions, some layered materials (such as TiO_2 (B), Nb_2O_5, and MoO_3) undergo Faradaic charge transfer due to the intercalation of electrolyte ions into

the tunnels or layers with no crystallographic phase change. Notably, these materials exhibit reversible and fast charge storage rates approaching or even surpassing the traditional surface-redox pseudocapacitive materials;[11, 56] therefore; they cannot be directly referred to as redox pseudocapacitors. This type of charge storage mechanism is defined by Dunn and Simon[45, 57] as "intercalation pseudocapacitors", which is common in non-aqueous electrolyte system. The electrochemical features of the intercalation pseudocapacitance are: the current is linearly proportional to the sweep rate, capacity does not vary significantly with charging time, and peak potentials do not shift considerably with sweep rate. A key feature for the intercalation pseudocapacitance is that materials do not undergo phase transformations during intercalation. The general reaction mechanism can be expressed as follows:

$$MA_y + xLi^+ + xe^- \leftrightarrow Li_xMA_y \qquad (3)$$

In contrast to the EDLCs, the charge storage process for the intercalation pseudocapacitance is not limited to the surface and thereby utilizing bulk of the materials for the reversible faradic electrochemical reactions. Nb_2O_5 is the typical example of the intercalation pseudocapacitance. The corresponding electrochemical profiles are shown in Figure 1 (g-i).

2.3 Battery-type charge storage and true performance metrics

The conventional battery-type electrode materials are different than the capacitor-like electrodes in terms of the redox processes, which is responsible for the phase change of the electrode materials during the electrochemical process. Moreover, during the charging-discharging process, the potential of the battery-type electrode remains constant, agreeing to the phase rule and follows the Nernst equation, as shown in Figure 1 (j-l). Therefore, the materials with solid-state diffusion-controlled faradic (battery-type) reactions display a couple of well-defined redox peaks in CV profiles and flat (plateau) charge/discharge profiles similar to a battery (see Figure 1 k, l).[15, 58] The typical battery-materials include Ni, Co, Cu and Cd constructed oxide/hydroxide, sulphide/selenide and phosphide that react with

hydroxide ion in alkaline media to store a charge. In the case of the battery-type electrode materials, it is strictly necessary to calculate the specific capacity (mAh/g) or specific charge (C/g) from the CV and GCD profiles because the "average capacitance (F)" will not be constant throughout the potential window. These metrics provide the number of ions and electrons accepted by a certain mass generally intercalated into a crystalline solid inside an electrode. The practical, specific capacity can be calculated by using both CV and GCD curves as follows. Typically, CV is recorded at a fixed voltage scan rate (V/s), and the specific capacity can be estimated by CV curves using the following equation:

$$Specific\ capacity\ (Ah/g) = \frac{\int i(V)dV\ \ (A.V)}{m(g) \times \vartheta\ (V/s) \times 3600} \qquad (4)$$

where the integration of current over voltage window will give the total voltammetric charge (which needs to be divided by 2) in A.V (ampere*volts); ν is scan rate and m is the mass loading. Typically, CV is recorded at a slow scan rate for battery-materials, which can deliver the best capacity values. However, it is vital to perform a few CV cycles until they overlap before making any calculations. The specific capacity can also be calculated by using galvanostatic CD curves (n=1):

$$Specific\ capacity\ (Ah/g) = \frac{\int i\ (A)\ dt(s)}{3600 \times m\ (g)} \qquad (5)$$

In equation 5, i, t, and m are the applied current density (A), discharge time (s), m is the mass loading of the active material (g). Moreover, the specific capacity of the electrode (for only capacitive materials while using in devices) can be further converted into specific capacitance (F/g) by applying the following equation:

$$Specific\ capacitance\ (F/g) = \frac{Specific\ capacity\ (Ah/g) \times 3600}{\Delta V\ (V)} \qquad (6)$$

where V is the potential window of the solitary electrode configuration (V). Such calculations are crucial to build a full device using a capacitive negative electrode.

2.4 Evolution of the term "Extrinsic Pseudocapacitors."

The rapid development of nanotechnology stimulates the use of nanomaterials with large surface areas and nano-dimensions as electrodes in energy storage devices, particularly in batteries. Such nano-structuring reduces the ion diffusion lengths and sometimes conquers the phase-change in battery materials. As a consequence, their electrochemical signatures shift to pseudocapacitive materials (quasi-rectangular CV and quasi-triangular CD curves). In this case, the traditional definition of "pseudocapacitor" is unable to differentiate these materials from "battery-type" behaviour. Therefore, Dunn and co-workers[14, 45] have referred this new development as "extrinsic pseudocapacitors" where the materials show battery-like features (strong redox peaks and plateau in GCD) in the bulk phase, however, in the form of nanostructures, pseudocapacitive behaviour emerges. The most notable example of such battery materials is $LiCoO_2$, which is a well-known intercalation-type cathode in traditional lithium-ion batteries. When the size of $LiCoO_2$ particles was reduced to <10 nm, the electrochemical profile (GCD) changes from that of a typical battery (voltage plateau) to a capacitive profile with a linear dependence of charge storage (linear voltage) within the potential window (see Figure 2a).[16] It is believed that the increased surface area via nano-structuring suppresses phase transformation of $LiCoO_2$ to a large extent and promotes the rate performance because of decreased diffusion lengths and increased surface lithium-ion storage sites. This example demonstrates how typical battery-type material turns to a pseudocapacitive material after reducing its dimensions to nanoscale by promoting surface-dominant ion-storage. Similarly, nano-sized V_2O_5, nickel and cobalt hydroxides have also been considered as "extrinsic pseudocapacitors" by some researchers.[59, 60] Similar to the layered metal oxides, the 2D layered metal sulphides (MS_2, where M= Mo, W, V, Ti, etc.) are also considered as ideal candidates for the intercalation pseudocapacitance owing to their unique sulphide-metal-sulphide (S-M-S) layers, which are linked through van der Waals

forces,[61, 62] and can provide the sufficient interspace for the alkali metal ions to perform the intercalation/de-intercalation electrochemical reactions. [63-65]

3. Distinguishing capacitive contribution from a diffusion-controlled process

The recent evolution of "intercalation pseudocapacitance" has dramatically broadened the number of pseudocapacitive materials. However, it is well-known that the intercalation in batteries is limited by semi-infinite diffusion into the bulk of host materials, which is reflected by strong-redox peaks in CV curves. Whereas several intercalation pseudocapacitive materials demonstrate minor or tiny redox peaks in CV curves, which then arises a question– how to ascertain that these diffusion reactions do not limit the intrinsic kinetics? To resolve this issue, the quantification of the charge storage kinetics of these new materials will be an important method. In principle, the redox electrode materials display specific electrochemical features in their response to (a) scan rates in the CV; (b) applied constant current in GCD curves and (c) alternating current in electrochemical impedance analysis.[11, 45] Several methods are reported to quantify or distinguish diffusion-controlled process and non-diffusion limitation process for electrode materials.[66-68] Among those, CV measurements is an ideal tool where the response current is varied with scanning rates depending on whether the redox reaction is controlled by ion diffusion or not.

It is assumed that the total charges stored in the intercalation type electrode materials are the sum of diffusion-controlled faradic and capacitive (pseudocapacitive + EDLC) processes. As a result, it is essential to identify the capacitive contributions (EDLC + pseudocapacitance) and diffusion-controlled faradic process to the total capacity of the electrode materials. Simple CV measurements at various scanning rates can be sufficient for such a differentiation where the current response for the applied sweep rate is a combination of diffusion-controlled (faradic) and surface-controlled (capacitive) processes. At a particular

potential, the relationship between the current (i) and the scan rate (v) can be expressed by a power law [69]:

$$i = a v^{b} \quad (7)$$

The value of the b in the above equation can tentatively define the majority of the charge storage process, and it can be determined from the slope of the plot of log(i) *v*. log(ν). The parameter b has two well-defined conditions (Figure 2b). The b value of 1 signifies that the majority of charge contributions are from fast surface-controlled redox reactions and the adsorption/desorption of the electrolyte ions. In this case, the current response in the CV curves is linearly varied with the scan rate($i \propto \vartheta$). On the other hand, the b value of 0.5 corresponds to slow semi-infinite diffusion-controlled faradaic processes where the current response in the CV curves is varying with the square root of the sweep rate ($i \propto \vartheta^{1/2}$) and can be expressed as follows:

$$i = nFAC^{*} D^{1/2} v^{1/2} (\alpha n F / RT)^{1/2} \pi^{1/2} \chi(bt) \quad (8)$$

where C^{*}, α, D, *n, A, F, R, and T* are the surface concentration of the electrode material, transfer coefficient, chemical diffusion coefficient, number of electrons involved in the electrochemical reaction, electrode material surface area, Faraday constant, molar gas constant and temperature, respectively. The function (bt) symbolizes the normalised current. By calculating the value of b by using the power law, it is possible to identify the material type in terms of the capacitor and battery. Also, it is possible to estimate the exact contribution of the surface-controlled processes (EDLC + pseudocapacitance) and the diffusion-controlled processes (i.e., faradic processes in battery-type electrodes). There is no clear boundary which can define the pseudocapacitive and battery-type materials based on b value. The b value ranges from 0.5 to 1.0 signifying the transition from the battery type behaviour to the capacitive behaviour. More importantly, the value of the b can act as a

guideline to design and develop the high-performance SCs electrode materials. For example, (i) *b* value can act as a gauge to distinguish pseudocapacitive charge storage mechanism from the battery-type; and (ii) it provides the more kinetic evidence in terms of the charge storage process at various potentials and sweep rates. Further, it is possible to quantify the exact capacitive ($k_1\nu$) and battery type ($k_2\nu^{1/2}$) charge storage contribution by rearranging equation (7) as follows:

$$i(V) = i_{cap} + i_{diff} = k_1\vartheta + k_2\vartheta^{\frac{1}{2}} \qquad (9)$$

or

$$\frac{i(V)}{\vartheta^{1/2}} = k_1\vartheta^{1/2} + k_2 \qquad (10)$$

Cracking the values of k_1 and k_2 at respective potential permits for the separation of the diffusion and capacitive currents. The slope and the y-axis intercept point for the plot of $i/\nu^{1/2}$ versus $\nu^{1/2}$ will give the value of the constants k_1 and k_2, respectively. After estimating the values of the constants k_1 and k_2, it is straightforward to distinguish the capacitive ($k_1\nu$) and the diffusion-controlled ($k_2\nu^{1/2}$) currents in the voltammograms as a function of diverse potentials. As seen in Figure 2c, the blue areas indicate how the capacitive current contribution changes in the CV curve.

In some recent work, this method is also utilized to investigate the quantitative kinetics battery-type Faradaic electrodes. For instance, $Li_4Ti_5O_{12}$ [70] and even for electrodes based on conversion reactions and alloying mechanism in Na and K-ion batteries,[71, 72] where the capacity contribution from capacitive reactions was estimated to be 58 % (for B-SnS_2 electrode at 0.2 mV/s)[71] and 90.7% (for VSe_2 as a conversion anode for KIBs at 1.1 mV/s).[72] Thus, referring to such a large capacitive contribution as "pseudocapacitance" is misleading and puzzles between the terms "battery" and "pseudocapacitive" materials. However, such an instance can be well explained as $b \approx 1$ suggests that the process is either a capacitive or a

fast redox reaction process, which has no diffusion limitation owing to the large surface area and short diffusion lengths of nanostructures. It is emphasized that all the electrochemical signatures should be presented in a wide range of sweep rate and current density to fit the above criterion. Moreover, to determine *b*-value using Dunn's method, it is suggested to record CV curves at relatively low scan rates. Indeed, the kinetics analysis is constructive to understand the charge storing mechanism. Still, it cannot be solely used to determine whether an electrode material is a pseudocapacitive one or not, since the basic electrochemical signatures should be firstly considered. Besides, other methods such as electrochemical impedance analysis should be utilised to support the claims.

4. An asymmetric supercapacitor (ASSCs) vs hybrid supercapacitors (HSSCs)

There is a growing number of papers on the asymmetric configuration of supercapacitive cells, and it is important to define standard terminologies to refer to these devices. The clear distinction between the "asymmetric" and "hybrid" SCs has been previously explained by Brousse et al. [15]. Note that the terms "asymmetric" and "hybrid" can only be used for devices and not for the electrodes. It is well known that the capacitors are the high-power devices with limited energy storing capacity while the batteries are the high-energy devices having poor power density. The combination of both systems is expected to develop a single device, which can deliver simultaneous high power and high-energy characteristics, as depicted in Figure 3 (a). Such a system can be fabricated using two dissimilar electrodes of different charge-storing mechanisms, for example, one capacitive and one battery-type Faradaic (activated carbon and $Ni(OH)_2$) electrodes. These devices display the electrochemical signature in between SC and battery-type electrodes and defined as "hybrid supercapacitor (HSSC)" (Figure 3a)[12, 73, 74]. In HSSCs, the high working potential (ΔV) is used to reach the redox potential of the battery-like electrode (ΔV_b), which ultimately

improves the energy storing capacity of the SCs. The CV and GCD curves for HSSCs (full cell) with one battery-type and one capacitive (EDLC or pseudocapacitive) electrodes show the deviation from ideal capacitive characteristics with more capacitive-like behaviour due to the hybridizations, as shown in Figure 3 (a). Although the high capacity and wide working voltage improve the energy storing capacity of the HSSCs, the battery-type electrode with intrinsically slow charge kinetics (due to phase transformation) leads to poor rate performance, inferior cycle life and sluggish dynamics.[75-77] Many strategies were proposed to circumvent these issues that include the design of nanoscale-electrodes, the introduction of highly conductive carbonaceous additives, such as graphene, carbon nanotube (CNT) and AC etc.[78-80]

Besides the battery-type positive electrodes, the use of reversible ion adsorption (EDLC) or fast surface redox reaction (pseudocapacitive) capacitor-type electrodes is anticipated to be a promising approach to develop a new cell with comparable power density to that of SCs. In this respect, a new cell design with two different electrode materials (such as the cell having two different electrode materials with different charge storing mechanism or the electroactive materials having varied ratios of the redox-active sites) is proposed and defined as "asymmetric supercapacitors (ASSCs)". Most of the time, the electrodes are based on the capacitive or pseudocapacitive mechanism, and the cell can provide the high working voltage with high energy density at high power rates and long-standing driving stability. The term "asymmetric" should only be used when capacitive or pseudocapacitive electrodes (both EDLC or both pseudocapacitive or one EDLC//one pseudocapacitive) are involved (for example, activated carbon//MnO_2) (Figure 3b) to avoid confusion with HSSCs. The ASSCs with two capacitive electrodes show an idyllic rectangular box-type CV curve and a triangular GCD curve for the full device (see Figure 3b).

According to the thermodynamic, both ASSCs and HSSCs use the different potential windows of the positive and negative electrode to reach the maximum working voltage for the SCs cell. As a result, a greatly enhanced energy storing capacity is recorded for both ASSCs and HSSCs cells. Charge balancing ($Q_+ = Q\_$) on both electrodes is essential to reach the highest cell voltage and energy density value. Since the stored charges are related to the specific capacitance (C), and mass (m) of the electrode, the optimized mass ratio from the positive to negative electrodes can be derived according to the following equation.[81-83]

$$\frac{m_+}{m_-} = \frac{C_- \times \Delta E_-}{C_+ \times \Delta E_+} \qquad (11)$$

where m_+, m_-, C_+, C_-, ΔE_+, and ΔE_- are the masses, capacitance and the potential window for the positive and negative electrode, respectively. Further, the energy and power densities can define the performance metrics of the ASSCs and HSSCs cells. The following equations have been used to estimate the energy density (E, Wh/kg) and power density (W/kg) values for the SCs cell:

$$E\ (Wh/kg) = \frac{0.5\ \times C(F/g) \times V^2\ (V)}{3.6} \qquad (12)$$

$$P\ (W/kg) = \frac{E\ (Wh/kg) \times 3600}{t\ (s)} \qquad (13)$$

where t is discharging time and the V is the resultant voltage of the SCs cell. It must be noted that the energy and power densities can only be calculated for full device and not for the single electrode (conventional three-electrode cell). The estimation of electrochemical performances of both of these devices should be carefully performed, taking into account the charge-storing mechanisms and their resulting electrochemical signatures, which is described in detail by Kaner et al.[84].

5. Roadmap for the selection of active electrode materials for asymmetric designs

Ideally, it is necessary to calculate the theoretical capacitance for the electrode materials before using it for the SCs cell application. Such kind of calculations can give the basic idea regarding the appropriateness of the electrode materials for SCs. For the pseudocapacitive electrode materials, the theoretical capacitance can be calculated by using the following relation between the potential (E) and fractional charge analysis (X = 1) as follows:

$$C = \left(\frac{nF}{m}\right)\frac{X}{E} \qquad \text{(here X is assumed as 1)} \qquad (14)$$

where *n*, *F* and *m* are the number of transferred electrons, Faraday's constant, and molecular weight of active material, respectively. The discussion was so far convinced that the key to achieving high energy density SC is to widen the working voltage window of the device. The selection of the electrode materials (both positive and negative) and electrolyte plays a vital role to determine the operational voltage window of the device. However, all the approaches to enhance the voltage window of the SCs cell are not fully understood. Nevertheless, the oxidation-reduction reactions in metal oxides are directly associated to their work functions,[85] and the electrodes with the largest work function difference can offer highest voltage window in ASSCs. Thus, the following equation can be used to calculate the working voltage window for the ASSCs:

$$E = E_0 + \Delta E_1 + \Delta E_2 = \frac{1}{F(\omega^{\beta} - \omega^{\alpha})N_A} + \Delta E_1 + \Delta E_2 \qquad (15)$$

In the above equation, the work function for the positive and negative electrode is denoted by ω^{α} and ω^{β}, respectively. At the same time, the N_A, ΔE_1 and ΔE_2 are the Avogadro's constant, surface dipole potential of the positive and negative electrodes, respectively.[86, 87] For the SCs cell with two identical electrodes having the same charge storage mechanism (symmetric SCs) leads to the $\Delta E_1 = -\Delta E_2$ and $\omega^{\beta} = \omega^{\alpha}$. Hence, the operating voltage limit for the symmetric SCs is similar to their three-electrode measurements, or it depends upon the

dissociation energy of the electrolyte. On the other hand, the HSSCs and ASSCs contain two different electrodes having different work function values, and the working potential leads to the higher voltage limit. Therefore, the higher voltage limit for the SCs device is reachable when the two different electrodes have the largest work function difference. More importantly, the observed working voltage ranges for the HSSCs and ASSCs are larger than for the SSCs and the water dissociation potential. In the aqueous system of the electrolyte, the hydrogen and oxygen evolution reactions on the electrode surface lead to the water dissociation, which kept constraints on the resultant voltage window of the cell. The work function values for the different electrode materials and their potential operating window are summarised in Figure 4 (a) which can guide us for selecting the positive and negative electrode materials for the HSSCs and ASSCs [88-91]. In the case of the metal oxide-based electrode materials, the work function can be modified by creating some oxygen vacancies that will act as n-type dopants and as a result, shift the Fermi level closer to the conduction band edge. Moreover, the chemisorption of proton and hydroxide ions from the electrolyte solution on the surface of the metal oxide electrode will further enlarge the potential window by modifying the work function. Thus, according to Figure 4 (b), the MnO_2 (with 6.2 eV) and MoO_3 (with 4.4 eV) can be considered as positive and negative electrodes, respectively, to achieve extended voltage windows owing to their largest work function difference. Thus, the potential working window for MnO_2//MoO_3 ASSC can be calculated using equation 15 (see Figure 4b). Further, to provide more insight for developing the high voltage SCs cell, we have summarized the redox potential windows of different materials in Figure 5, which will guide the researchers to identify appropriate positive and negative electrode materials and electrolytes. Here we would like to mention that the potential window of the electrode materials varies from one electrolyte to another one (pH or ion types) as well as the

nanostructure, crystal structure and the particle size can modify the potential window for the electrode material.

6. Materials innovations for solid-state asymmetric designs

The electrode materials and the electrolytes are the primary performance determinant factors in energy storage systems. This section will provide the earnest efforts taken to develop electrode materials for two distinct device configurations based on charge storing mechanism and combination of electrodes: 1) Asymmetric solid-state supercapacitors (ASSCs), which will cover the advances in the capacitive/pseudocapacitive materials in terms of the positive and negative electrodes; 2) Hybrid solid-state supercapacitors (HSSCs), which will be focused on the development of different battery-type materials as positive electrodes in combination with different capacitive electrodes.

6.1 Asymmetric solid-state supercapacitors (ASSCs)

As defined previously, the asymmetric SCs is comprised of two electrodes revealing the capacitive (EDLC and pseudocapacitive) mechanisms. It should be noted that only intrinsic pseudocapacitive materials are considered in this class of devices. The section is dedicated to the development of promising electrode materials for ASSCs. Typically, carbon and its allotropes such as activated carbon (AC), graphene, CNTs etc. are proposed as favourable candidates for EDLCs, while transition metal compounds (including oxides/carbides/nitrides) and conducting polymers (polyaniline, polypyrrole, and polythiophene) with fast and reversible redox reactions are explored as pseudocapacitive electrodes.[92] Here, we have summarized the advances in ASSCs, taking into account the electrode materials with capacitive or pseudocapacitive mechanisms (both EDLC or both pseudocapacitive or one EDLC//one pseudocapacitive).

6.1.1 Carbon for negative electrodes

Traditionally, carbon and its allotropes are the most prospective negative electrode materials for the ASSCs owing to their higher electrical conductivity, good mechanical stability, large abundancy, eco-friendly nature and low cost. [38, 93] In addition to this, the large specific surface area, tunable porosity, and chemical inertness with double-layer charge storing mechanism make them desired negative electrode material candidate to achieve higher electrochemical response for ASSCs.

Among several carbon-based materials, activated carbons (ACs) in combination with transition metal compound have been extensively studied as a negative electrode in ASSCs due to their excellent features such as high specific surface area (SSA) (2,000 to 3,000 m^2/g) with wide pore-size tunability, extending from macropores (>50 nm) to nanopores (<2 nm).[94-97] Some of the AC-based ASSCs have been developed. The best example is AC//MnO_2.[98] Pseudocapacitive MnO_2 has been extensively investigated as a positive electrode in ASSCs due to its large natural abundance, low cost, large theoretical capacitance (~1370 F/g), and low harmfulness.[99, 100] From the charge storage point of view, the MnO_2-based electrode materials can perform the fast and reversible pseudocapacitive redox reactions (Mn^{3+}/Mn^{4+}) at or near the surface of MnO_2 nanostructures. Zhang and co-workers fabricated ASSCs using Ni/MnO_2 decorated filter paper (FP) as the positive and Ni/AC decorated FP as negative electrodes with gel electrolytes composed from the poly(vinyl alcohol) (PVA)-Na_2SO_4 (Figure 6a). The optimized ASSCs might work in the wide voltage window of 2.5 V and delivered a capacitance of 1.4 F/cm^3 at 2.5 mA/cm^3 current density with the excellent maximum energy density of 0.78 mWh/cm^3.[101] The low electrical conductivity with rarely achieved theoretical capacitance is the major obstacle for the MnO_2-based pseudocapacitive electrode for its utilization in practical ASSCs.[45] Combining the MnO_2-based electrode material with the other conducting electrode materials is the best option to enhance their

energy storing and delivering capacity. With this aim, Tao et al.[102] developed polypyrrole (PPy) wrapped MnO_2 nanoflowers on the flexible carbon cloth (CC) current collector as a positive electrode and assembled ASSCs by pairing with AC@CC with enhanced electrical conductivity. The AC//PPy/MnO_2 device exhibited 1.41 F/cm^2 of volumetric capacitance with energy density and power density of 8.67 mWh/cm^3 and 12.35 mW/cm^3, respectively, in an extended voltage window of 1.8 V. The ASSCs cell could further light up an LED display, a toy car and a mini-motor after full charging.

Despite the significant advancement in AC-based ASSCs, the poor electrical conductivity and low specific capacitance of AC hinder their application in high-performance SCs.[103] Instead of AC, the one dimensional (1D) carbon nanotubes (CNTs) are considered as a favourable nominee for SCs since Niu et al. anticipated this.[104] Although CNTs exhibits less theoretical SSA (≈50-1315 m^2/g), CNTs can deliver relatively high capacitances than ACs due to their unique tubular structures with a large number of mesopores, which offer easy charge transportation and great accessibility of electrolyte ions.[105, 106] Also, CNTs provide lower contact resistance during charge/discharge reactions, leading to great energy and power densities.[107, 108] The MnO_2-decorated CNTs have been prepared by Kang et al.[109] for the ASSCs as positive electrode materials with the CNTs coated regular Xerox paper as negative electrodes. The combination of the different featured electrode materials in the single electrode can enlarge the energy storing capacity. Here, the high energy storing capacity of the MnO_2 merged with highly conducting nature of the CNTs leads to the specific energy of 5.97 Wh/kg. Importantly this figure is higher than that of a CNTs-based symmetric cell (0.89 Wh/kg). In recent years, the highly flexible woven or knitted fabrics/textiles based SCs have been developed by using CNT fibres.[110] For example, the ASSCs based on CNT@MnO_2 composite as a positive electrode and the CNT yarn as the negative electrode conveyed about five-fold larger energy density (42 Wh/kg) and power density (483.7 W/kg) than the CNTs-

based SSCs.[111] Because of the high strength and flexibility, CNT//CNT@MnO_2 two-ply device maintains excellent electrochemical performances during the repeated folding/unfolding actions, implying its suitability for flexible automated electronic gadgets which require high permanency and wearer comfort.

Likewise, fibre-shaped ASSC with high volumetric energy density was assembled using a positive electrode based on the ternary hybrid fibre, and carbon/CNTs ordered microporous as a negative electrode.[112] The ternary hybrid was prepared by growing MnO_2 nanosheets onto Poly(3,4-ethylenedioxythiophene):poly(styrene sulfonate) (PEDOT:PSS)-coated CNTs fibre (Figure 6b). The device delivered a high volumetric energy density of ~11.3 mWh/cm^3 and high volumetric power density of ~2.1 W/cm^3, analogous to the commercially available bulk supercapacitors with good cycling stability of 85% retention over 10,000 cycles. Due to the unique fibre shape, such devices can be woven or knitted into flexible power textile applications. Despite great research on CNTs-based SCs, the lack of efficient and low-cost manufacturing methods hampers the technology transfer to the commercial market. Also, the imbroglio in CNTs is the main difficulty that results in poor efficiency as it limits ionic transport.

Recently, the graphene-based electrode materials have been considered as an emerging negative-electrode for ASSCs due to their exceptional electrical conductivity, mechanical flexibility, and higher SSA (2630 m^2/g).[113-115] The exceptional inherent double-layer capacitance (≈21 μF/cm^2) in graphene can deliver a huge specific capacitance of up to 550 F/g, beating almost all EDLC materials, including ACs, CNTs, mesoporous carbon.[116, 117] In recent years, several exciting ASSCs have been developed using graphene-based negative electrodes. For instance, Pan et al.[118] have developed ASSC by pairing MnOx (as a positive electrode) with chemically converted graphene (CCG) as a negative electrode. Initially, ultrathin MnO_x nanosheets were grown on Ni-coated CC to prepare a three-dimensional (3D)

porous electrode. Typically, 3D porous nature of the electrode materials is beneficial for the electrochemical performance as it provides the shorter diffusion paths for electrolyte ions and continuous electron pathways for better electrical contacts.[119] The as-fabricated device delivered excellent cyclic stability of 81.5% after 10,000 charge/discharge with an energy density of 1.16 mWh/cm^3. However, restacking of the graphene sheets significantly lowers the SSA and results in low energy storing capacity. To overcome this drawback, graphene-based nanocomposites such as graphene/MnO_2 as a positive electrode and the graphene/Ag as a negative electrode have been prepared and used in the ASSCs.[120] This approach overcomes the restacking problem of the graphene nanosheets and improves the electrical conductivity and capacitance of the electrodes. The resulting ASSCs cell showed the highest energy density of 30.8 Wh/kg with a power density of 24.5 kW/kg.

Likewise, Yang et al.[121] developed the ASSCs by pairing the 3D Al@Ni@MnO_x nanospike (NSP) and CCG as a positive and a negative electrode, respectively, which can operate in the voltage window of 1.8 V. Interestingly, the assembled ASSCs cell delivers the energy density of 23 Wh/kg (1.29 mWh/cm^3), which was maintained to the 6.57 Wh/kg at a high power density of 59 kW/kg. Additionally, the cell delivers excellent cycling durability over 10,000 cycles by reversing 96.3% of its initial capacitance, implying effective utilization of active materials, facilitating electrolyte permeation, and shortening the electron pathway in the active materials. Conversely, another effective approach to avoid restacking of graphene nanosheets is mixing them with other carbon materials. Freestanding CNT-graphene (CNT-G) paper is presented as an efficient negative electrode with Mn_3O_4-graphene (Mn_3O_4-G) paper[122] as a positive electrode to assemble ASSCs, which could be reversible in the higher voltage window of the 1.8 V. The cell achieved an energy density of 32.7 Wh/kg, which is much higher than that of Mn_3O_4-G (7.1 Wh/kg) and CNT-G (10.5 Wh/kg) based symmetric cells. More importantly, the CNT-G//Mn_3O_4-G cell shows maximum power density of 9.0

kW/kg at a high energy density of 22.9 Wh/kg signifying that it can provide high energy and power densities as well as high current densities. The low specific capacitance is another issue for the graphene-based electrodes apart of restacking, which obstructs its practical applications. An emerging tactic to improve the capacitance is the functionalization of graphene with functional groups, metal oxides or conducting polymers.

Choi and co-workers[123] assembled ASSCs based on an ionic liquid functionalized chemically modified graphene (IL-CMG) film (as the negative electrode) and a hydrous RuO_2-ILCMG composite film (as the positive electrode) (Figure 6c). Flexible self-standing ASSC device exhibited a high energy density of 19.7 Wh/kg and power density of 6.8 kW/g, higher than those of symmetric SCs based on IL-CMG films. Moreover, the device can operate even under extremely high current density 10 A/g with 79.4% retention of specific capacitance. Remarkably, this device retained 95% of its specific capacitance after 2000 cycles under harsh mechanical conditions including twisted and bent states, suggesting excellent flexibility and cycling stability. Recently, the Metal-organic frameworks (MOFs) derived nanoporous carbon has been used as a negative electrode to assemble the ASSCs.[124] For example, Tian et al.[125] prepared the porous metal-doped carbon material for the ASSCs via specific carbonization process of the MOFs. The developed ASSCs with the porous metal-doped carbon material show the energy density of 51.4 Wh/kg with a power density of 1500 W/kg. Similarly, Zhao et al.[126] developed ASSCs with N, F co-doped hierarchical nanoporous carbon polyhedron (NFHPC) as a negative electrode showing the energy density of 55.1 Wh/kg at a power density of 799.8 W/kg, and a long cycle life up to 5000 cycles.

6.1.2 Metal oxides for negative electrodes

As described in the previous section, carbon composed materials are employed as negative electrodes in combination with positive pseudocapacitive electrodes for designing

various ASSCs (EDLC//pseudocapacitive type). However, the lower capacitance of carbon-based negative electrodes limit the overall capacitance of ASSCs according to the following relation; $1/C_T = 1/C_+ + 1/C_-$, where C_T is total capacitance, C_+ and C_- are capacitances of positive and negative electrodes, respectively.[127]. Compared with EDLCs, pseudocapacitive electrode materials can achieve much higher energy storing capacity as they can provide a variety of oxidation states for efficient redox charge transfer. Some pseudocapacitive metal compounds (including oxides/nitrides, conducting polymers) which operate in the negative potential window[89, 128, 129] may be combined with another positive pseudocapacitive material and thus overcome the limitations of the carbon-based ASSCs. Typical pseudocapacitive materials with negative potential window, including MoO_3 and Fe_2O_3, [89, 130] hold a great promise to provide high energy density. Taking advantage of the diverse operating potential windows of MnO_2 NWs (positive side) and Fe_2O_3 nanotubes (negative side), Yang et al. [130] developed flexible ASSC with PVA-LiCl gel-electrolyte (Figure 7a). The cell cycled in the voltage limit of 1.6 V with high specific capacitances of 91.3 F/g (1.5 F/cm^3) at a current density of 2 mA/cm^2. Besides, MnO_2//Fe_2O_3 device showed excellent rate capability (with 59% retention) with an energy density of 0.55 mWh/cm^3 and a high power density of 139.1 mW/cm^3. Nevertheless, the inherent semiconducting nature of metal oxides- based electrode materials leads to poor electrical conductivity, ultimately resulting in low electrochemical parameters for ASSCs.[131] In this respect, Fe_2O_3 nanorods coated with carbon shell (Fe_2O_3@C) were explored as a negative electrode with MnO_2 nanowires based positive electrode. The thin carbon coating on the Fe_2O_3 nanorods grown on CC improved the electrical conductivity, while MnO_2 was decorated on CuO NWs, which were prepared by annealing Cu-wire.[132] The coil-type ASSCs were accumulated by merely twisting the Fe_2O_3@C negative electrode onto the MnO_2@CuO NW positive electrode divided by a PVA-LiCl gel-electrolyte. Remarkably, the assembled wire-type cell delivered 2.46 F/cm^3 of

capacitance along with excellent rate-performance (95.4%) and high energy density of 0.85 mWh/cm^3. Moreover, 93 % of cycling stability was obtained for the 4,000 cycles at different bending states. Similarly, the conductivity of metal oxide electrodes can be further improved by merging them with highly conducting carbon-based materials. As an example, ASSC was assembled with the positive wrinkled MnO_2/CNT electrode and negative wrinkled Fe_2O_3/CNT electrode[133]. The enhanced electrical conductivity for both positive and negative electrodes improves the electrochemical features such as an extended voltage of 2 V, the energy density of 45.8 Wh/kg and continued cycling over 10,000 cycles.

Thus, several advancements have been reported using transition metal compounds based negative electrodes in ASSCs by designing various strategies such as nanocomposite electrodes, modifying crystal structures and use of deep eutectic solvent-based electrolyte. However, further enhancements can be done by testing many other negative//positive combinations and application of deep eutectic solvent-based electrolyte for these systems.

6.1.3 Metal nitride for negative electrodes

Due to the excellent electrical conductivity, metal nitrides have recently attracted much attention as promising electrode materials for high-performance SCs. For instance, the conductivity of titanium nitride (TiN) varies between 4×10^3 and 5.55×10^4 S/cm[134], which is close to that of metals and thus can be beneficial for SCs electrode that requires fast transport and effective collection of charge. Nevertheless, metal nitrides usually oxidise in aqueous solutions, and therefore, to circumvent this issue, they have been encapsulated with more stable materials by different processes, including CNT[135] and graphene wrapping.[136-138] In this sense, Zhu and co-workers[139] grown titanium nitride (TiN) and iron nitride (Fe_2N) on graphene nanosheets (GNS) and utilized them as the positive and negative electrode, respectively, to assemble ASSCs. The fabricated Fe_2N@GNS//TiN@GNS cell was operated

in a wide voltage window of up to 1.6 V. It delivered a stable capacitance of 60 F/g at 10 mV/s with < 2% capacity drop after an increase in scan rate to 100 mV/s, suggesting extraordinary rate capability. Moreover, the cycling stability of the device was tested under bending conditions from cycle 5,000 to 15,000 and subsequently under the natural state in the last 5,000 cycles, suggesting that bending had a negligible effect on the capacitance of the device. The device achieved both a high volumetric energy density of 0.55 mWh/cm^3 and a high power density of 220 mW/cm^3. Such impressive results can be credited to the structural stability of electrode material in a gel electrolyte.

6.1.4 MXene for negative electrodes

The term MXenes is collectively representing the family of materials such as transition metal carbides, carbonitrides and nitrides (e.g., Ti_3C_2, Nb_2C, Ti_3CN and Ti_4N_3), which are the latest 2D materials and have attracted much attention since their discovery in 2011.[140-142] These compounds have a general formula of $M_{n+1}X_nT_x$ (n = 1-3), where M represents an early transition metal (Ti, V, Nb, Cr and Mo), X is carbon and/or nitrogen, and T_x corresponds to the surface terminations (hydroxyl, oxygen and fluorine).[143, 144] Unique properties of these compounds such as high electronic conductivity (1000 to 6500 S/cm), excellent mechanical properties and hydrophilicity make them promising materials for energy storage systems. MXenes are commonly prepared by selective etching of element 'A' (mostly Al) from their layered precursors (MAX phases) using wet chemistry routes, such as etching in HF[145] or acidic solutions of fluoride salts (LiF in HCl).[146] MXene, especially $Ti_3C_2T_x$, is an emerging material due to its graphene-like 2D shape and unique properties, and high volumetric capacitance (1500 F/cm^3). Owing to their negative operational potential and pseudocapacitive nature, MXenes since recently are considered as promising negative electrode materials in ASSCs.[147,148] For instance, Jiang and co-workers[147], developed all

pseudocapacitive ASSCs using Ti_3C_2Tx as negative and RuO_2 as positive electrodes, which can operate in an extended voltage window of 1.5 V (Figure 7b). The complementary working potential windows of Ti_3C_2Tx and RuO_2, along with proton-induced pseudocapacitance, significantly enhanced the device performance to deliver an energy density of 37 μWh/cm^2 at a power density of 40 mW/cm^2 with 86% capacitance retention after 20,000 charge/discharge cycles. Similarly, the asymmetric yarn SC, which comprises MXene/CNT and MnO_2/CNT bi-scrolled yarns as negative and positive electrodes, was fabricated using PVA/LiCl gel electrolyte.[148] The MXene/CNT//MnO_2/CNT cell delivered a capacitance of 220 mF/cm^2 at 0.3 mA/cm^2 discharge rate. It retained about 80% when the discharge rate was increased tenfold (1-10 mA/cm^2). Due to the extended voltage window of 2 V, the device further showed an energy density of 100 μWh/cm^2 and high power density of 26 mW/cm^2 with capacitance retention of 96% over 10,000 cycles. Almost negligible loss in performance was observed under deformations, suggesting its applicability in wearable electronics. Thus, overall results show that the pseudocapacitive negative MXene electrodes can potentially replace carbon-based materials in ASSCs, leading to an increased energy density. However, further investigation of MXene-based negative electrode is required by exploring different positive electrodes and cell designs.

6.1.6 Conducting polymer for negative electrodes

In the 1990s, conducting polymers (CPs) were first demonstrated as promising electrode materials for SCs.[149] They exhibit pseudocapacitive charge storage through doping and de-doping of the polymer backbone, which results in intercalation and de-intercalation of electrolyte ions within the polymer electrode to maintain charge neutrality.[150] Also, CPs deliver high conductivity (imparted by their conjugated backbones, which allow for delocalization of p-electrons over the entirety of the polymer chain), low cost, and facile

processability,[151, 152] Several conducting polymers, namely polyaniline (PANI), poly(3,4-ethylenedioxythiophene) (PEDOT), and polypyrrole (PPy) displayed good specific capacitances, which are comparable or higher than many other pseudocapacitive metal oxides.[153-155] Interestingly, CPs can provide stable and impressive energy storage performance in both positive and negative working potentials. For example, all-polymer ASSC device was fabricated on Au-coated PEN plastic substrates using PEDOT and PANI as negative and positive electrodes, respectively,[156] which could be cycled in a wide voltage window of 1.6 V and exhibited a volumetric stack capacitance of 34 F/cm^3 at a current density of 0.5 mA/cm^2. Moreover, the PANI//PEDOT cell displayed the energy density of 12 mWh/cm^3, which was sixfold higher than that for the symmetric PEDOT cell (2 mWh/cm^3) and two-fold higher than for the PANI-based symmetric cell (5 mWh/cm^3). Further, the ASSC cell showed good cycling stability with capacitance retention of 80% over 10,000 cycles. Nevertheless, CPs undergoes serious mechanical degradation due to the swelling and shrinking during the charge/discharge processes. Thus, poor cycling stability is always observed, especially when the materials are used as negative electrodes. Therefore, different strategies have been developed to enhance and stabilize the capacitance of CPs in negative potential regions. In this context, Lu et al.[157] developed highly ordered 3D α-Fe_2O_3@PANI core-shell nanowires as negative electrodes for ASSCs. Initially, α-Fe_2O_3 nanowires were electrodeposited on CC and annealed in air, on top of which a thin layer of PANI was then electrodeposited to produce the 3D α-Fe_2O_3@PANI core-shell structure. This unique α-Fe_2O_3@PANI core-shell nanoarchitecture provides a large reaction surface area, fast ion and electron transfers and good structure stability, all of which improved the electrochemical performance. The ASSC cell was then assembled with α-Fe_2O_3@PANI as negative and PANi on carbon cloth as positive electrodes, which displayed a capacitance of 2.02 mF/cm^3 (based on the volume of the device). In addition, the device delivered a high energy density of 0.35

mWh/cm^3 at a power density of 120.51 mW/cm^3 with good cycling stability over 10,000 cycles. Another strategy explored to enhance the mechanical strength and cyclic stability of CPs is to make composites with carbon-based materials. CNTs are considered as an effective additive due to their exceptional mechanical properties, good electrical conductivities and large surface areas, which can help to mitigate the cycle degradation problems in pristine CPs. Recently, CNT/PANI as the negative electrode was prepared and combined with CNT/MnO_2/graphene positive electrodes to construct ASSCs with a PVP-Na_2SO_4 gel electrolyte.[158] The as-fabricated cell was operated in a high voltage range up to 1.6 V and achieved an energy density of 24.8 Wh/kg with a high-power density of 2,230 W/kg. Thus, several strategies have been developed to improve the capacitance and cycling stability of CPs in the negative voltage region, which are still significantly poorer than the expectations. Table 1 summarises the electrochemical performance of ASSCs based on different negative-electrodes with their corresponding gel electrolytes[159 160 161 162 163 164 165 166 167 168 169 170 171 172 173 174].

6.2 Hybrid solid-state supercapacitors (HSSCs)

As discussed in the previous section, the term "hybrid SCs" should be used when the device is fabricated using one capacitive and one battery-type Faradaic electrode, implying the characteristics of SC and battery in a single system. The first report on hybrid SCs was patented by Varakin et al. in the mid 90's[175] by combining EDLC electrode (AC) with a positive nickel-oxide battery electrode. This section will provide a brief description on similar cell designs by taking into account the recent advancements in faradic battery-type (including extrinsic pseudocapacitors) positive electrode given their nanostructures, composites and core-shell heterostructures, used to improve the overall electrochemical performances in terms of energy density and cycling stability. Note that the extrinsic

pseudocapacitors are also considered as battery-type materials despite their pseudocapacitive behaviour on nano-structuring, therefore, can be covered in HSSC.

6.2.1 Ni-based Materials for HSSCs

Nickel-based materials have been widely used for Ni-Zn, Ni-Cd, and Ni-Metal hydride batteries for many years. Indeed, these materials exhibit pure battery-characteristics, which store charges through Faradaic processes (see Figure 1 (j-l)); nevertheless, they have been falsely presented as pseudocapacitive electrodes for SCs and hybrid devices.[25, 176, 177] Regardless of this misinterpretation, Ni-based battery electrodes can be of interest as positive electrodes in HSSCs operating under KOH electrolyte, together with a suitable capacitive-negative electrode.[178] This section comprises the efforts taken to utilize Ni-based electrodes in hybrid designs (HSSCs) to achieve the improved energy and power densities of such devices. Note that, as described in the previous sections, the specific capacity (mAh or C) is the correct metric and not the capacitance (in F) for such battery-electrodes; however, to avoid confusion for the reader, we have used the same metrics used in respective papers.

Several Ni-based materials such as $Ni(OH)_2$, NiO and Ni-sulfides/selenides/phosphides have been utilized as positive electrodes in HSSCs. Among them, $Ni(OH)_2$ is widely investigated due to its high theoretical specific capacity (1041 C/g, 290 mAh/g), low cost, well-defined electrochemical redox activity and the possibility to enhance performance by forming nanostructures. $Ni(OH)_2$ exhibits hexagonal-layered structure and commonly exists in α and β forms, corresponding to γ- and β-NiOOH after oxidation. α-$Ni(OH)_2$ is a hydroxyl-deficient phase with interlayered anions and water molecules. β-$Ni(OH)_2$ possesses a brucite structure without water molecules. α-$Ni(OH)_2$/γ-NiOOH couple shows higher capacitance than β-$Ni(OH)_2$/β-NiOOH couple due to the more

considerable change in valence states. $Ni(OH)_2$ stores charges through deprotonation/protonation reaction, which can be expressed as follows:

$$Ni(OH)_2 + OH^- \leftrightarrow NiOOH + H_2O + e^- \quad (15)$$

Previous investigations suggested that the hydrous $Ni(OH)_2$ holds a great promise to provide a specific capacitance as high as 1000 F/g when used as a positive-electrode material.[179] However, the humble rate capability due to the poor electric conductivity of $Ni(OH)_2$ and the poor cycling stability confine its practical applications. Incorporation of $Ni(OH)_2$ with conducting carbon-based materials can efficiently improve the electronic conductivity, thus increasing the power density and stability of the resulting hybrid device. For example, Feng and co-workers[180] deposited $Ni(OH)_2$ and Mn_3O_4 on conducting paper (nickel/graphite/Paper, NPG) and utilized them as positive and negative electrodes, respectively, in HSSC. Normally, Mn-based oxides are employed as positive electrodes in aqueous neutral electrolytes; however, Mn_3O_4 ($Mn(II)[Mn(III)]_2O_4$) with Mn in multiple valences can provide rich redox reactions in the negative region with aqueous alkaline electrolytes. The superior cycling stability (82.5% capacitance retention after 12000 cycles) was observed for a $Ni(OH)_2$/NGP electrode. Moreover, the assembled flexible Mn_3O_4-NGP//$Ni(OH)_2$-NGP device delivered a large capacitance of 3.05 F/cm^3, superior cycling stability (87% capacity retention over 12000 cycles at a scan rate of 100 mV/s), and high energy/power densities of 0.35 mWh/cm^3 and 32.5 mW/cm^3, respectively. Similarly, flexible carbon fibres (CFs) have also attracted much attention as conducting support due to their high conductivity, high knittability, and porosity, which can effectively load the maximum amount of active material. $Ni(OH)_2$ coated on CF (CF-$Ni(OH)_2$) has demonstrated cycling stability of 99.9% over 1500 continuous charge/discharge in the conventional three-electrode configuration.[181] Furthermore, HSSC was assembled using CF-$Ni(OH)_2$ as the positive and CF-CNTs as negative electrodes in PVA-KOH gel electrolyte, which exhibited high specific energy of 41.1 Wh/kg at a high

specific power of 1.4 kW/kg accompanied by excellent cycle stability (retaining 98% capacitance retention over 3000 cycles).

Nickel oxide (NiO), which can be obtained through heating of nickel hydroxide, is also a promising positive electrode for HSSCs due to its high theoretical capacity (1292 C/g, 359 mAh/g), low cost and environmental friendliness. Two charge storing mechanisms have been proposed for NiO: one considers that the energy storage process occurs between NiO and NiOOH (Eq. 16 and 17) while the second suggests that first NiO changes to $Ni(OH)_2$ in an alkaline electrolyte and then the electrochemical reactions occur between $Ni(OH)_2$ and NiOOH (Eq. 18 and 19). The reactions can be expressed as follows:

$$NiO + OH^- \leftrightarrow NiOOH + e^- \quad (16)$$

$$NiO + H_2O \leftrightarrow NiOOH + H^+ + e^- \quad (17)$$

OR

$$Ni(OH)_2 \leftrightarrow NiOOH + H^+ + e^- \quad (18)$$

$$Ni(OH)_2 + OH^- \leftrightarrow NiOOH + H_2O + e^- \quad (19)$$

Similar to $Ni(OH)_2$, NiO also suffers from low conductivity and poor cycle performance due to the substantial volume change during the charging/discharging processes. Composing NiO with carbon materials or metal or conducting polymers can efficiently enhance the electric conductivity and surface area, leading to an excellent rate capability.[182, 183] Heteroatom doping of nickel (Ni) has been proposed to improve the electrochemical performance of Ni/NiO by tuning the annealing temperature of a nickel-based metal-organic framework (Ni-MOF).[184] The incorporation of Ni^{3+} into the primitive lattice of Ni/NiO nanoparticles introduces disordering into the Ni/NiO lattice, providing a large number of electrochemical reaction active and ion-conduction paths. The HSSCs based on Ni/NiO as positive and CNTs-COOH as negative electrode displayed a high energy density of 61.3 Wh/kg at the power density of 900 W/kg, which was maintained at 28.2 Wh/kg at a high

power density of 9064 W/kg. More importantly, the device delivered excellent cycling stability over 10,000 cycles with 92.8% capacitance retention, signifying that the specific structure of Ni/NiO composites can prevent the collapse of the structure caused by the volume expansion during cycling. Similarly, non-metal elements (such as N, P and S) were introduced into the crystal defects of Ni-MOF to enhance the stability of the Ni-MOF structure and create the unique frame structure. Among them, sulphur (S) doped Ni-MOF (S@Ni-MOF) demonstrated improved performance. The material was further utilized as a positive electrode to assemble HSSC with AC as a negative electrode. The as-assembled HSSC exhibited a high energy density of 56.85 Wh/kg at a power density of 480 W/kg. After 20,000 cycles, the capacitance retention was 86.67%, which can be assigned to the formation of a stable framework structure and large active sites due to S modification. Combining NiO with conducting polymers (CPs) is also another strategy, which not only improves the electrical conductivity and stability but also can deliver extra pseudocapacitance. For instance, Yang et al.[160] developed a fibre-shaped HSSC with NiO/$Ni(OH)_2$ nanoflowers encapsulated into a 3D interconnected PEDOT on contra wires (Contra is a kind of a Cu-Ni alloy with the nickel content from 1% to 44%) as the positive electrode and ordered mesoporous carbon (CMK3) as the negative electrode. The as-formed flexible HSSC device delivered an areal capacitance of 31.6 mF/cm^2 (3.16 F/cm^3) at a current density of 0.4 mA/cm^2, which was maintained to15.9 mF/cm^2 (or 1.59 F/cm^3) even at a higher current density of 8 mA/cm^2, suggesting excellent rate capability. The cell further exhibited an operating voltage of 1.45 V with an energy density of 0.011 mWh/cm^2 at a power density of 0.33 mW/cm^2 and stable performance over 1,400 cycles.

Besides Ni-oxides/hydroxides, Ni-sulfides/selenides are other candidates of the battery-family, which can be potentially utilized as positive electrodes for HSSCs owing to their desired properties such as higher electric conductivity, improved electrochemical

activity, and the diversity of stoichiometric chemistry compared to their oxide counterparts. The electrochemical behaviour of nickel sulphides involves the reversible redox reaction of Ni(II) ↔ Ni(III) in the presence of hydroxide counter anions and can be generalized as follows:

$$NiS_x + OH^- \leftrightarrow NiS_xOH + e^- \quad (20)$$

Among the diverse crystal structures of nickel sulphide, NiS, NiS_2 and Ni_3S_2 have been widely studied as electrode materials in energy storage systems. To achieve a high active surface area for capacitive enhancement, much research has been devoted to tailoring the morphology of the nickel sulphide nanostructures. For example, heazlewoodite Ni_3S_2 nanorods were directly grown on Ni foam (NF) as a binder- and conductive agent-free positive electrode for HSSC.[185] The heazlewoodite phase of Ni_3S_2 is among the most feasible for SCs due to its novel atomic structures and electronic properties.[186] In addition, Ni_3S_2 exhibits metallic behaviour but the bonding in its structure is more covalent compared with metal oxides,[187] resulting in high electronic conductivity and corrosion resistance. By combining 3D rGO-foam capacitive electrode with Ni_3S_2 Faradaic electrode, an HSSC was assembled, which was reversibly cycled up to 2.2 V and delivered high energy density of 70.58 Wh/kg at 1.1 kW/kg. Even at a high power density of 33 kW/kg, the device maintained an energy density of 52.44 Wh/kg with a capacity retention of 90.4% after 5000 cycles. The excellent device properties can be ascribed to the unique combination of metallic Ni_3S_2 nanorods and interconnected porous 3D rGO electrode, which offers sizeable ion-accessible surface area, efficient electron and ion transport pathways. According to the literature, nickel sulphides tend to assemble into hierarchical nanosheets. Due to their ultrathin and porous nature, the extrusion pathway of electrolyte ions is significantly reduced, accompanied by an increased accessible active surface area. In this regards, Chen et al.[188] developed open porous and sponge-like NiS/Ni_3S_2 hybrids with interconnected thin nanosheets. The formation of

such hybrid nanosheets significantly improved the rate capability, with 87.6% of the capacity retention when the current density was increased by 10 fold. A two-electrode HSSC comprising NiS/Ni_3S_2 as a positive and AC as a negative electrode demonstrated a high energy density of 0.289 mWh/cm^2 with a high power density of 12.825 mW/cm^2. Moreover, long-term cycling of the cell showed capacity retention of 86.7% after 8000 continuous GCD cycles, suggesting excellent stability with high Coulombic efficiency. Direct growth of active materials on a carbon fibre cloth (CFC) was proven to be an efficient way to improve the electrochemical performance of electrodes due to enhancement of phase contact between the electrode material and the current collector resulting in enhanced electron transfer. $Ni_{0.85}Se$ nanosheets array grown directly on CFC exhibited an excellent rate capability (83.17%) and improved cycling performance with 82.6% capacitance retention over 10,000 cycles.[189] The HSSC fabricated with AC negative electrode materials and KOH/PVA gel as the electrolyte achieved a high energy density of 29 Wh/kg at a power density of 779 W/kg under the optimal voltage range of 1.6 V. Furthermore, the cycling performance of $Ni_{0.85}Se$//AC HSSC devices demonstrated capacitance retention of 81.3% after 5000 charge/discharge cycles.

6.2.2 Co-based positive electrodes

Similar to nickel, Co-based materials such as $Co(OH)_2$, Co-oxides and Co-sulfides/selenides, endowing them with rich structure chemistry and distinguishable properties to be suited as positive electrodes in HSSCs. $Co(OH)_2$ has a similar structure and properties to $Ni(OH)_2$, which is also a hexagonal-layered structure. It can also be divided into α- and β-$Co(OH)_2$, and α-$Co(OH)_2$ has better supercapacitive performance than β-$Co(OH)_2$. The reactions can be expressed as follows:

$$Co(OH)_2 + OH^- \leftrightarrow CoOOH + e^- \quad (21)$$

$$CoOOH + OH^- \leftrightarrow CoO_2 + H_2O + e^- \quad (22)$$

Since the performance of most of the advanced functional materials depends intimately on their accessible SSA, considerable interest has concentrated on the controllable synthesis of $Co(OH)_2$ nano-morphologies. In addition, the use of conductive substrates further provides efficient pathways to improving the electrochemical performance during the ion transmission progress. Recently, carbonized wood (CW) is proposed as a suitable substrate to deposit $Co(OH)_2$ nanoflakes, where CW not only serves as high surface-area support to improve the mass loading but also permits fast electron conduction and ion diffusion, thus accelerating the rate performance.[190] When this electrode had been used as a self-standing positive electrode to assemble HSSC (with CW-negative electrode), the cell displayed high areal-specific capacitance of 2.2 F/cm^2 with improved rate capability (59% when the current density was increased by 20 folds) and capacitance retention of 85% over 10,000 cycles. The HSSCs device (using CW as a negative electrode) delivered superior energy density of 0.69 mWh/cm^2 at a power density of 1.126 W/cm^2, and volumetric capacitance of 14.19 F/cm^3 and energy density of 4.45 Wh/L, respectively.

Typically, cobalt oxide occurs in two different modifications, namely as CoO and Co_3O_4. The CoO is challenging to obtain since it readily takes up oxygen even at room temperature to reform to a higher oxide, while Co_3O_4 exhibits a stable spinel structure of AB_2O_4 type belonging to the cubic system. The Co_3O_4 showed higher theoretical specific capacity and better cycle stability than NiO as well as excellent corrosion resistance. The charge storage reactions of Co_3O_4 can be described as follows (Eq. 30 and then Eq. 22):

$$Co_3O_4 + OH^- + H_2O \leftrightarrow 3CoOOH + e^- \qquad (23)$$

Co_3O_4 is a widely used positive electrode material for hybrid designs; however, it suffers from lower electronic and ionic conductivity, leading to poor rate capability. In addition, the substantial volume change with pulverization during the cycling process results in short cycle life. To improve the rate capability and cycling stability, the core-shell nanostructure of

conducting Co_3O_4 nanocubes (shell) and high surface area $Co(OH)_2$ nanosheets (core) has been employed as the positive electrode (Co_3O_4/$Co(OH)_2$) in HSSCs with AC negative electrode.[191] The controllable uniform distribution of Co_3O_4 nanocubes on the $Co(OH)_2$ nanosheets results in unique, well-defined surface-interface nanostructures, resulting in improved electrochemical performances. For instance, HSSC device delivered a capacitance of 210 mF/cm^2, which is almost twice as high as that of Co_3O_4 nanocube//AC (111 mF/cm^2), fivefold higher than that of $Co(OH)_2$ microplate//AC (43 mF/cm^2) and twice as high as that of Co_3O_4 + $Co(OH)_2$//AC (133 mF/cm^2) cells. The Co_3O_4/$Co(OH)_2$//AC cell maintained a capacitance of 159 mF/cm^2 at a current density of 10 mA/cm^2, suggesting improved rate capability (75% capacitance retention) with an energy density of 9.4 mWh/cm^3 as well as excellent cycling performance with only 3% decay in the initial capacitance over 5,000 cycles. The nanostructured Co_3O_4 materials can provide large SSA as well as short diffusion and transport pathways of ions and electrons, resulting in fast reaction kinetics. The well-defined Co_3O_4 nanostructures with unique crystalline architectures and highly tuneable porosities can be achieved using a template-assisted method. MOF is a new class of hybrid materials, which can be used as templates or precursors for the synthesis of nanoporous materials. Using proper post-synthesis treatment, MOFs can be readily transformed into porous carbons, metal oxides, and metal sulphides as active materials for energy storage. In this context, "one for two" strategy has been proposed to construct two nanoporous electrodes such as Co_3O_4 and N-doped carbon on CC for flexible HSSC using single 2D-MOF precursor[192] (Figure 8a). Owing to the tuneable porosity, both electrodes showed excellent rate capability, for example, CC@Co_3O_4 retained 58.7 % while CC@NC delivered 80.8 % of initial capacitance after 16 times increment in the current density. The as-assembled CC@Co_3O_4//CC@NC cell exhibited energy density of 41.5 Wh/kg at a power density of 6.2 kW/Kg, and it maintains 27.4 Wh/Kg at a peak power density of 49.2 kW/kg, suggesting

excellent rate performance. The cell experienced only 10-15% of decay in the initial capacitance over 10,000-20,000 cycles under different bending/twisting conditions, showing structural stability with excellent cycling durability. Thus, the high rate properties can be ascribed to: (i) the nanoporous structure of the electrodes, which provides high surface areas and short ion diffusion lengths, and (ii) the direct contact between the active materials and the carbon support that offers a good electron transport highway. By taking advantage of MOF-materials, advanced electrodes with hierarchical hollow architectures can be designed and engineered for improved energy storage. Dai et al. [193] developed CoO@S-Co_3O_4 core-sheath nanoarrays on CC for binder-free electrode materials with MOFs as a versatile scaffold. The hollow S-doped Co_3O_4 sheath was prepared using a two-step synthetic protocol, which includes the surface etching of CoO nanowire for synchronous in-situ growth of well-aligned ZIF-67 and the following hydrothermal process. The synergetic effect between CC nanofibers and hollow ordered CoO@S-Co_3O_4 ensures efficient mass and electron transport. By assembling MOFs-derived nanoporous carbons as a negative electrode and CoO@S-Co_3O_4 as a positive electrode, the HSSC delivered the highest energy density of 33 Wh/kg at 1000 W/kg, together with 87.9% capacitance retention over 5000 continuous cycles. Such a high performance can be attributed to the core-sheath structure, which facilitates both mass and electron transfer simultaneously.

According to the phase diagram of Co-S, cobalt sulphides can exist in different stoichiometric compositions, such as Co_4S_3, Co_9S_8, CoS, Co_3S_4, Co_2S_3, and CoS_2 with rich structure chemistry and divergent properties. Among the diverse crystal structures of cobalt sulphides, Co_9S_8, CoS, and CoS_2 have been widely studied as electrode materials in energy storage systems.[194] In cobalt sulphide, the energy is stored and released by exploiting the Faradaic reaction of CoSx with OH and inducing the electron transition between the Co^{2+}/Co^{3+} redox couple. The reaction can be generally expressed as:

$$CoS_x + OH^- \leftrightarrow CoS_xOH + e^- \quad (24)$$

$$CoS_xOH + OH^- \leftrightarrow CoS_xO + H_2O + e^- \quad (25)$$

Much research has been dedicated to engineering core-shell nanostructures with improved surface area and fast charge kinetics to achieve high electrochemical performance. By taking advantage of 1D nanostructure of Co_3O_4, acicular-type Co_9S_8 nanorod and Co_3O_4@RuO_2 nanosheet were grown on carbon cloth and utilized as positive and negative electrodes in HSSC, respectively[195](Figure 8b). Co_9S_8 nanorod arrays were grown by a hydrothermal sulphuration of acicular Co_3O_4 nanorod arrays, while the RuO_2 was directly deposited on the Co_3O_4 nanorods. The as-fabricated HSSC can be cycled reversibly in the voltage range of 1.6 V and exhibited superior electrochemical performance with an energy density of 1.44 mWh/cm^3 at the power density of 0.89 W/cm^3 and excellent cycling performance at multi-rate currents and large currents after thousands of cycles. Compared with transition metal oxides, metal selenides possess higher electrochemical activity since the electronegativity of selenium is lower than that of oxygen. Thus, the substitution of selenium for oxygen could create a more flexible microstructure. Furthermore, transition metal selenides exhibit much enhanced electrical conductivity compared with metal oxides/sulphides. Therefore, it is expected that transition metal selenides would show excellent electrochemical properties as active electrode materials. Thus, cobalt selenide can be considered as promising battery electrode for HSSCs due to their low-cost and good electrochemical activities. The cobalt selenides are composed of two stable forms (CoSe, $CoSe_2$) and two possible compounds (Co_3Se_4, Co_2Se_3) at room temperature. Zhang et al. [196] have grown porous CoSe directly on a stainless steel substrate using the electrodeposition method and combined with AC-negative electrode to assemble HSSC. The single CoSe-electrode exhibited superior cycling stability with capacitance retention of 91 % over 5000 cycles, which can be originated from the unique porous structure of the CoSe thin films. The

maximum energy density and power density of the CoSe//AC HSSC achieved were 0.17 mWh/cm^3 and 33.16 mW/cm^3, respectively, with 96.7% of capacitance retention over 5000 cycles. The unique porous structure of CoSe where the nanoparticles were connected by thin nanosheets and supported each other maintains the structural stability and facilitates ion exchange during the charge/discharge process, thereby enhancing the electrochemical properties of the device. Three-dimensional (3D) architectures growing on flexible substrates with high specific areas, inter-connective porous channels, high conductivity and excellent structural, mechanical stability were employed to improve the rate performance and cycling stability.[197] By using selenization treatment, freshly grown Co_3O_4/carbon was transformed into hierarchical 3D $CoSe_2$ architectures on carbon fabric, which delivered excellent capacitance retention of 95.4% after 5000 cycles in conventional three-electrode design. The HSSC with $CoSe_2$/carbon fabric as a negative electrode and MnO_2/carbon fabric as a positive electrode showed enhanced electrochemical performances including the extended voltage window of 1.6 V and the energy density of 0.588 mWh/cm^3 at the power density of 0.282 W/cm^3 with 94.8% capacitance retention after 2000 cycles. The improved electrochemical activities can be ascribed to the hierarchical 3D $CoSe_2$ architectures. Besides, MnO_2 nanowires on carbon fabrics exhibit sizeable specific surface area, which offers more efficient charge/mass exchanges and easy ionic transportation.

In addition to the materials mentioned above, some new promising materials, for instance, cobalt phosphides (CoP) with both metalloid characteristics and excellent electric conductivity have been employed as a negative electrode in HSSC.[198] The hybrid design of SCs with MnO_2 NW as the positive electrode, displayed excellent supercapacitive characteristics, including a volumetric capacitance of 1.94 F/cm^3 and energy and power densities of 0.69 mWh/cm^3 and 114.20 mW/cm^3, respectively. In addition, the CoP/CC//MnO_2/CC cell showed high cycle stability with 82% capacitance retention after

5000 charge/discharge cycles, which can be assigned to 3D-nanowire arrays that provide a large surface area and short ionic and electronic diffusion paths.

6.2.3 Mixed metal-based positive electrodes

An intelligent approach to push up the electrode material's performance is to create architectures with a high specific surface area. Such an approach is anticipated to achieve a joint improvement in electrical conductivity, specific capacitance, energy and power densities, and cyclic stability. Several methods, such as the formation of nanocomposites and direct growth of materials on conducting substrates, are summarized in the previous sections. On the other hand, the integrated hierarchical 3D porous structure, coupling two types of materials and/or nanostructures on conductive substrates, brings together many competitive advantages such as easy accessibility of electrolyte ions, rich electroactive sites, short ion diffusion paths, superior current collection efficiency and the synergetic effects of different components. Keeping this in mind, Gao et al.[199] prepared a hierarchical core/shell CoO@NiO hybrid nanostructure, taking urchin-like CoO nanostructure as a backbone to deposit NiO nanoflakes on flexible activated carbon textiles (ACT). Due to the high surface/volume ratio of CoO urchins and large surface area of NiO nanoflakes, the hybrid CoO@NiO electrode enables fast charge accumulation and ion transport. The HSSC was assembled using CoO@NiO as a positive electrode and ACTs wrapped with graphene as a negative electrode with PVA/KOH polymer gel-electrolyte. The CoO@NiO/ACT//ACT/graphene cell synergically worked together to achieve improved electrochemical properties in terms of working voltage (1.6 V), the energy density of 52.26 Wh/kg and power density of 9.53 kW/kg with capacitance retention of 97.53% after 2000 cycles. Thus, a hierarchical 3D porous core/shell CoO@NiO/ACT nanostructure with high surface area facilitates the charge accumulation and ion transport. In contrast, the porous ACTs wrapped graphene with good

electrical conductivity offers an "expressway" for electrolyte ions, endowed the high rate and stable performing HSSC. Conversely, a single step electrochemical synthesis of NiO-Co_3O_4 composite on stainless steel yarn (SSY) was reported to yield a high-performance electrode for HSSC.[200] The high electrochemical properties were assigned to both the nanospherical morphology of the Ni/Co oxides and the flexible, highly conductive stainless steel yarns. Moreover, unlike regularly used carbon-based negative electrodes, highly pseudocapacitive polypyrrole coated SSY was utilized as the negative electrode. By taking advantages of battery and pseudocapacitive electrodes, the HSSC achieved a high volumetric capacitance of 14.69 F/cm^3 with an energy density of 3.83 mWh/cm^3 at a power density of 18.75 mW/cm^3. Moreover, after charging/discharging for 6000 cycles, the HSSC retained nearly 90% of the original capacitance. Despite such a high surface area, the mixed or core-shell nanostructure of oxides on conducting substrate, the interface between the core and shell may experience low conductivity due to the intrinsically poor conductivity of oxides. In this regard, a unique hierarchical Co_3O_4@C@Ni_3S_2 sandwich-structured nanoneedle arrays on Ni foam were engineered as an efficient battery-electrode where mesoporous Co_3O_4 arrays served as a core, a thin carbon layer used as the inner shell layer and Ni_3S_2 nanoflakes as the outer shell layer.[201] Here, Co_3O_4 nanoneedles not only provide a conductive connection for Ni_3S_2 but also enlarge the specific surface area, while the thin Ni_3S_2 nanoflakes increase the contact area with electrolyte, enabling fast redox reaction. In addition, a layer of carbon nanoparticles on the Co_3O_4 nanoneedle surfaces acts as an intermediate layer, which offers electron "superhighways" for charge storage and transportation as well as a "protection" layer to induce a perfect coating of ultrathin Ni_3S_2 nanoflakes on the Co_3O_4 nanoneedle arrays. By the synergetic contribution from individual constituents and the complex configuration, the Co_3O_4@C@Ni_3S_2//AC HSSC delivered an energy density of 1.52 mWh/cm^3 at 6 W/cm^3 and 0.920 mWh/cm^3 at a high-power density of 60 W/cm^3. Additionally, capacity retention of

91.43% after 5000 charge-discharge cycles was achieved, demonstrating the high rate performance and good cycling stability of the device.

6.2.4 Binary metal-based positive electrodes

Of the various battery-type electrodes, binary metal-based (including oxides/sulphides/selenides) materials have been conceived as a promising cost-effective and scalable alternative since they offer many advantages such as good electrochemical activities, abundant resources, low cost and environmental friendliness. It is reported that the binary metal oxides have higher electrical conductivity than unitary metal oxides and contain both components' contributions to the total capacitance, which result in better electrochemical performance compared to individual components. Depending on the structure, morphology, particle size, and metal ions, broad and stable reversible capacities can be achieved. This section describes the advancements in binary metal-based materials as positive electrodes in HSSCs.

Spinel cobaltites (MCo_2O_4; M = Mn, Ni, Zn, Cu, etc.) are promising battery-materials as they have high specific capacities and good rate capabilities owing to the advantages of both metal ions. Several spinel cobaltites have been reported, among them, $NiCo_2O_4$ (NCO) attracts much attention, as it possesses much better conductivity and higher electrochemical activity, at least two orders of magnitude higher than conventional transition metal oxides.[202, 203] Typically, $NiCo_2O_4$ possesses a spinel structure where Ni occupies the octahedral sites, and Co is distributed over both octahedral and tetrahedral sites.[203] The charge storage mechanism of $NiCo_2O_4$ in alkaline media during the redox process corresponds to the reversible reactions of Co^{2+}/Co^{3+} and Ni^{2+}/Ni^{3+} transitions as given in the following equations:[204, 205]

$$NiCo_2O_4 + OH^- + H_2O \leftrightarrow NiOOH + 2CoOOH + 2e^- \quad (26)$$

$$CoOOH + OH^- \leftrightarrow CoO_2 + H_2O + e^- \quad (27)$$

Synthesizing NCO with rationally designed morphology and nanoscale structure provided one of the most feasible ways to create high-performance positive electrodes for HSSCs. The hierarchical $NiCo_2O_4$ nanostructures (with airy organdy $NiCo_2O_4$ nanosheets on vertical $NiCo_2O_4$ nanoarrays) were prepared on carbon cloth and combined with 3D-porous graphene papers (PGP) negative electrode to assemble HSSC.[206] The $NiCo_2O_4$/CC//PGP cell delivered a combination of electrochemical properties including extended working voltage (1.8 V) with an energy density of 60.9 Wh/kg and power density of 11.36 kW/kg. Moreover, the capacitance retention of 96.8% over 5000 cycles was achieved under mechanical bending. Similarly, to prevent the capacity fading due to the volume change during charge/discharge processes, one effective route is to construct smart core-shell hybrid architecture electrodes. Such a hybrid configuration benefits from each of the materials. This can provide unique synergistic effects to facilitate the transfer of ions and electrons during electrochemical reactions process. In this context, ultrathin $Ni(OH)_2$ nanosheet wrapped $NiCo_2O_4$ nanowires were grown on carbon nanotube fibres (CNTF) as the positive electrode, which provides a large accessible surface area in the electrolyte and improved ionic transportation,[207] as shown in Figure 9a. Unlike typical carbon-negative electrode, highly conducting and porous vanadium nitride (VN) nanowires on CNTF were utilized as a pseudocapacitive negative electrode to assemble HSSC with a $NiCo_2O_4$@$Ni(OH)_2$/CNTF positive electrode. The cell voltage reached to 1.6 V with a capacitance of 291.9 mF/cm^2 (106.1 F/cm^3) and energy density of 103.8 μWh/cm^2 (37.7 mWh/cm^3). The flexibility and cycling stability of HSSC was tested by weaving into a glove, which retained a capacitance of greater than 90% after bending over 5000 cycles. The porous VN nanowires and $NiCo_2O_4$@$Ni(OH)_2$ core-shell hierarchical nanowires arrays with a large specific surface area contributed to shorter transportation path for the diffusion of electrolyte ions and accelerate the redox reactions

between electrolyte ions and electrode materials. The integration of metal oxide with conducting polymers is another possible approach to enhance the electron transport and ion diffusion issues of traditional metal oxides. For example, Kong and co-workers[208] engineered 3D hierarchical $NiCo_2O_4$@PPy coaxial nanowire arrays on carbon textiles where the mesoporous $NiCo_2O_4$ nanowires serve as the highly electroactive "core" and uniform PPy nanospheres work as the conductive "shell". This hybrid electrode provides several key advantages. In this nanostructure, the mesopores $NiCo_2O_4$ improve ions access and transport while the conducting PPy shell increases the electron transport within every nanowire. Moreover, the unique core-shell design allows electrolytes to penetrate in every nanowire so that both the $NiCo_2O_4$ and PPy can involve in the redox reactions to contribute to the energy storage. The $NiCo_2O_4$@PPy//AC cell achieved a high energy density of 58.8 Wh/kg and power density of 10.2 kW/kg with capacitance retention of 89.2% after 5000 cycles as well as a good flexibility. On the other hand, improved electrochemical performance induced by foreign carbonaceous materials has also been reported.[209] For instance, $NiCo_2O_4$-based graphene oxide/carbon fibre (NCGO/CF) electrodes were prepared and paired with a P-doped graphene oxide/carbon fibre (PGO/CF) negative electrode. The resulting fibre-type HSSC delivered a high energy density of 36.77 mWh/cm^3 at a power density of 142.5 mW/cm^3, and their unique hybrid structures exhibit satisfactory electrochemical performance.

Other spinel cobaltites such as $ZnCo_2O_4$, $FeCo_2O_4$ and $MnCo_2O_4$ exhibit same structure as $NiCo_2O_4$ except for X (X= Zn, Fe or Mn) that replaces Co^{2+} at the tetrahedral site in Co_3O_4, which can also be utilized as positive electrodes in HSSCs. The common electrochemical performance-limiting factor for metal oxides is their low electrical conductivity; hence, it is essential to combine them with conducting carbon and/or polymer-based materials. The hybrid $ZnCo_2O_4$/ZnO@multiwall carbon nanotube was fabricated as a positive electrode for HSSC.[210] Initially, $ZnCo_2O_4$/ZnO was deposited onto Ni foam by the

hydrothermal method, with subsequent deposition of MWCNT by a dip and dry process. The sandwich structure of $ZnCo_2O_4$/ZnO@MWCNTs with a jungle flake inside showed improved rate capability and capacitance retention of 80.2% after 3000 cycles, assigning to the improved surface area and electrical conductivity. The HSSC cell displayed a specific capacitance of 111.8 F/g (at 1 A/g) with an energy density of 48.1 Wh/kg (at 900 W/kg) and good capacitance retention of 92.9% after 3,000 cycles. Moreover, two serial connected $ZnCo_2O_4$/ZnO@MWCNT//AC HSSC could light four parallel-connected LEDs, which remained bright for 23 min. Similarly, Ma and co-workers[211] designed $ZnCo_2O_4$@MnO_2 core-shell nanotube arrays on Ni foam as a positive electrode and paired with 3D porous Fe_2O_3 on Fe foil as the negative electrode. The as-designed HSSC exhibited an extended operating voltage window of 1.3 V with a maximum energy density of 37.8 Wh/kg and capacitance retention of 91% after 5,000 cycles.

Metal molybdates ($MMoO_4$ where M = Ni, Co, etc.) with superior redox-activities have drawn extensive research attention.[212, 213] $NiMoO_4$ with multiple oxidation states offers high redox reactivity in a suitable electrolyte and can be used as battery-electrode in HSSCs. Gao et al.[214] prepared $NiMoO_4$ nanorods covered with conducting PANI to take the best properties out of these two materials to improve the electrochemical stability and charge storage capacity of SCs. The PANI with good mechanical stability can also prohibit the structural collapse of $NiMoO_4$ during charge/discharge processes. The assembled HSSCs with $NiMoO_4$-PANI composite and AC demonstrated an energy density of 33.07 Wh/kg at 240 W/kg and high capacitance retention of about 98.6% after 5000 cycles. Similarly, Chen and co-workers[215] grew $CoMoO_4$ nanowires on carbon cloth (CC) and then wrapped them with a thin layer of electrically conducting PPy, aiming to improve the cycling stability. The resulting $CoMoO_4$/PPy nanocomposite showed capacitance resistance of 95.2% after 2000 cycles, which was significantly higher than that of pristine $CoMoO_4$ nanowires. The better

cyclic stability of $CoMoO_4$/PPy hybrid can be assigned to the existence of the PPy layer. The latter serves as a mechanical buffering layer that prevents the structural evolution of $CoMoO_4$ as well as tolerates the volumetric swelling/shrinking during the rapid charge/discharge process.

Later, the HSSC device was fabricated by coupling $CoMoO_4$/PPy positive electrode with a conventional AC negative electrode. The energy density for the cell was determined to be 104.7 Wh/kg (3.522 mWh/cm^3) at a power density of 971.43 W/kg (32.6 mW/cm^3). The device delivered a maximum power density 2171 W/kg (409.6 mW/cm^3) at the energy density of 26.37 Wh/kg (0.887 mWh/cm^3), suggesting good rate performance. Moreover, the device maintained capacitance retention of 95 % over 2000 cycles under the bending angles of up to 180°.

The electronegativity of sulphur is lower than oxygen; replacement of oxygen with sulphur can create a more flexible structure, preventing the structural disintegration and making it easy for electrons to transport, which is beneficial to electrochemical performances. Due to the lower bandgap, binary $NiCo_2S_4$ possesses an electric conductivity ~100 times higher than that of NCO. Therefore, it was widely explored as electrode material for energy storage applications. Recently, Lu et al.[216] proposed the enhancement of the electrochemical activities of the $NiCo_2S_4$ electrode by interface regulation and further cobalt geometrical-site-dependent electrochemical propensity modulation. They have employed a different route to regulate the interfaces and edges in NiCo-spinel structure effectively and introduced active species such as Co^{2+} at the tetrahedral site and Co^{3+} at the octahedral site, which correspondingly anchors the specific reactions, i.e. energy storage or catalytic process. The HSSCs with $NiCo_2S_4$ positive and reduced rGO hydrogel negative electrode delivered a satisfying rate capability with the capacitance retention of 89.5% when the current density was increased four-fold. In addition, the cell showed impressive long-term cyclic stability

without a visible drop even after 5000 cycles with the energy density of 22.21 Wh/kg at the power density of 962.2 W/kg. Thus, it was uncovered that the electrochemical performance could not only be improved due to the electronic conductivity but also depends on geometrical-sites of cobalt species in $NiCo_2S_4$ nanostructure. On the other hand, to further improve the rate capability and cycling stability, $NiCo_2S_4$@$CoMoO_4$ core-shell nanowire arrays were grown on carbon cloth.[217] Benefiting from the unique hierarchical structure and their synergistic effects between $CoMoO_4$ and $NiCo_2S_4$, the electrode realizes a fast electron and ion transfer, a large electroactive surface area and superior conductivity, resulting in good rate capability (81.6%) and cycling stability (88.6% capacitance retention after 5000 cycles). The assembled HSSC device with AC-negative electrode achieved an energy density of 66.6 Wh/kg at a power density of 0.8 kW/kg and high-power density of 16 kW/kg at 49.95 Wh/kg with good capacitance retention of 85.6% over 5000 cycles. Similarly, $CoMoO_4$@$Co_{1.5}Ni_{1.5}S_4$ rambutan-like hybrids were also investigated as positive electrode for HSSC, they delivered an energy density of 127.86 Wh/kg at a power density of 2003.88 W/kg and showed prominent capacitance retention of 96.3 % after 2000 cycles.[218] These electrochemical performances were assigned to the special structure of the $CoMoO_4$@$Co_{1.5}Ni_{1.5}S_4$ hybrids, with $CoMoO_4$ as a core and $Co_{1.5}Ni_{1.5}S_4$ as branches; these provide high surface area and reveal synergistic effects. In addition to this, Kumbhar et al.[219] developed the HSSC by using the $NiCo_2O_4$ as a positive electrode and AC as a negative electrode. Initially, the Ni-Co hydroxide was prepared by three different electrodeposition routes, and further, it was converted into the $NiCo_2S_4$ via a hydrothermal process. The developed $NiCo_2S_4$// AC HSSC shows the energy density value of 69.7 Wh/kg with a power density of 8 kW/kg. Further, carbon-containing $NiCo_2S_4$ hollow-nanoflake structures were fabricated by Mohamed et al. [220] via one-step solvothermal method using CS_2 as a single source for sulfidation and carbonization. The as-fabricated asymmetric supercapacitor based

on carbon-containing $NiCo_2S_4$ nanoflakes and AC electrodes revealed a high energy density of 38.3 Wh/kg and a high power density of 8.0 kW/kg with capacitance retention of 91.5% and a coulombic efficiency of 95.6% after 5000 cycles. In addition, some more different binary metal sulphides such as $CuCo_2S_4$,[221] graphite nanosheet@$CoMoS_4$,[222] $CoNi_2S_4$/Ni[223] have been investigated as positive battery electrodes for hybrid solid-state supercapacitors with a suitable capacitive-negative electrode to achieve high energy density, good rate performance and excellent cycling stability.

Mixed bimetallic sulphides have also been tested as positive electrode for the HSSC cell. Recently, Javed et al. [224] have prepared the $Zn_xCo_{1-x}S$ nanoparticle-embedded in nitrogen-doped carbon on flexible carbon cloth ($Zn_xCo_{1-x}S$-NC) as a binder-free positive electrode for the flexible HSSC. This unique hierarchical mesoporous composite structure was simply derived from a metal-organic framework (MOF) precursor, followed by calcination and a tuned sulfurization process. Flexible HSSC based on $Zn_xCo_{1-x}S$-NC as the positive electrode and bimetallic MOF-derived nitrogen-doped mesoporous carbon (MPC) as the negative electrode (ZCS//MPC-ASC) were assembled and exhibited excellent energy density of 92.59 Wh/kg with inspiring cycling stability by retaining 91.82% of its initial capacitance after 5000 cycles. Further, Sun et al.[225] developed the HSSC by using the redox-active positive and negative electrode. They proposed the effective metal-organic framework (MOF)-derived approach to construct high performance positive and negative electrode materials with a core-shell heterostructure. Binary MOF arrays were converted to zinc–cobalt sulphide nanosheets (ZnCoS-NSs) scaffolds with excellent conductivity and a flexible structure, which can offer an electrically and ionically conductive 3D continuous network for the growth of active materials. Further, the $Ni(OH)_2$ and VN were decorated on the ZnCoS-NSs to form the positive $Ni(OH)_2$@ZnCoS-NSs and negative VN@ZnCoS-NS for HSSC application. The assembled HSSC device exhibited ultrahigh energy density (75 W h/kg at a

power density of 0.4 kW/ kg), stable electrochemical stability (82% capacitance retention even after 10 000 cycles), and excellent flexibility (92% capacitance retention after bending 4000 times).

6.2.5 Layered double hydroxide (LDH)-based positive electrodes

Metallic layered double hydroxides have attracted increasing attention as promising battery electrodes due to their extremely reversible redox activities, rich abundance, low price and natural friendliness. Importantly, the easy intercalation/deintercalation of ions without altering the structure is favourable for the stable energy storage application. In addition to this, the facile exfoliation into monolayer nanosheets and easy chemical modification makes them excellent electrode for the energy storage application among the other hydroxide electrodes. However, the unsatisfactory structural stability and conductivity severely restrict their practical applications in high-performance HSSCs. Hollow nanostructures possess many advantages such as large surface area favouring electrolyte accesses and charge transfer, thus leading to enhanced electrochemical activities.

In the past few years, numerous studies were carried out on the NiCoAl-LDH for the energy storage application due to its high energy storing capacity and tunable structure. Some of the primary studies focused on the synthesis of single-phase NiCo-LDH by changing the ratio of the nickel and cobalt precursors.[226, 227] Recently many efforts have been taken to combine NiCo-LDH with different conducting materials such as graphene nanosheets[228], reduced graphene oxide (rGO)[229] and V_4C_3 Mxene.[230] For example, Wang et al.[230] prepared the composite electrodes by combining the NiCoAl-LDH and V_4C_3 Mxene in a single electrode to take the benefits of the battery-type and capacitive-type charge storage mechanism. As a result, the hybrid supercapacitor with NiCoAl-LDH/V_4C_3 as the battery-type electrode and activated carbon (AC) as the capacitive electrode, show superior energy

densities of 71.7 and 45.0 W h/kg at power densities of 830 and 20 000 W/kg in 1 M KOH, respectively. Similarly, Gao et al.[231] systematically investigated the effect of the Al in the ternary LDH on the supercapacitive performance. They prepared the $NiCo_2Al$-LDH by changing the proportion of the Al and studied its impact on the structure, morphology, and electrochemical features of the electrode. At the appropriate level of Al (x=2), the mixed nanowires-nanosheets-based morphology exhibited the 2.3-fold capacitance of $NiCo_2$-OH. Further, the hybrid supercapacitor was developed by using the $NiCo_2Al$-LDH as a positive electrode, and MOF derived porous carbon as a negative electrode with PVA-KOH gel electrolyte. The developed hybrid supercapacitor shows the highest energy density of 44 Wh/kg at the power density of 462 W/kg with remarkable cyclic stability with 91.2% capacitance retention over 15 000 charge-discharge cycles. Some other approaches have also been reported in the literature to enhance the energy storing capacity of the LDH based electrodes. Zhao et al.[232] fabricated the core-shell based electrodes by preparing the NiCo-LDH nanosheets on the $CoMoO_4$ nanowires by a two-step hydrothermal process. Further, they developed the hybrid supercapacitor by using the $CoMoO_4$@NiCo-LDH as a positive electrode and AC as a negative electrode with PVA-KOH gel electrolyte. The developed hybrid supercapacitor achieves a maximum energy density of 59.5 Wh/kg at a power density of 800 W/kg and long-term cycling stability over 5000 cycles. The Ni–V LDH has been reported by the Tyagi et al.[233] for the HSSC. They developed the hybrid supercapacitor by using the Ni–V LDH as a positive electrode and AC as a negative electrode with PVA/LiCl gel electrolyte. The HSSC works at a voltage limit of 1.6 V with a maximum energy density of 0.24 mWh/cm^3. In addition to this, NiFe-LDH was also reported for the HSSC application. Wang et al.[234] proposed the NiFe-LDH/RGO/CNFs composite as a positive electrode for the flexible asymmetric supercapacitor. Initially, they prepared the NiFe-LDH/RGO/CNFs composite via the one-pot hydrothermal process and later assembled the flexible NiFe-LDH-

RGO-CNFs//AC HSSC. The developed asymmetric supercapacitor shows the capacitance of 98.4 F/g with an energy density of 33.7 Wh/kg at a power density of 785.8 W/kg. Given all these excellent electrochemical features for the LDH based supercapacitor cell, the fundamental understanding of each component of the LDH during the charge-discharge process is necessary.

6.2.6 Other battery-type positive electrode

In addition to the materials mentioned above, some new promising compounds have also been utilized for the hybrid supercapacitors to achieve higher electrochemical performance. For example, novel 1D $Co_{2.18}Ni_{0.82}Si_2O_5(OH)_4$ ultrathin nanoflakes architecture was paired with graphene nanosheets (GNSs) to realise an HSSC.[235] Interestingly, the as-assembled $Co_{2.18}Ni_{0.82}Si_2O_5(OH)_4$//graphene HSSC cell displayed a specific capacitance of 194.3 mF/cm^2 at a current density of 0.50 mA/cm^2 while retaining the value of 141.6 mF/cm^2 at a current density of 6.0 mA/cm^2 (~73% capacitance retention). Further, the cell could deliver a maximum energy density of 0.496 mWh/cm^3 and excellent cycle stability with 96.3% retention over 10,000 cycles. Zhao et al.[236] prepared the novel $Ni_{20}[(OH)_{12}(H_2O)_6][(HPO_4)_8(PO_4)_4]\cdot_{12}H_2O$ nanorods via the one-pot hydrothermal method and applied them for the flexible hybrid supercapacitor. The developed $Ni_{20}[(OH)_{12}(H_2O)_6][(HPO_4)_8(PO_4)_4]\cdot_{12}H_2O$//graphene hybrid supercapacitor works at operating voltage of 1.6 V with a maximum energy density of 0.446 mWh/cm^3 at a current density of 0.5 mA/cm^2. Moreover, the metal silicate has also been reported for the supercapacitor application. Wang et al.[237] prepared the metal silicate (MnSi, CoSi and NiSi) by using the Stöber method-fabricated SiO_2 sphere as a template (Figure 9b). The developed HSSC with the metal silicate as a positive electrode and AC as a negative electrode with PVA-KOH gel electrolyte shows impressive electrochemical features. The MnSi//AC,

CoSi//AC and NiSi//AC device demonstrated an areal capacitance of 1048.3, 375.5 and 120.9 F/cm^2, corresponding to a high energy density of 4.6, 2.6 and 0.93 mWh/cm^3, respectively. Recently, Chodankar et al.[238] have prepared the battery-type phosphorus-containing amorphous tri-metal nickel–ruthenium–cobalt hydroxide (P@NRC-OH) nanofibers via one step binder-free potentiodynamic polarization approach. The prepared P@NRC-OH electrode exhibited enhanced energy storage properties in terms of specific capacity (541.66 mAh g^{-1} at 3 mA cm^{-2}), cycling durability (90.35% retention over 20 000 cycles), and rate capability (308.64 mAh g^{-1}, at 20 mA cm^{-2}). The assembled full-cell HSSC with P@NRC-OH nanofibers as the positive electrode and porous AC as the negative electrode produced maximum specific energy of 90.02 W h/kg at a specific power of 1363 W/kg which remained as high as 37.87 W h/kg at a power density of 6818.18 W/kg, also showing long cycling stability over 15,000 charge-discharge cycles.

Hierarchical core/shell nanostructures are of great interest owing to their large surface area, short diffusion paths, and fast ion/electron transport pathways and component synergistic effects that are feasible for high-performance SCs. Recently, Chodankar et al.[239] reported the self-assembled vertically aligned microsheets-structured 2D $Ni_2P_2O_7$ decorated with amorphous Ni-Co-hydroxide as a positive electrode for the hybrid supercapacitor (Figure 9c). The assembled $Ni_2P_2O_7$/Ni-Co-hydroxide//AC hybrid worked at a high voltage limit of 1.6 V with an energy density of 78 Wh/kg (1.065 mWh/cm^3) and revealed extraordinary cyclic stability over 10000 charge-discharge cycles with excellent energy efficiency (75%–80%) for all current densities. Similarly, Liu et al. [240] developed transparent HSSC by using the core-shell structured electrodes. Initially, they prepared the Ag nanowire-decorated NiCo/$NiCo(OH)_2$ to form the core-shell electrode, which was used as a positive electrode to assemble the hybrid supercapacitor. Impressively, the hybrid supercapacitor composed of the Ag NW@NiCo/$NiCo(OH)_2$ cathode and the Ag NW/graphene anode

achieves a maximum areal capacitance of 9.6 mF/cm^2 at a current density of 0.2 mA/cm^2, the high energy density of 3.0 Wh/kg and power density of 3.5 W/kg.

Metal selenides have been regarded as a new class of battery-type electrodes because of their superior electronic conductivities, enriched redox-active sites, lower band gaps, large specific surface areas, and ultrahigh specific capacities as compared to their corresponding metal oxide analogues. Recently, Nguyen et al.[241] have prepared the ternary metal selenides of nickel−vanadium selenide ($NixV_3-xSe_4$) and nickel−iron selenide ($NixFe_3-xSe_4$) series by a simple and low-cost hydrothermal method, followed by selenization for flexible HSSC application. They have studied the impact of the Ni^{2+} on the electrochemical features of the $Ni_xV_{3-x}Se_4$ and nickel−iron selenide $Ni_xFe_{3-x}Se_4$ electrodes. As a result, the developed $Ni_xV_{3-x}Se_4$//$Ni_xFe_{3-x}Se_4$ HSSC cell shows the energy density value of 73.5 Wh/kg at a power density of 0.733 kW/kg and superior cycling performance (96.6% capacitance retention after 10 000 cycles). Similarly, Zhai et al.[242] fabricated the mixed Co-Cd selenide (Co-Cd-Se) nanorods and used the material as a positive electrode to develop the HSSC cell. In addition to this, the bismuth selenide has also been tested for the HSSC.[243]

Transition metal phosphides (TMPs) have recently emerged as a positive electrode material for use in HSSC thanks to their intrinsically outstanding specific capacity and high electrical conductivity. Recently, Yang et al.[244] have prepared the highly conducting 2D GeP_5 via high-temperature and high-pressure oriented growth technique (HTHP-OGT). The prepared 2D GeP_5 shows the excellent electrical conductivity of 2.4 x 10^6 S/m, which is quite favourable for high-performance HSSC applications. As a result, the prepared 2D GeP_5 exhibits excellent electrochemical performances (including an ultrahigh scan rate of 1000 V/s), a high specific capacitance of up to 35.86 F/cm^3 at 5 mV/s, a great power density of 397.24 W/cm^3 and energy density of 4.98 mWh/cm^3. Furthermore, binary TMPs have also been reported in the literature as a positive electrode for the HSSCs to overcome the

limitations of the unitary TMPs. For instance, bimetallic $Co_xNi_{1-x}P$ ultrafine nanocrystals supported on carbon nanofibers ($Co_xNi_{1-x}P$/CNF) have been synthesized by Zhang et al. [245] for the highly efficient HSSC application. They find that the Co:Ni ratio has a significant impact on the specific capacitance/capacity of $Co_xNi_{1-x}P$/ CNF, and $Co_xNi_{1-x}P$/CNF with an optimal Co:Ni ratio exhibits an extraordinary specific capacitance/capacity of 3514 F/g/1405.6 C/g at a charge/discharge current density of 5 A/g, which is the highest value for TMP-based electrode materials reported by far. The density functional theory (DFT) calculations imply that the significant capacitance/capacity enhancement in binary $Co_xNi_{1-x}P$/CNF, compared to the unitary NiP/CNF and CoP/CNF, originates from the enriched density of states near the Fermi level. An HSSC cell was developed with $Co_xNi_{1-x}P$/CNF as a positive electrode material, AC as a negative electrode material, and a KOH-PVA polymer gel as the electrolyte. The HSSC cell shows a specific capacitance/capacity of 118.7 F/g/166.2 C/g at 20 mV/s, delivers an energy density of 32.2 Wh/kg at 3.5 kW/kg, and demonstrates good capacitance retention after 10000 charge/discharge cycles. Similarly, Nguyen et al.[246] prepared the 3D Zn-Ni-P nanosheets arrays via simple, scalable and cost-effective hydrothermal and subsequent effective phosphorization technique. Furthermore, the developed Zn–Ni–P NS//Fe_2O_3@NG HSSC cell delivers an ultra-high volumetric capacity of 1.99 mAh/cm^3, excellent energy density of 90.12 W h/kg at a power density of 611 W/kg and extraordinary cycling stability (93.05% of initial capacity after 20 000 cycles at a high current density of 15 mA/cm^2). The detailed summary of recent advancement in electrochemical performance of flexible solid-state hybrid SCs based on different positive and negative electrodes is presented in Table 2.

6.2.7 Extrinsic pseudocapacitive materials in HSSCs

As mentioned earlier, the layered materials such as V_2O_5, TiO_2, MoS_2 and WS_2 exhibit diffusion-controlled (battery-like) behaviour in their bulk state, however, they behave like pseudocapacitive materials while turning to nanostructures and therefore called as extrinsic pseudocapacitors. This section describes the utilization of such materials in the fabrication of HSSCs. For example, titanium dioxide (TiO_2) can be considered as a promising electrode material for HSSCs due to its excellent electrochemical stability at negative potential range (up to -1.6 V vs SCE) in neutral aqueous electrolytes.[247-249] However, most of the TiO_2 polymorphs exhibit the tunnel-type structure or layered structure constructed by the corner-shared or edge-shared [TiO_6] octahedra chains (Figure 10a). The compact crystal structures of these TiO_2 polymorphs with small interlayer spaces and tight (1×1) tunnels suffer from slow ion diffusion in the crystal, leading to low specific capacitance and poor rate-performance.[250-252] Thus, to improve the charge storage capacity and advance ion-diffusion, K^+ intercalated hollandite TiO_2 electrode with large (2×2) atom tunnels ($K_{0.06}TiO_2$) has been developed via a phase transformation from anatase TiO_2 to hollandite TiO_2 with partial extraction of the intercalated K^+ ions.[253] The large (2 × 2) tunnels offer large space for ion storage, they also facilitate the intercalation/de-intercalation and transportation of ions in the crystal, endowing the hollandite TiO_2 high pseudo-capacitance with high-rate performance (Figure 10a). The $K_{0.06}TiO_2$ has been utilized as a novel negative electrode with MnO_2 positive electrode to assemble a high voltage (2.4 V) $MnO_2//K_{0.06}TiO_2$ flexible HSSC device, which further delivered a high capacitance of 295.5 mF/cm^2 and energy density of 63.9 mWh/cm^3. Moreover, after 10,000 cycles, the device retained 72.7% of the initial capacitance, indicating good cycling performance. Conversely, Lu and co-workers proposed core-shell structured hydrogenated TiO_2@MnO_2 for the HSSC application; the corresponding SEM images are shown in Figure 10 (b).[254] Combining MnO_2 with the TiO_2 can drastically enhance the electrical conductivity and the stability of the core-shell structured electrode.[255]

More importantly, the carrier density of pristine TiO_2 can be increased by three orders of magnitude upon hydrogenation. Based on these merits, hydrogen-treated TiO_2 (H-TiO_2) nanowires were employed as the core (conducting scaffold) to support electrochemically active MnO_2 and carbon shells (H-TiO_2@C). Thus, HSSC was fabricated using H-TiO_2@MnO_2 and H-TiO_2@C as positive and negative electrodes, respectively, which delivered volumetric and specific capacitance values of 0.71 F/cm^3 and 141.8 F/g, respectively, at 10 mV/s. It also delivered a good energy density of 0.30 mWh/cm^3 (59 Wh/kg) and a power density of 0.23 W/cm^3 (45 kW/kg) with good cycling performance with 8.8% capacitance loss over 5,000 cycles. The utilization of metal oxides as positive and negative electrodes in HSSCs enhances the energy density of SCs to some extent; however, it is still far from the energy density of batteries. Therefore, in addition to the hybrid cell designs, further strategies need to be developed to improve the energy density of SCs. Ecologically compatible deep eutectic solvent-based electrolytes are implemented to assemble high-voltage SCs that can significantly improve the energy density of a device and also work in a broad range of operating voltage.[256-259] For instance, PVA-acetamide-$LiClO_4$ (PAL) deep eutectic solvent-based gel electrolyte was sandwiched between vanadium oxide (VOx) and manganese oxide (MnOx) nanofibers on a conductive paper as positive and negative electrodes, respectively.[260] The constituted VOx//MnOx HSSCs delivered a great specific capacitance of 100 F/g in an ultra-high-voltage region (4.2 V). Because of the wide voltage range, the device exhibited outstanding energy density of 245 Wh/kg at 1800 W/kg, which was maintained to 98 Wh/kg even at a high power density of 95.3 kW/kg with good cycling stability (<10% loss after 6000 cycles). The deep eutectic solvent-based electrolyte affords a large applied potential of ~4.2 V due to the efficient and reversible intercalation/de-intercalation of electroactive cations (Li(urea)n^+) into the electrode materials and a large variation of the oxidation states of electrodes.[256, 257] Similarly to oxide, vanadium-based

nitrides can be potential candidates as negative electrodes for HSSCs due to their relatively high electrical conductivity. For instance, vanadium nitride (VN) with large specific capacitance (1,340 F/g) and high electrical conductivity (σ_{bulk} = 1.67 x 10^6 /Ωm) operates in a negative potential region. HSSC was fabricated using porous VN nanowires as the negative electrode and VOx nanowires as the positive electrode[261] (Figure 10c). Notably, the VN//VOx device exhibited a stable electrochemical window of 1.8 V and achieved a volumetric capacitance of 1.35 F/cm^3 (based on the volume of the entire device; 60.1 F/g, per the total mass of active materials) with remarkable rate capability of 74.7%. Indeed, a high energy density of 0.61 mWh/cm^3 and a high power density of 0.85 W/cm^3 were achieved with long-term cycling stability (87% retention after 10,000 cycles). Moreover, the device delivered good electrochemical performances even under different deformation conditions such as folding and twisting, which confirms its potential for application in wearable electronics.

As an alternative to EDLC based carbon materials, few pseudocapacitive metal sulphides with high capacitance and stability have also been investigated as a negative electrode for HSSCs, including MoS_2 and WS_2.[262, 263] MoS_2 is a particularly attractive pseudocapacitive electrode material owing to its large van der Waals gap of 6.2 Å in micro-sized samples, which can increases up to 6.9 Å in nanostructured samples.[264, 265] The increased van der Waals spacing should further reduce the guest-host interaction, making an ideal pseudocapacitive material. Owing to the two-dimensional (2D) atomic layered structure, MoS_2 has recently been considered to be a proper choice for SCs, which can provide large surface area and permeable slit-shaped channels to facilitate ion insertion/extraction within an individual monolayer.[266, 267] However, its sluggish ionic kinetics and poor cycling stability limit their electrochemical performance. The nanocomposite of MoS_2 with carbon-based materials would help to improve the electronic conductivity and enhance the structural

stability so that it can potentially be useful to fabricate high-performance SCs. Thus, MoS_2 nanosheets coated carbon nanotube fibres (MoS_2@CNTFs) were developed as a negative electrode and combined with Na-doped MnO_2 nanosheets on CNTFs (Na-MnO_2@CNTFs) to construct HSSCs. The designed fibre shaped HSSCs cell exhibited a large operating potential window of 2.2 V with a remarkable specific capacitance (265.4 mF/cm^2), as well as high energy density (178.4 μWh/cm^2). Besides, the device showed excellent flexibility with the capacitance retention of 92.4% after bending 3500 times and maintained stability at various angles. In a similar line, Yang and co-workers[268] developed HSSCs using the flower-like MoS_2 and MnO_2 grown on graphene nanosheets (GNS) as negative and positive electrodes, respectively. Both MoS_2/GNS and MnO_2/GNS nanostructures were prepared by the controlled hydrothermal process where MoS_2/GNS hybrid displays a typical crinkly and rippled structure with ultrathin MoS_2 nanosheets uniformly grown on the graphene.

Additionally, the MoS_2/GNS electrode exhibits superior electrochemical performance, such as high specific capacitance (320 F/g at 2 A/g) in a negative potential window which is quite suitable for the HSSCs application. The assembled MnO_2/GNS// MoS_2/GNS HSSCs delivers a remarkable energy density of 78.9 Wh/kg at a power density of 284.1 W/kg. To overcome the sluggish electrode kinetics of MoS_2, Liu et al.[269] proposed the phosphorus heteroatom doping strategy to enhance the electrical conductivity of MoS_2 and to lower the diffusion barrier of Na^+ ion. According to density functional theory (DFT), the lowest energy barrier of Na-diffusion in P-doped MoS_2 (0.11 eV) is considerably lower than that for pure MoS_2 (0.19 eV), signifying the improvement in rate performance upon P-doping. As a result, the developed HSSCs with P-doped MoS_2 as a negative electrode and MnO_2 as a positive electrode exhibits an ultrahigh energy density of 67.4 Wh/kg at 850 W/kg and excellent cycling stability with 93.4% capacitance retention after 5000 cycles at 8 A/g. Our group[270] has recently developed the high-mass loaded HSSCs with 2D MoS_2/CF and MnO_2/CF as

negative and positive electrodes, respectively, and with PVA-Na_2SO_4 as gel electrolytes. Record-high capacitances (close to their theoretical values) have been reported for the materials such as MnO_2 and MoS_2. Importantly, the achieved capacitances are possible only when the electrode mass loading is less than 1 mg/cm^2. However, the electrode mass loading less than the 1 mg/cm^2 is meaningless for commercial applications. Our group has recently developed high mass loaded MnO_2/CF (6.6 mg/cm^2) and MoS_2/CF (7.2 mg/cm^2) using a controlled hydrothermal process for HSSCs. These hierarchical 2D nanosheets delivered outstanding areal capacitances of 1187 and 495 mF/cm^2 at high current densities with excellent cycling stabilities. The assembled HSSC cell shows an energy density of 2.305 mWh/cm^3 at a power density of 50 mW/cm^3 and capacitance retention of 92.25% over 11,000 cycles and a minimal diffusion resistance (1.72 $\Omega/s^{1/2}$). Likewise, Liu et al.[271] reported the first example of crystalline WS_2 nanosheets as a promising negative electrode for HSSCs by pairing it with MnO_2@TiN nanostructure as a positive electrode. Indeed, the stable electrochemical voltage window of as-fabricated WS_2//MnO_2@TiN device was estimated to be 1.8 V with a capacitance of 4.2 F/cm^3. Moreover, the device delivered a maximum energy density of 0.97 mWh/cm^3 at a power density of 702.1 mW/cm^3 that was retained to 0.36 mWh/cm^3 at a high-power density of 1.14 W/cm^3, demonstrating excellent rate capability.

7. Perspectives and Challenges

Solid-state asymmetric supercapacitors (ASSCs) and hybrid supercapacitors (HSSCs) with high power density, short charging time, long cycling life represent one of the key energy storage systems in portable and wearable electronics. The research in the field of ASSCs and HSSCs is principally focused on enhancing the energy density of SCs without compromising its power and cycling stability. In this context, several nanostructured electrode materials and combinations of different positive and negative electrodes (capacitive

and faradic) in devices have been explored. However, the more in-depth understanding of the charge storage mechanisms and respective terminologies needs to be better provided. It is well elaborated that despite the impressive advancements, still, innovative approaches are necessary to enlarge the working voltage window of the ASSCs to boost the energy density. We have summarised some of the current challenges and the future research directions for the asymmetric supercapacitor;

- **Terminologies used for Materials:** The redox chemistries of materials in SCs can be broadly divided into two categories such as pseudocapacitive (surface redox and intercalation) and faradic (bulk reactions) electrodes. Based on the electrochemical signatures (CV and CD curves), both materials can be easily distinguished. However, several reports on Ni, Co and Ni-Co battery type electrodes have designated them as pseudocapacitive materials although they display sharp and distinct redox peaks. Therefore, a clear understanding of the electrochemical properties of materials and their charge storing mechanisms should be developed.
- **Suitable metrics and calculations:** A standardised calculation method and electrochemical performance metrics need to be designed and developed for different materials. For example, every year numerous studies on the nickel, cobalt and nickel-cobalt based electrode materials with faradic charge storing mechanisms report the specific capacitance in the range of thousands of Farads per gram, which is merely meaningless. For such electrode materials, their capacity (either in C/g or mAh/g) should be reported. Also, reporting the volumetric electrochemical parameters are essential for the ASSCs as the mass loading of the active material over the current collector is negligible in comparison with the weight of the whole device.
- **Terminologies for Device Configurations:** As previously discussed, the proper terminology should be used for the device configurations based on the electrode

materials and their charge storing mechanisms. For instance, the device containing two different electrode materials with similar (capacitive) charge-storing mechanisms should be termed as asymmetric supercapacitors (EDLC//EDLC, Pseudocapacitive//Pseudocapacitive and EDLC//Pseudocapacitive). On the other hand, the device with different positive and negative electrode materials and different charge storage mechanisms such as one battery-type and one capacitor-type electrode should be strictly called "hybrid capacitor". The hybrid capacitors are also considered as a subclass of the asymmetric cell design. However, to avoid confusion, the devices need to be clearly defined.

- **Materials Properties:** Searching the suitable electrode material with higher electrical conductivity, large specific surface area and controllable pore structures are essential for the enhanced electrochemical performance. In the last decade, the 2D electrode materials such as MXenes, metal nitrides, MOFs and metal dichalcogenides have been explored for ASSCs. However, the obtained electrochemical performances of these electrode materials are not sufficient for the practical applications.
- **Enhancing working voltage window:** The selection and optimisation of the electrolyte for the ASSCs are fundamentally necessary to improve the energy storing capacity. The majority of research on the ASSCs is conducted on electrode materials. However, the electrolyte is equally responsible for the resultant electrochemical performance. Typically, both electrode materials and the electrolyte can affect the resultant cell voltage. Therefore, it is essential to develop the electrolyte having high ionic conductivity, thermal stability, and higher overpotential for the hydrogen evolution reaction (HER) and the oxygen evolution reaction (OER). The use of redox-active electrolytes is another approach to enhance the energy density of ASSCs. Besides, the

proper selection of the positive and negative electrode materials is necessary to improve the voltage limit of the cell.

- **Self-discharge:** The high rate of self-discharge is another critical issue for the ASSCs. The significant effort is taken in the last decade to enhance the energy density, power density and the cycling stability of the asymmetric supercapacitor. However, not many of the studies discuss the self-discharge issue. To effectively use the asymmetric supercapacitor at the commercial level, it is necessary to overcome the self-discharge issue.

In summary, the present review has provided the proper terminologies for electrode materials and devices with a fundamental understanding of their charge storage mechanisms, design, fabrication and the evaluation of the appropriate electrochemical performance metrics and recent advancement an in an asymmetric fashion. The recent progress in flexible ASSCs suggests that solid-state ASSCs would play a vital role in the emergence of lightweight, flexible and wearable capacitive devices in the near future.

Acknowledgement

D.P.D. acknowledges the Queensland University of Technology (start-up grant: 323000-0424/07) and Australian Research Council (ARC), Australia for the Future Fellowship (FT180100058). H.D.P. would like to acknowledge the Post-Doc Fellowship sponsored by Centre for Materials Science, QUT, Australia. D.P.D. and H.D.P. are also thankful to the Institute for Future Environment (IFE)-Catapult Grant (290111-0040/07). J.F.S.F and D.G. are grateful to the ARC Laureate Project FL160100089 and QUT Project 323000-0355/51.

TOC: The demonstration of distinction between asymmetric and hybrid supercapacitor on the basic of electrode combinations respective to their charge storing mechanisms.

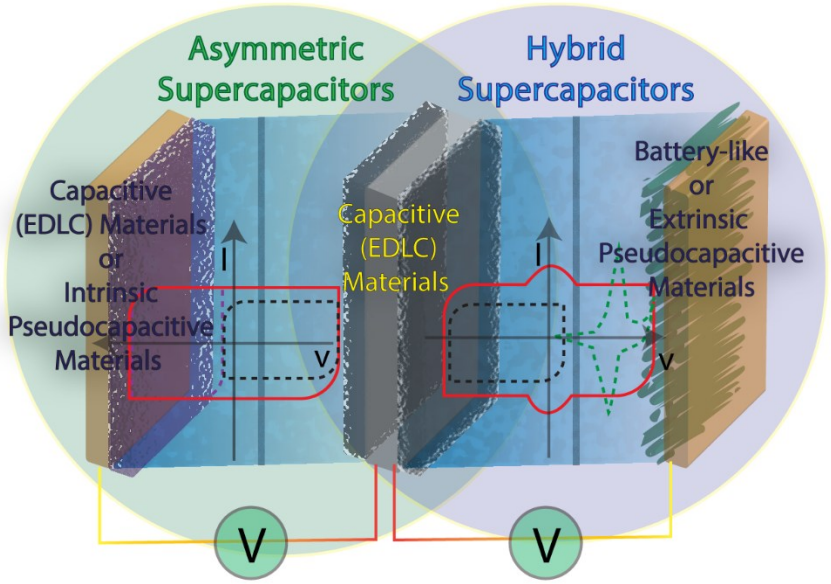

Table of Contents (TOC): Pseudocapacitive materials are in high demands due to their unique characteristic of high energy storing capacity but at high rates for long periods of time. However, with the recent scientific advancements, the boundary between pseudocapacitive and battery materials is blurred. This review provides a true meaning of pseudocapacitors with their electrochemical signatures. The distinction between asymmetric and hybrid supercapacitor based on electrode combinations is demonstrated.

Table 1: Summary of recent progress in asymmetric supercapacitors with both capacitive electrodes

Negative Electrode	Positive Electrode	Electrolyte	Voltage window (V)	Specific capacitance	Max. Energy density
Ni/AC	Ni/MnO_2	Na_2SO_4/PVA	2.5	1.4 F/cm^3 @ 2.5 mA/cm^3	0.78 mWh/cm^3
Activated	PPy/MnO_2/CC	H_3PO_4/	1.8	1.41 F/cm^2 @	8.67

carbon/CC		PVA		0.5 mA/cm^2	mWh/cm^3	
AC	MoS_2/CNTs-MnO_2	PVDF-HFP/EMIMBF4/EMIMTFSI	4.0	50.5 F/g @ 0.5 A/g	124 Wh/kg	
CNT	MnO_2/CNT	Na_2SO_4/silica/PVA	1.8	56.3 F/g @ 1 A/g	5.97 Wh/kg	
Ordered microporous carbon/CNTs	MnO_2@PEDOT:PSS	Na_2SO_4/CMC	1.8	23.4 F/cm^3 (21.7 F/g) @ 0.085 A/cm^3	11.3 mWh/cm^3	
IL-CMG	RuO_2–ILCMG	H_2SO_4/PVA	1.8	175 F/g @ 0.5 A/g	19.7 Wh/kg	
$K_{0.06}TiO_2$	MnO_2	LiCl/PVA	2.4	295.5 mF/cm^2 @ 0.25 mA/cm^2	63.9 mWh/cm^3	5
Titanium carbide MXene ($Ti_3C_2T_x$)	RuO_2	H_2SO_4/PVA	1.5	60 mF/cm^2 @ 5 mV/s	19 μWh/cm^2	
MXene/CNT	MnO_2/CNT	LiCl/PVA	2.0	220 mF/cm^2 @ 0.3 mA/cm^2	100 μWh/cm^2	
Graphene/polypyrrole	Graphene/MnO_2	KOH/PVA	1.8	2.69 F/cm^3 (175.2 F/g) @ 1 mA/cm^2	1.23 mWh/cm^3	
CW/CMK-3	CW/PNC/PEDOT	KOH/PVA	1.45	31.6 mF/cm^2 (3.16 F/cm^3)@ 0.4 mA/cm^2	0.011 mWh/cm^2	
MoS_2@CNTFs	Na-Doped MnO_2@CNTFs	Na_2SO_4/PVA	2.2	265.4 mF/cm^2 @ 1 mA/cm^2	0.178 mWh/cm^2	
Fe_2N@GNSs	TiN@GNSs	LiCl/PVA	1.6	60 F/g @ 50 mV/s	15.4 Wh/kg	
OPHPC-Orange peel derived porous carbon	MnO_2@OPHPC	Orange peel juice/PVA	1.0	3.9 F/cm^2 (65.4 F/g) @ 1 mA/cm^2	-	
N-rGO	Fe_2O_3-Fe_3O_4	KOH/PVA	1.6	112 F/g @ 0.8 A/g	24.55 Wh/kg	
Hydrophilic Carbon Cloth@ Polypyrrole	Hydrophilic Carbon Cloth@ MnO_2	LiCl/PVA	1.8	62.66 F/g @ 0.5 A/g	28.2 Wh/kg	
C@TiN@CNT fiber	MnOx@TiN@carbon nanotube fiber	EMIMTFSI/PVDF-HFP	3.5	36 F/cm^3 (360 mF/cm^2) at 0.1 A/cm^3	61.2 mWh/cm^3	
H-TiO_2@C	H-TiO_2@MnO_2	LiCl/PVA	1.8	0.71 F/cm^3 (141.8 F/g) @ 10 mV/s	0.30 mWh/cm^3 (59 Wh/kg)	

Fe_2O_3/CF	α-MnO_2/CF	LiCl/PVA	1.6	1.5 F/cm^3 @ 2 mA/cm^2	0.55 mWh/cm^3	1
Graphene hydrogel (GH)/copper wire (CW)	MnO_2/graphene/ CF	KCl/PAAK	1.6	2.54 F/cm^3 @ 0.2 mA/cm^2	0.9 mWh/cm^3	
RGO	MnO_2/ZnO	LiCl/PVA	1.8	0.52 F/cm^3 @ 10 mV/s	0.234 mWh/cm^3	
CF@TRGO	CF@RGO@MnO_2	KCl/PAAK	1.6	-	1.23 mWh/cm^3	
CNT/graphene paper	Mn_3O_4/graphene paper	KCl/PAAK	1.8	72.6 F/g @ 0.5 A/g	32.7 Wh/kg	
Fe_2O_3	MnO_2	$LiClO_4$/PVA	2.0	147 F/g @ 5 mV/s	41 Wh/kg	
Fe_2O_3	CuO	Na_2SO_4/CMC	2.0	79 F/g @ 2 mA/cm^2	23 Wh/kg	
Eggplant derived AC	γ-MnS	-	1.6	110.4 F/g @ 1.0 mA	37.6 Wh/kg	

Table 2: Recent advances in hybrid supercapacitors with one battery and one capacitive electrode

Positive Electrode	Negative Electrode	Electrolyte	Voltage window (V)	Specific capacitance	Max. Energy density	Max. Power density	Cycling stability (%)	Ref.
Carbon Fiber (CF)-$Ni(OH)_2$	CF−CNT	KOH/PVA	1.3	-	41.1 Wh/kg	3.5 kW/kg	98 over 3,000 cycles	[181]
MOF-derived Ni/NiO	CNTs-COOH	KOH/PVA	1.8	136.4 F/g @ 2 mA/cm^2	61.3 Wh/kg	9.064 kW/kg	92.8 over 10,000 cycles	[184]
Ni_3S_2	3D-rGO	KOH/PVA	2.2	105 F/g @ 1 A/g	70.58 Wh/kg	33 kW/kg	90.4 over 5000	[185]

							cycles	
NiS/Ni_3S_2	AC	KOH/PVA	1.7	0.34 mAh/cm^2 @ 2 mA/cm^2	0.289 mWh/cm^2	12.825 mW/cm^2	86.7 over 8,000 cycles	[274]
$Ni_{0.85}Se$	AC	KOH/PVA	1.6	81 F/g @ 1 A/g	29 Wh/kg	5.512 kW/kg	81.25 over 5,000 cycles	[189]
$Co(OH)_2$@Carbonized wood (CW)	Carbonized wood (CW)	KOH/PVA	1.5	14.19 F/cm^3 @ 1 mA/cm^2	0.69 mWh/cm^2 (10.87 Wh/kg)	15.447 W/cm^2 (236.8 W/kg)	85 over 10,000 cycles	[190]
MOF-derived CoO@S-Co_3O_4	MOF-derived carbon	KOH/PVA	1.5	1.99 F/cm^3 @ 2 mA/cm^2	0.71 mWh/cm^3	207 mW/cm^3	87.9 over 5,000 cycles	[193]
Co_9S_8	Co_3O_4@ RuO_2	KOH/PVA	1.6	4.28 F/cm^3 @ 2.5 mA/cm^2	1.44 mWh/cm^3	0.89 W/cm^3	90.2 over 2,000 cycles	[195]
CoSe	AC	KOH/PVA	1.4	18.1 mF/cm^2 @ 0.5 mA/cm^2	0.17 mWh/cm^3	33.16 mW/cm^3	96.7 over 5,000 cycles	[196]
MnO_2	$CoSe_2$	LiCl/PVA	1.6	1.77 F/cm^3 @ 1 mA/cm^2	0.588 mWh/cm^3	0.282 W/cm^3	94.8 after 2,000 cycles	[197]
CoO@NiO/AC textile	AC-textile /graphene	KOH/PVA	1.6	147.6 F/g @ 10 mA/cm^2	52.26 Wh/kg	9.53 kW/kg	97.5 over 2,000 cycle	[199]

							s	
$NiO+Co_3O_4$	Polypyrrole	KOH/PVA	1.5	14.69 F/cm^3 @ 25 mA/cm^3	3.83 mWh/cm^3	29 mWh/cm^3	91 over 6000 cycles	[200]
$Co_3O_4@C@Ni_3S_2$	AC	KOH/PVA	1.8	-	1.52 mWh/cm^3	60 W/cm^3	91.43 over 10,000 cycles	[201]
$NiCo_2O_4/CC$	Porous graphene paper (PGP)	LiOH/PVA	1.8	71.32 F/g @ 5 mA/cm^2	60.9 Wh/kg	11.36 kW/kg	96.8 over 5,000 cycles	[206]
$Ni(OH)_2@NiCo_2O_4$ @CNTF	VN@CNTF	KOH/PVA	1.6	291.9 mF/cm^2 (106.1 F/cm^3) @ 1 mA/cm^2	0.1038 mWh/cm^2	8 mW/cm^2	87.2 over 5000 cycles	[207]
$NiCo_2O_4$-GO/CF	P-doped GO/CF	KOH/PVA	2.0	73.3 F/cm^3 @ 0.146 A/cm^3 (100 F/g @ 0.21 A/g)	36.77 mWh/cm^3 (50.6 Wh/kg)	1068 mWh/cm^3 (1.5 kW/kg)	97 over 2,000 cycles	[209]
$NiMoO_4$-PANI	AC	KOH/PVA	1.6	93 F/g @ 0.3 A/g	33.07 Wh/kg	5.2 kW/kg	98.6 after 5,000 cycles	[214]
$CoMoO_4$/PPy	AC	KOH/PVA	1.7	-	104.7 Wh/kg	971.43 W/kg	95 over 2,000 cycles	[215]

$NiCo_2S_4$	rGO-hydrogel	KOH/PVA	1.5	110.8 F/g @ 2 A/g	22.21 Wh/kg	-	No Loss after 5000 cycles	216
$NiCo_2S_4$@ $CoMoO_4$	AC	KOH/PVA	1.6	187.3 F/g @ 1 A/g	66.6 Wh/kg	16 kW/kg	85.6 over 5000 cycles	217
$CoMoO_4$@$Co_{1.5}Ni_{1.5}S_4$	AC		1.6	221.3 F/g @ 1.5 A/g	127.86 Wh/kg	6.587 kW/kg	96.3 over 2,000 cycles	218
$CuCo_2S_4$	MoO_2@ N-doped carbon	KOH/PVA	1.6	184 F/g @ 1 A/g	65.1 Wh/kg	12.8 kW/kg	90.6 over 5000 cycles	221
Graphite nanosheet@$CoMoS_4$	AC	KOH/PVA	1.8	95.11 F/g @ 1 A/g	42.85 Wh/kg	4.5 kW/kg	93.2 over 8000 cycles	222
$CoNi_2S_4$/Ni	CNTs+GR/Ni	KOH/PVA	1.8	23.5 F/g (102 mF/cm^3 @ 12 mA/cm^3	10.6 Wh/kg	3.732 kW/kg	77.3 over 1800 cycles	223
NiCoAl-LDH/V_4C_3	AC	KOH	1.6	194 F/g @ 1 A/g	71.7 Wh/kg	20000 W/kg	98 % after 10,000 cycles	230
Ti_3C_2/Ni-Co-Al-LDH	AC	KOH/PVA	1.6	128.89 F/g @ 0.5 A/g	45.8 Wh/kg	6.93 kW/kg	97.8 after 10,000 cycle	232

							s	
Ni-V-LDH	AC	KOH/LiCl	1.6	91 mF/cm^2 @ 0.1 mA/cm^2	0.24 mWh/cm^3	214.4 mW/cm^3	100 % after 15,000 cycles	[233]
$Co_{2.18}Ni_{0.82}Si_2O_5(OH)_4$	Graphene	KOH/PVA	1.75	194.3 mF/cm^2 @ 0.50 mA/cm^2	0.496 mWh/cm^3	38.8 mW/cm^3	96.3 over 10,000 cycles	[235]
MnSi	AC	KOH/PVA	1.2	1048.3 mF/cm^2 @ 2 mA/cm^2	4.6 mWh/cm^3	-	1000 cycles	[237]
$Ni_2P_2O_7$/Ni-Co-hydroxide	AC	KOH/PVA	1.6	2.99 F/cm^3 @ 2 mA/cm^2	78 Wh/kg	2814 W/kg	91.83 % after 10,000 cycles	[239]
MnO_2@$Ni_2P_2O_7$	AC	KOH/PVA	1.6	82 mAh/g @ 1 A/g	66 Wh/kg	1920 W/kg	91.83 % after 10,000 cycles	[275]
Ni-Co LDH	AC	KOH/PVA	1.6	265 F/g at 1 A/g	94.5 Wh/kg	15.6 kW/kg	80.5 over 1000 cycles	[276]
$Ni(OH)_2$/NGP	Mn_3O_4/NGP	NaOH/PVA	1.3	1.96 F/cm^3 @ 50 mV/s	0.35 mWh/cm^3	32.5 mW/cm^3	83 over 12,000 cycle	[180]

							s	
NiMn-LDH/CNT	RGO/CNT	KOH/ Nafion	1.7	221 F/g @ of 1 A/g	88.3 Wh/kg	17.2 kW/kg	94 over 1,000 cycles	[277]
$NaCoPO_4$-Co_3O_4	Graphene	KOH/PVA	1.0	28.6 mF/cm^2 @ 0.1 mA/cm^2	0.39 mWh/cm^3	50 mW/cm^3	94.5 over 5,000 cycles	[278]
$NiCo_2O_4$@PPy	AC	KOH/PVA	1.6	165.4 @ 1 mA/cm^2	58.8 Wh/kg	10.2 kW/kg	89.2 over 5,000 cycles	[208]
$Ni_{11}(HPO_3)_8(OH)_6$	Graphene	KOH/PVA	1.4	1.64 F/cm^3@ 0.50 mA/cm^2	0.45 mWh/cm^3	33 mW/cm^3	93.3 over 10,000 cycles	[279]
Carbon cloth@$CoMoO_4$@NiCo LDH	AC	KOH/PVA	1.6	167.3 F/g @ 1 A/g	59.5 Wh/kg	16 kW/kg	89.7 over 5000 cycles	[280]
$K_2Co_3(P_2O_7)_2$-$2H_2O$	Graphene	KOH/PVA	1.07	6 F/cm^3 @ 10 mA/cm^3	0.96 mWh/cm^3	54.5 mW/cm^3	94.4 over 5,000 cycles	[281]
$FeCo_2O_4$@ polypyrrole	AC	KOH/PVA	1.6	194 F/g @ 1 A/g	68.8 Wh/kg	15.5 kW/kg	91 over 5000 cycles	[282]
$Ni(OH)_2$ @ sulfonated graphene	AC	KOH/PVA	0.8	80.44 F/g @ 0.05 A/g	7.15 Wh/kg	118 W/kg	75 over 1000 cycles	[283]

$Co_{11}(HPO_3)_8(OH)_6$-Co_3O_4	Graphene	KOH/PVA	1.38	1.84 F/cm^3 @ 0.5 mA/cm^2	0.48 mWh/cm^3	105 mW/cm^3	98.7 over 2,000 cycles	[284]
Polypyrrole/$Ni(OH)_2$ /sulfonated GO	AC	KOH/PVA	1.6	224 F/g @ 1 A/g	79.6 Wh/kg	7.97 kW/kg	60 over 5,000 cycles	[285]
Ni-Mo-S	Ni-Fe-S	KOH/PVA	1.6	103 mAh/g @ 2 mA/cm^2	82.13 Wh/kg	13.103 kW/kg	95.86 over 10,000 cycles	[286]
Cobalt carbonate hydroxide/N-doped graphene	N-doped graphene	KOH/PVA	1.9	153.5 mF/cm^2 @ 1.0 mA/cm^2	0.77 Wh/m^2	25.3 W/m^2	93.6 over 2,000 cycles	[287]
S@Ni-MOF	AC	KOH/PVA	1.6	136.5 F/g @1 A/g	56.85 Wh/kg	4.1 kW/kg	86.67 over 20,000 cycles	[288]
$Ni_{0.1}Co_{0.8}Mn_{0.1}$	PAN-derived carbon	KOH/PVA	1.6	147 F/g @ 1 A/g	52.47 Wh/kg	8 kW/kg	89.5 over 10,000 cycles	[289]
Mn-Silicate	AC	KOH/PVA	1.2	1.048 F/cm^2 @ 2 mA/cm^2	4.6 mWh/cm^3	80 mW/cm^3	32 over 900 cycles	[237]
Co-Silicate	AC	KOH/PVA	1.5	0.375 F/cm^2 @ 2	2.6 mWh/cm^3	98 mW/cm^3	45 over 2,800 cycle	[237]

				mA/cm^2			s	
Ni-Silicate	AC	KOH/PVA	1.6	0.12 F/cm^2 @ 2 mA/cm^2	0.93 mWh/cm^3	102 mW/cm^3	42 over 3,000 cycles	[237]
PPy@$NiCo(OH)_2$	AC	KOH/PVA	1.4	307 F/g @ 1 A/g	-	-	93 over 5,000 cycles	[290]
$CuGa_2O_4$/NF	FeP/NF	KOH/PVA	1.5	202 F/g @ 1 A/g	63.15 Wh/kg	9 kW/kg	90 over 5,000 cycles	[291]
NiO@carbon nanofibers/CC	N-Carbon nanofibers/CC	KOH/PVA	1.5	62.4 F/g @ 20 mA/cm^2	19.5 Wh/kg	11.5 kW/kg	-	[292]
$NiCo_2O_4$	N-doped porous carbons	KOH/PVA-PEO	1.6	120 F/g @ 1 A/g	42.7 Wh/kg	8 kW/kg	94 over 10,000 cycles	[293]
$NiCo_2$Al-LDH	MOF derived porous carbon	KOH/PVA	1.5	144 F/g @ 0.5 A/g	44 Wh/kg	6286 W/kg	91.2 % after 15,000 cycles	[231]
TiN@V_2O_5	TiN@V_2O_5	LiCl/PVA	1.6	74.25 F/cm^3 @ 1 A/cm^3	26.42 mWh/cm^3	9 W/cm^3	89.8 after 4000 cycles	[31]
MnO_2@TiN	WS_2	LiCl/PVA	1.8	2.13 F/cm^3 @ 4	0.97 mWh/cm^3	1.14 W/cm^3	70.3 after 2500 cycle	[271]

				mA/cm^2			s	
MoS_2-rGO/MWCNT	rGO/MWCNT	H_2SO_4/PVA	1.4	5.2 F/cm^3 @ 0.16 A/cm^3	-	-	-	164
MnO_2@PEDOT:PSS	VN@C	Na_2SO_4/PVA	1.8	213.5 mF/cm^2 @ 0.3 mA/cm^2	0.096 mWh/cm^2	2.7 mW/cm^2	96.8 after 5,000 cycles	167
2D mesoporous MnO_2	VN	SiO_2-LiTFSI	2.0	16.1 mF/cm^2 (38.8 F/cm^3) @ 1 mV/s	21.6 mWh/cm^3	1539 mW/cm^3	90 after 5,000 cycles	170

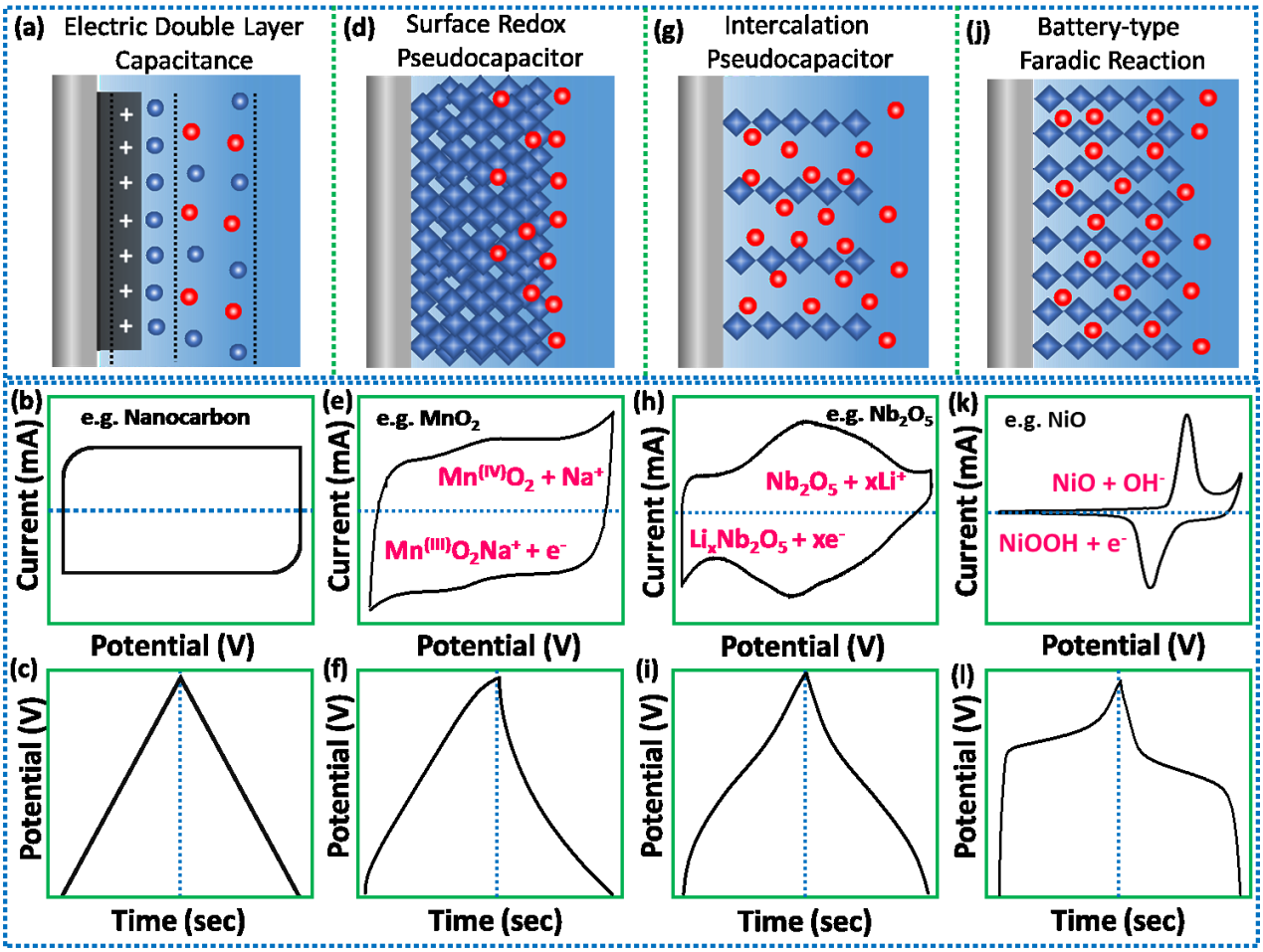

Figure 1. The schematic illustration of the energy storage mechanisms with their corresponding electrochemical signatures (representative shapes of CV and CD curves): (a-c) electrical double layer capacitance, (d-f) surface redox capacitance, (g-i) intercalation capacitance and (j-l) faradic battery-type.

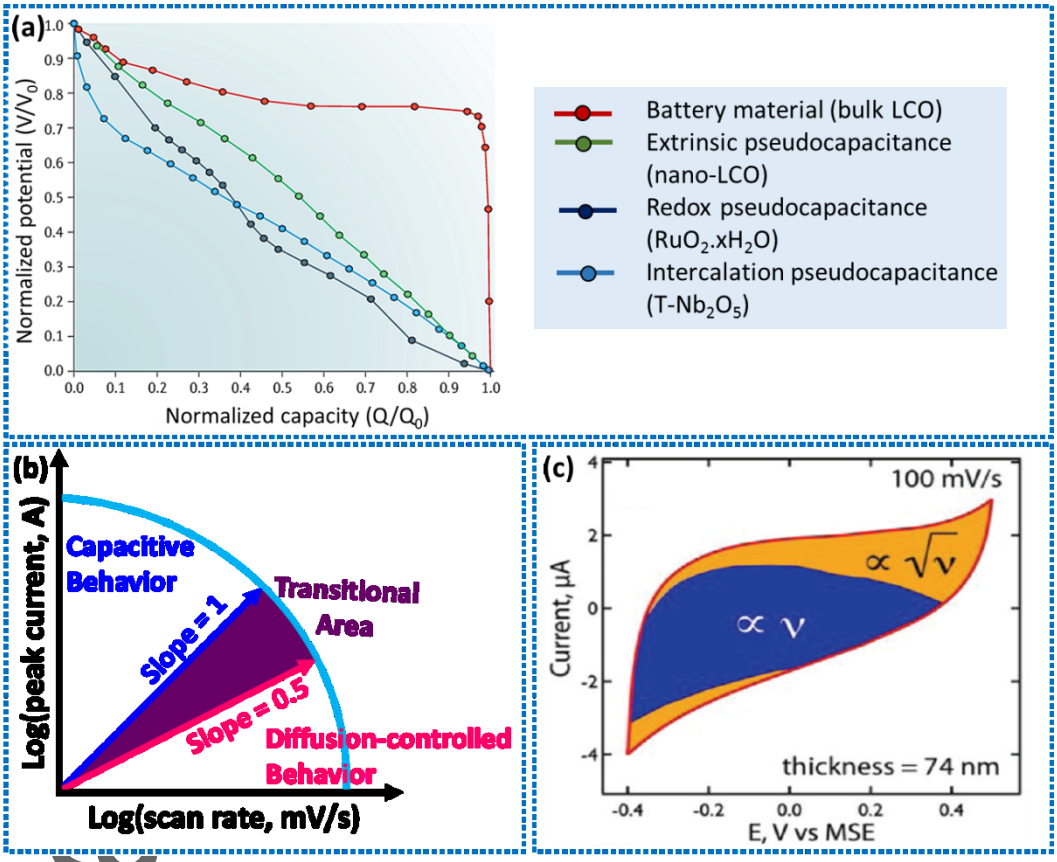

Figure 2. (a) Galvanostatic discharge curves for various kinds of pseudocapacitive materials (surface redox, intercalation pseudocapacitance, and a nanostructured extrinsic pseudocapacitive material) in comparison with bulk $LiCoO_2$ (LCO). Reprinted with permission from Ref.[14], Copyright 2019, Springer Nature. (b) Power law dependence of the peak current on sweep rate for capacitive materials (b = 1) and typical battery-type materials (b = 0.5). The "transition" area between capacitive and battery-type materials area is located in the range of b = 0.5–1.0. (c) CV at 100 mV/s of Au/MnO_2 core-shell nanowires separated into capacitive (varying with v) and diffusion (varying with $v^{1/2}$) contributions. Reprinted with permission from Ref.[294], Copyright 2012 American Chemical Society.

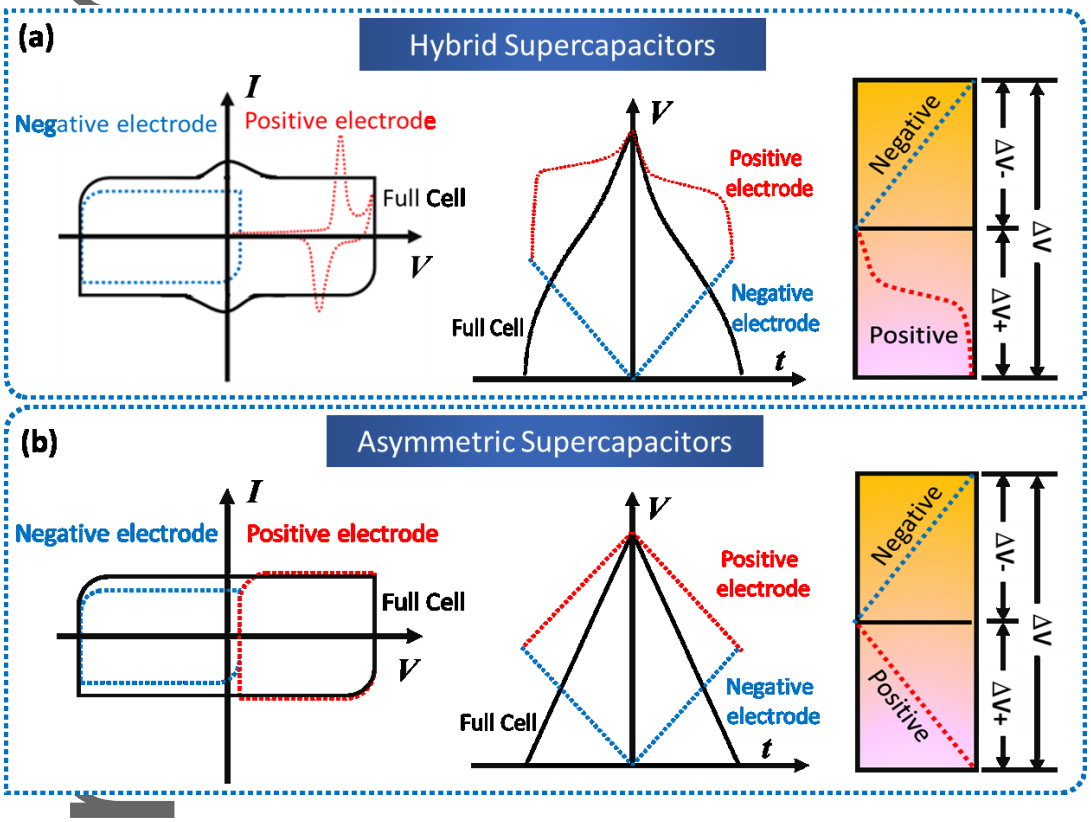

Figure 3. Comparison of the electrochemical signature for a typical (a) hybrid and (b) asymmetric supercapacitors with electrochemical features of their corresponding electrodes.

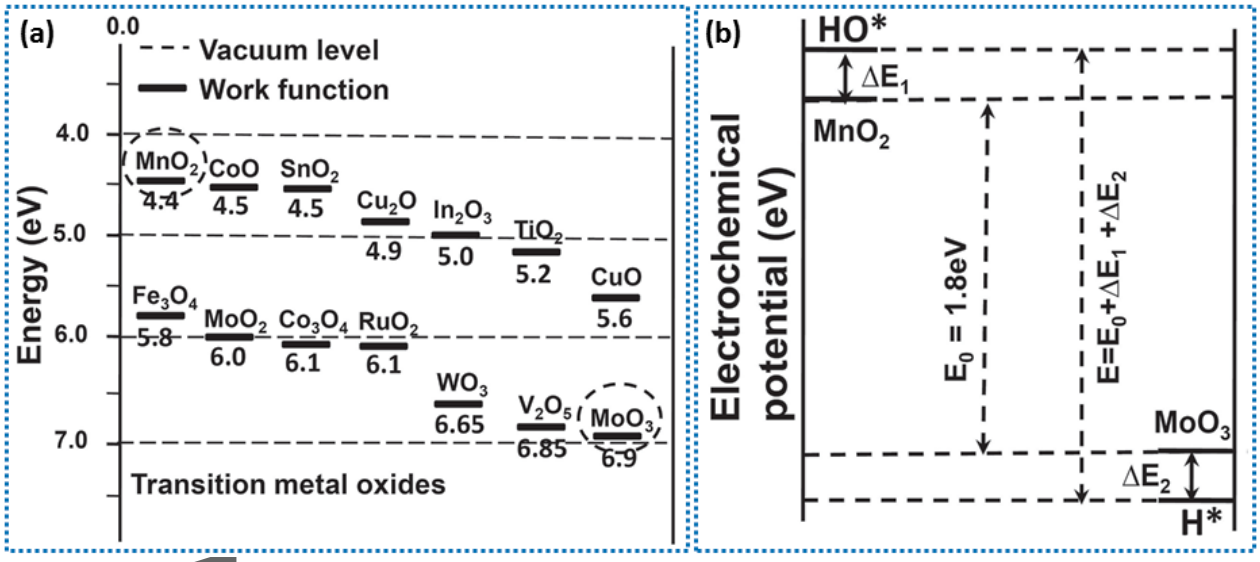

Figure 4. (a) Schematic illustration of work function of different metal oxides. (b) Relationship between potential window and the shift of work function (electrochemical potential) of two electrodes during charging. Reprinted with the permission from Ref.[89], Copyright, 2013 Wiley-VCH Verlag GmbH & Co. KGaA, Weinheim.

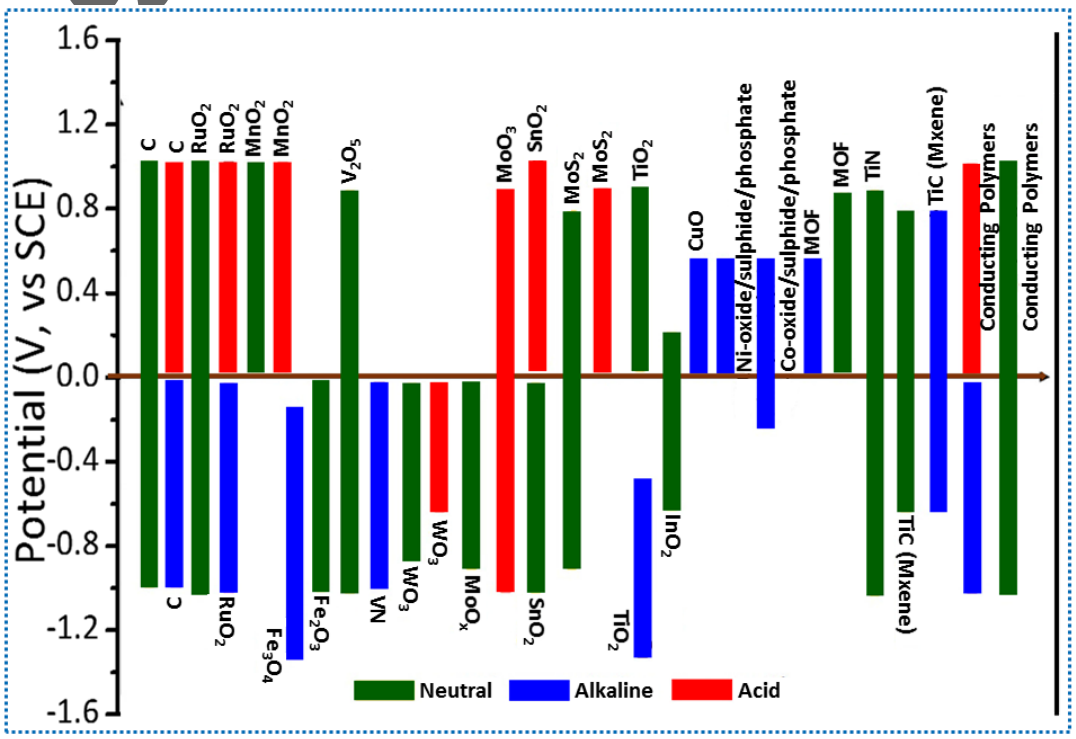

Figure 5. Potential window of various electrode materials in aqueous electrolyte.

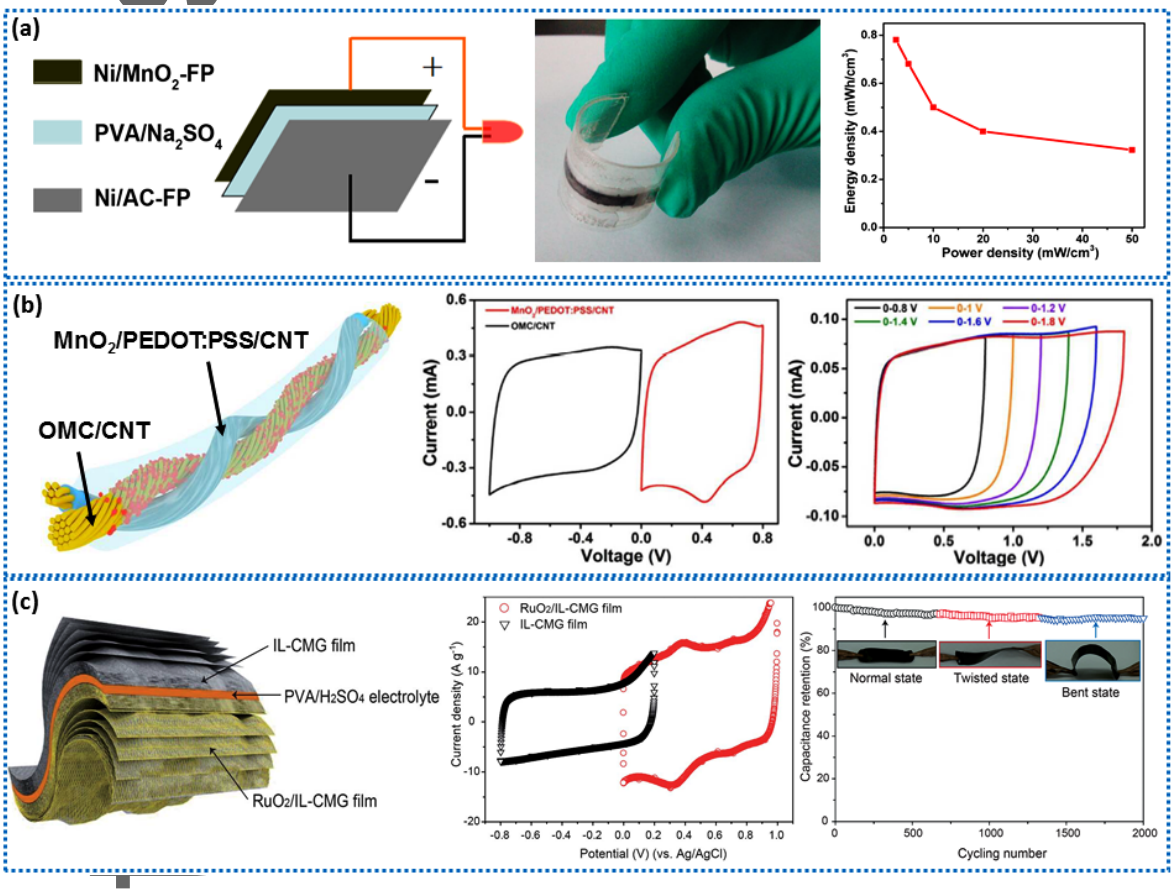

Figure 6. (a) Schematic illustration for the Ni/MnO_2-FP//Ni/AC−FP ASSC device. Digital photograph of Ni/MnO_2-FP//Ni/AC-FP device in a bent state. Relation curve of energy density and power density of Ni/MnO_2-FP//Ni/AC-FP ASSC. Reproduced with the permission from Ref.[101], Copyright, 2015, American Chemical Society. (b) Schematic illustration of the fabrication of fiber-shaped MnO_2/PEDOT:PSS/CNT//OMC/CNTs ASSC. Comparative CV curves of OMC/CNT and MnO_2/PEDOT:PSS/CNT electrodes at 20 mV/s. CV curves measured at different operating voltages at a constant scan rate of 20 mV/s. Reproduced with the permission from Ref.[112], Copyright, 2016, American Chemical Society.

(c) Pictorial diagram of IL-CMG//RuO_2/IL-CMG all-solid-state ASSC. Comparative CV curves recorded for IL-CMG and RuO_2-ILCMG films in 1 M H_2SO_4 solution at 50 mV/s. Cycling stability of IL-CMG//RuO_2/IL-CMG devices under normal, twisted, and bent states at 1 A/g over 2000 cycles. Reproduced with the permission from Ref.[123], Copyright, 2012, The Royal Society of Chemistry.

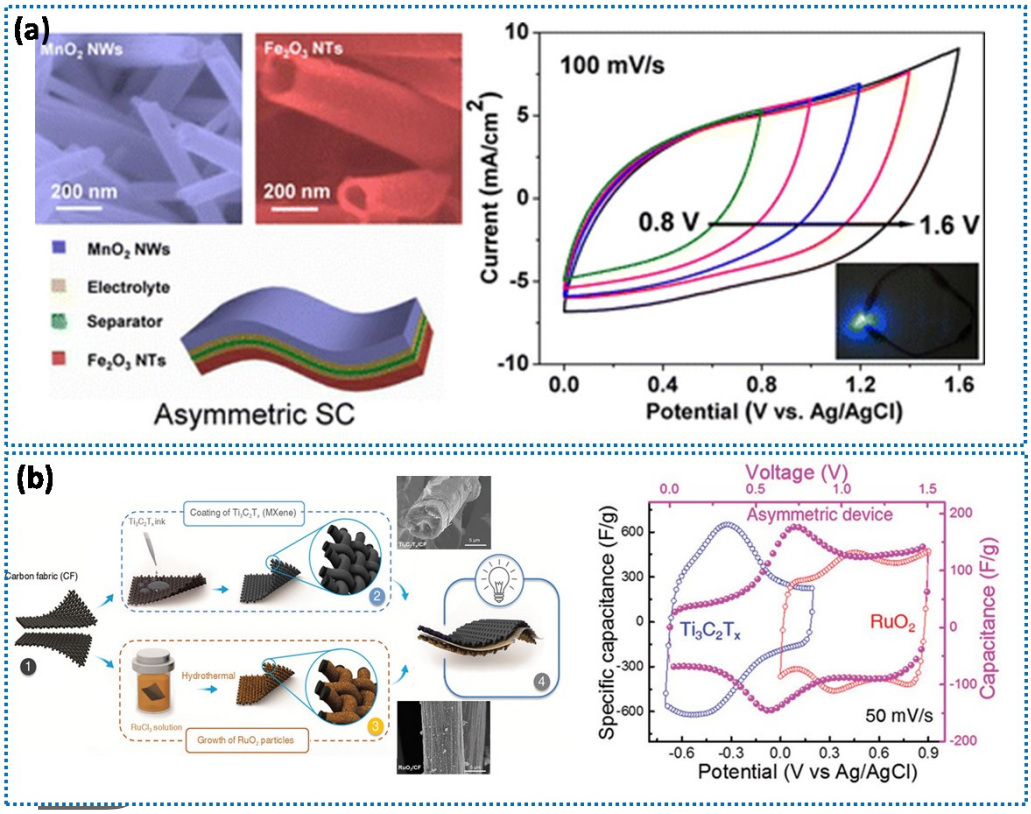

Figure 7 (a) SEM images of α-MnO_2 nanowires and amorphous Fe_2O_3 nanotubes grown on flexible carbon fabric. Schematic diagram α-MnO_2//Fe_2O_3 ASSC. CV curves of the assembled solid-state ASSC device collected in different scan voltage windows, inset shows a blue LED powered by the tandem ASSC devices. Reproduced with the permission from Ref.[130], Copyright, 2014, American Chemical Society. (b) Schematic representation of the fabrication process of $Ti_3C_2T_x$/CF//RuO_2/CF ASSC. CVs curves of RuO_2/CF, $Ti_3C_2T_x$/CF,

and the $Ti_3C_2T_x$/CF//RuO_2/CF ASSC at a scan rate of 50 mV/s. Reproduced with the permission from Ref.[147], Copyright, 2018 Wiley-VCH Verlag GmbH & Co. KGaA, Weinheim.

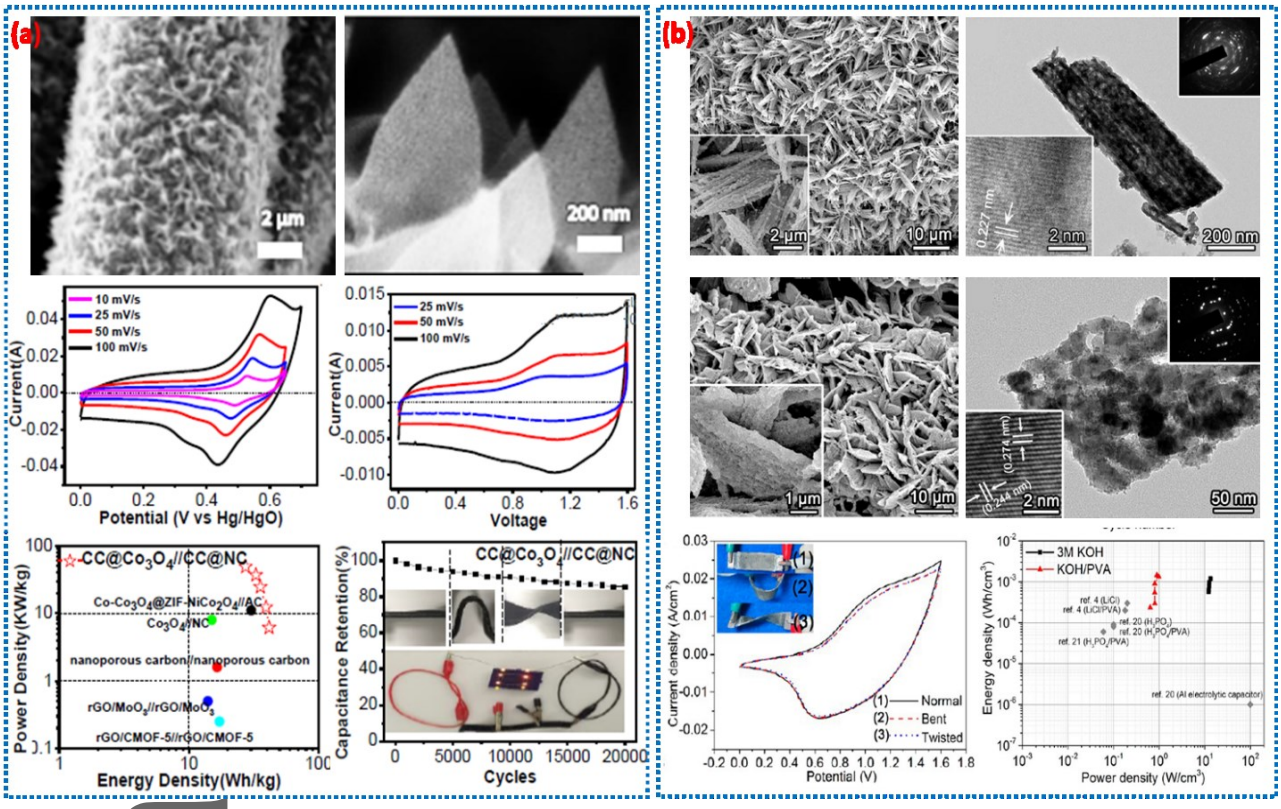

Figure 8 (a) SEM images of Co_3O_4 nanosheets deposited on carbon cloth (CC). CV curves of CC@Co_3O_4 with three electrode configurations in KOH electrolyte. Ragone plots and cycling test result of the CC@Co_3O_4//CC@NC HSSC with PVA-KOH gel electrolyte, inset shows digital images of the flat, bent, and twisted states of the cell during cycling test (upper) and a demo that three full cells can light up 8 orange LEDs. Reproduced with the permission from Ref.[192], Copyright, 2017, The Royal Society of Chemistry. (b) SEM and TEM images of Co_9S_8 nanorod arrays and Co_3O_4@RuO_2 nanosheet arrays on woven carbon fabrics. CV curves collected at the scan rate of 100 mV/s for the Co_9S_8//Co_3O_4@RuO_2 solid-state HSSC under normal, bent, and twisted conditions. Insets are the device photographs under different test conditions. Ragone plots of liquid and solid-state electrolyte based Co_9S_8//Co_3O_4@RuO_2 HSSC devices. Reproduced with the permission from Ref.[195], Copyright, 2013, American Chemical Society.

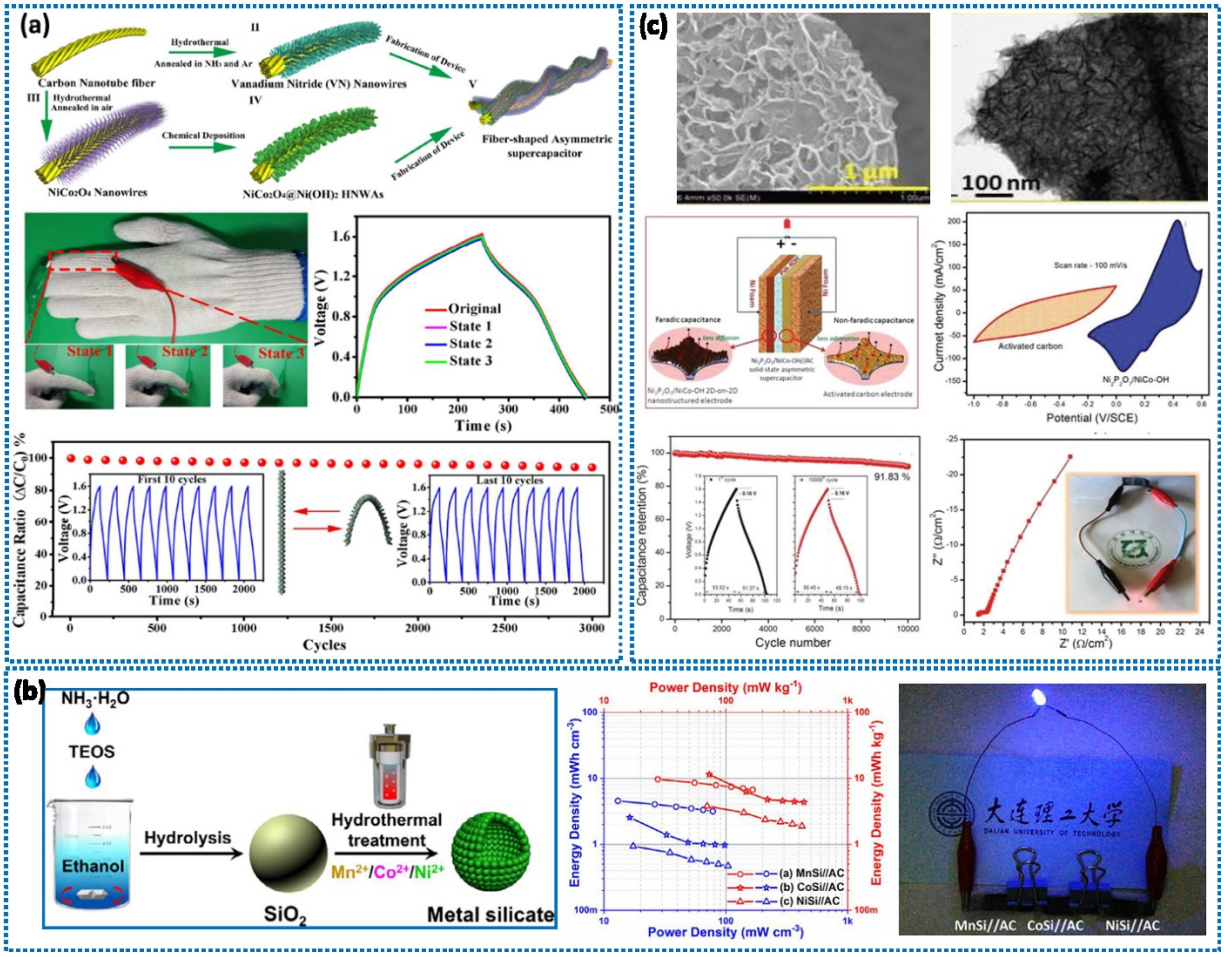

Figure 9 (a) Schematic illustration of the fabrication process for VN/CNTF and $NiCo_2O_4$@$Ni(OH)_2$/CNTF HSSC device. Optical images of a FACS woven into a glove. GCD curves obtained at different bending states corresponding to images. Cycle stability tested at 90° bending states corresponding to images in the inset. Reprinted with the permission from Ref.[207], Copyright, 2018, American Chemical Society. (b) Schematic illustration of the synthesis procedure of metal silicate. The Ragone plot (power density to energy density) of the metal silicate based HSSC devices. An LED is powered by MnSi//AC, CoSi//AC and NiSi//AC devices connected in series. Reproduced with the permission from Ref.[237], Copyright 2019, Elsevier. (c) SEM and TEM images of $Ni_2P_2O_7$/NiCo-OH 2D-on-2D nanostructured materials. The schematic of the assembled $Ni_2P_2O_7$/NiCo-OH//AC solid-state HSSC. CV curves for the $Ni_2P_2O_7$/NiCo-OH and activated carbon electrode at 100 V/s scan rate. Capacitance retention for the $Ni_2P_2O_7$/NiCo-OH//AC solid-state HSSC, inset shows the initial and final GCD cycles. Nyquist plot for the $Ni_2P_2O_7$/NiCo-OH//AC device, inset sows

the actual demonstration of the $Ni_2P_2O_7$/NiCo-OH//AC solid-state HSSC. Reproduced with the permission from Ref.[239], 2019 WILEY-VCH Verlag GmbH & Co. KGaA, Weinheim.

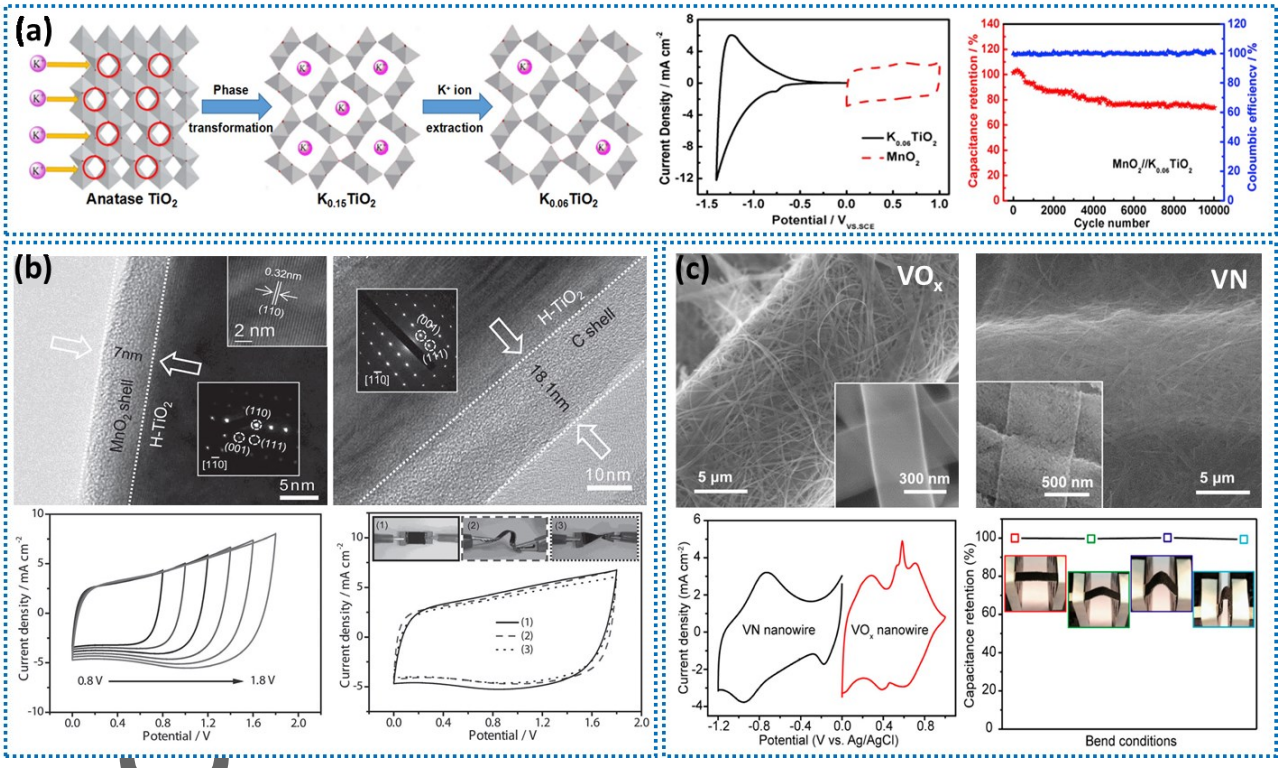

Figure 10 (a) Schematic of the phase transformation from anatase TiO_2 to hollandite K_xTiO_2 via the intercalation of K^+ ions at high temperature hydrothermal condition. CV curves of the $K_{0.06}TiO_2$ and MnO_2 electrodes at 5 mV/s in the 5 M LiCl electrolyte. Cycling performance and Coulombic efficiencies at different cycles of the all-solid-state MnO_2//$K_{0.06}TiO_2$ ASSC at the current density of 5 mA/cm^2. Reproduced with the permission from Ref.[273], Copyright 2019, Elsevier. (b) TEM images of H-TiO_2@MnO_2 and H-TiO_2@C NWs with corresponding SAED patterns. CV curves of the H-TiO_2@MnO_2//H-TiO_2@C HSSC collected in different scan voltage windows. CV curves collected at a scan rate of 100 mV/s for the HSSC device under flat, bent, and twisted conditions with the pictures under test conditions. Reproduced with the permission from Ref.[255], Copyright, 2013 Wiley-VCH Verlag GmbH & Co. KGaA, Weinheim. (c) SEM images of VOx and VN nanowires grown on carbon cloth with corresponding magnified SEM images (inset). CV curves collected for VN and VOx nanowire electrodes at 10 mV/s scan rate. Capacitance retention of the VOx//VN-HSSC

device measured at different bent conditions with their digital pictures. Reprinted with the permission from Ref.[261], Copyright, 2013, American Chemical Society.

References

1. C. Lethien, J. Le Bideau and T. Brousse, *Energy & Environmental Science*, 2019, **12**, 96-115.
2. D. P. Dubal, N. R. Chodankar, D. H. Kim and P. Gomez-Romero, *Chem Soc Rev*, 2018, **47**, 2065-2129.
3. F. Wang, X. Wu, X. Yuan, Z. Liu, Y. Zhang, L. Fu, Y. Zhu, Q. Zhou, Y. Wu and W. Huang, *Chem Soc Rev*, 2017, **46**, 6816-6854.
4. Y. Zheng, Y. Yang, S. Chen and Q. Yuan, *CrystEngComm*, 2016, **18**, 4218-4235.
5. P. Yang and W. Mai, *Nano Energy*, 2014, **8**, 274-290.
6. X. Lu, M. Yu, G. Wang, Y. Tong and Y. Li, *Energy & Environmental Science*, 2014, **7**.
7. H. Sun, Y. Zhang, J. Zhang, X. Sun and H. Peng, *Nature Reviews Materials*, 2017, **2**.
8. M. Beidaghi and Y. Gogotsi, *Energy & Environmental Science*, 2014, **7**.
9. M. Salanne, B. Rotenberg, K. Naoi, K. Kaneko, P. L. Taberna, C. P. Grey, B. Dunn and P. Simon, *Nature Energy*, 2016, **1**.
10. F. Bonaccorso, L. Colombo, G. Yu, M. Stoller, V. Tozzini, A. C. Ferrari, R. S. Ruoff and V. Pellegrini, *Science*, 2015, **347**, 1246501.
11. V. Augustyn, J. Come, M. A. Lowe, J. W. Kim, P. L. Taberna, S. H. Tolbert, H. D. Abruña, P. Simon and B. Dunn, *Nat Mater*, 2013, **12**, 518-522.
12. K. Naoi, S. Ishimoto, J.-i. Miyamoto and W. Naoi, *Energy & Environmental Science*, 2012, **5**.
13. X. Yu, S. Yun, J. S. Yeon, P. Bhattacharya, L. Wang, S. W. Lee, X. Hu and H. S. Park, *Advanced Energy Materials*, 2018, **8**.
14. C. Choi, D. S. Ashby, D. M. Butts, R. H. DeBlock, Q. Wei, J. Lau and B. Dunn, *Nature Reviews Materials*, 2019, **5**, 5-19.
15. T. Brousse, D. Bélanger and J. W. Long, *Journal of The Electrochemical Society*, 2015, **162**, A5185-A5189.
16. E. H. Masashi Okubo, Jedeok Kim, Masaya Enomoto, Norimichi Kojima, Tetsuichi Kudo, Haoshen Zhou, Itaru Honma, *Journal of American Chemical Society* 2007, **129**, 7444-7452.
17. M. R. Lukatskaya, S. Kota, Z. Lin, M.-Q. Zhao, N. Shpigel, M. D. Levi, J. Halim, P.-L. Taberna, M. W. Barsoum, P. Simon and Y. Gogotsi, *Nature Energy*, 2017, **2**.

18. M. K. Marketa Zukalova, Ladislav Kavan, Ivan Exnar, Michael Graetzel, *Chem. Mater.* , 2005, **17** 1248-1255.
19. Y. Jiang and J. Liu, *Energy & Environmental Materials*, 2019, **2**, 30-37.
20. H. Wang, A. C. Forse, J. M. Griffin, N. M. Trease, L. Trognko, P. L. Taberna, P. Simon and C. P. Grey, *J Am Chem Soc*, 2013, **135**, 18968-18980.
21. .
22. Y. Wang, Y. Song and Y. Xia, *Chem Soc Rev*, 2016, **45**, 5925-5950.
23. G. Wang, L. Zhang and J. Zhang, *Chem Soc Rev*, 2012, **41**, 797-828.
24. J. W. Long, D. Bélanger, T. Brousse, W. Sugimoto, M. B. Sassin and O. Crosnier, *MRS Bulletin*, 2011, **36**, 513-522.
25. F. Shi, L. Li, X.-l. Wang, C.-d. Gu and J.-p. Tu, *RSC Adv.*, 2014, **4**, 41910-41921.
26. C. Cougnon, E. Lebègue and G. Pognon, *Journal of Power Sources*, 2015, **274**, 551-559.
27. F. Ma, S. Ding, H. Ren and Y. Liu, *RSC Advances*, 2019, **9**, 2474-2483.
28. Z. Fan, J. Yan, T. Wei, L. Zhi, G. Ning, T. Li and F. Wei, *Advanced Functional Materials*, 2011, **21**, 2366-2375.
29. Y.-M. Chang, C.-Y. Wu and P.-W. Wu, *Journal of Power Sources*, 2013, **223**, 147-154.
30. X. Lu, J. Shen, H. Ma, B. Yan, Z. Li, M. Shi and M. Ye, *Journal of Power Sources*, 2012, **201**, 340-346.
31. J. Guo, Q. Zhang, Q. Li, J. Sun, C. Li, B. He, Z. Zhou, L. Xie, M. Li and Y. Yao, *ACS Appl Mater Interfaces*, 2018, **10**, 29705-29711.
32. H.-F. Ju, W.-L. Song and L.-Z. Fan, *J. Mater. Chem. A*, 2014, **2**, 10895-10903.
33. D. P. Dubal, N. R. Chodankar, Z. Caban-Huertas, F. Wolfart, M. Vidotti, R. Holze, C. D. Lokhande and P. Gomez-Romero, *Journal of Power Sources*, 2016, **308**, 158-165.
34. X. Fan, Z. Peng, Y. Yang, H. Zhou and X. Guo, *Journal of Materials Chemistry A*, 2015, **3**, 10077-10084.
35. C. Choi, J. A. Lee, A. Y. Choi, Y. T. Kim, X. Lepro, M. D. Lima, R. H. Baughman and S. J. Kim, *Adv Mater*, 2014, **26**, 2059-2065.
36. W. Li, F. Zhang, Y. Dou, Z. Wu, H. Liu, X. Qian, D. Gu, Y. Xia, B. Tu and D. Zhao, *Advanced Energy Materials*, 2011, **1**, 382-386.
37. K. Jost, D. Stenger, C. R. Perez, J. K. McDonough, K. Lian, Y. Gogotsi and G. Dion, *Energy & Environmental Science*, 2013, **6**.
38. J. Ren, W. Bai, G. Guan, Y. Zhang and H. Peng, *Adv Mater*, 2013, **25**, 5965-5970.
39. L. L. Zhang, X. Zhao, H. Ji, M. D. Stoller, L. Lai, S. Murali, S. McDonnell, B. Cleveger, R. M. Wallace and R. S. Ruoff, *Energy & Environmental Science*, 2012, **5**.
40. Z. S. Wu, K. Parvez, X. Feng and K. Mullen, *Nat Commun*, 2013, **4**, 2487.
41. B. Nagar, D. P. Dubal, L. Pires, A. Merkoci and P. Gomez-Romero, *ChemSusChem*, 2018, **11**, 1849-1856.
42. M. Oschatz, L. Borchardt, K. Pinkert, S. Thieme, M. R. Lohe, C. Hoffmann, M. Benusch, F. M. Wisser, C. Ziegler, L. Giebeler, M. H. Rümmeli, J. Eckert, A. Eychmüller and S. Kaskel, *Advanced Energy Materials*, 2014, **4**.
43. K. Pinkert, M. Oschatz, L. Borchardt, M. Klose, M. Zier, W. Nickel, L. Giebeler, S. Oswald, S. Kaskel and J. Eckert, *ACS Appl Mater Interfaces*, 2014, **6**, 2922-2928.
44. P. Huang, M. Heon, D. Pech, M. Brunet, P.-L. Taberna, Y. Gogotsi, S. Lofland, J. D. Hettinger and P. Simon, *Journal of Power Sources*, 2013, **225**, 240-244.
45. V. Augustyn, P. Simon and B. Dunn, *Energy & Environmental Science*, 2014, **7**.
46. T. Brousse, M. Toupin, R. Dugas, L. Athouël, O. Crosnier and D. Bélanger, *Journal of The Electrochemical Society*, 2006, **153**.

47. G. B. Sergio Trasatti, *Journal of Electroanalytical Chemistry and Interfacial Electrochemistry*, 1971, **29**.
48. M. Huang, F. Li, F. Dong, Y. X. Zhang and L. L. Zhang, *Journal of Materials Chemistry A*, 2015, **3**, 21380-21423.
49. K. Zhang, X. Han, Z. Hu, X. Zhang, Z. Tao and J. Chen, *Chem Soc Rev*, 2015, **44**, 699-728.
50. H. T. Tan, W. Sun, L. Wang and Q. Yan, *ChemNanoMat*, 2016, **2**, 562-577.
51. S. Devaraj and N. Munichandraiah, *J Phys Chem C*, 2008, **112**, 4406-4417.
52. C. Choi, J. H. Kim, H. J. Sim, J. Di, R. H. Baughman and S. J. Kim, *Advanced Energy Materials*, 2017, **7**.
53. L. Cao, J. Zhu, Y. Li, P. Xiao, Y. Zhang, S. Zhang and S. Yang, *J. Mater. Chem. A*, 2014, **2**, 13136-13142.
54. Q. Ke, C. Guan, X. Zhang, M. Zheng, Y. W. Zhang, Y. Cai, H. Zhang and J. Wang, *Adv Mater*, 2017, **29**.
55. P. Yu, Z. Zhang, L. Zheng, F. Teng, L. Hu and X. Fang, *Advanced Energy Materials*, 2016, **6**.
56. T. Brezesinski, J. Wang, S. H. Tolbert and B. Dunn, *Nat Mater*, 2010, **9**, 146-151.
57. Y. G. Patrice Simon, Bruce Dunn *Science*, 2014, **343**, 1210.
58. A. L. Brisse, P. Stevens, G. Toussaint, O. Crosnier and T. Brousse, *Materials (Basel)*, 2018, **11**.
59. H. B. Li, M. H. Yu, F. X. Wang, P. Liu, Y. Liang, J. Xiao, C. X. Wang, Y. X. Tong and G. W. Yang, *Nat Commun*, 2013, **4**, 1894.
60. Z. Chen, V. Augustyn, J. Wen, Y. Zhang, M. Shen, B. Dunn and Y. Lu, *Adv Mater*, 2011, **23**, 791-795.
61. M. R. Gao, Y. F. Xu, J. Jiang and S. H. Yu, *Chem Soc Rev*, 2013, **42**, 2986-3017.
62. X. Huang, Z. Zeng and H. Zhang, *Chem Soc Rev*, 2013, **42**, 1934-1946.
63. X. Cao, C. Tan, X. Zhang, W. Zhao and H. Zhang, *Adv Mater*, 2016, **28**, 6167-6196.
64. Y. Liu, Y. Li, H. Kang, T. Jin and L. Jiao, *Materials Horizons*, 2016, **3**, 402-421.
65. X. Zhang, L. Hou, A. Ciesielski and P. Samorì, *Advanced Energy Materials*, 2016, **6**.
66. W. G. P. T. C. Liu, B. E. Conway, *J. Electrochem. Soc.*, 1998, **145**, 1882.
67. D. C. W. K. B. E. Conway, *J. Electrochem. Soc.: Electrochemmical Science and Technology*, 1987, **134**, 906.
68. H. Shao, Z. Lin, K. Xu, P.-L. Taberna and P. Simon, *Energy Storage Materials*, 2019, **18**, 456-461.
69. J. Wang, J. Polleux, J. Lim and B. Dunn, *J Phys Chem C*, 2007, **111**, 14925-14931.
70. P. Yu, C. Li and X. Guo, *The Journal of Physical Chemistry C*, 2014, **118**, 10616-10624.
71. D. Chao, P. Liang, Z. Chen, L. Bai, H. Shen, X. Liu, X. Xia, Y. Zhao, S. V. Savilov, J. Lin and Z. X. Shen, *ACS Nano*, 2016, **10**, 10211-10219.
72. C. Yang, J. Feng, F. Lv, J. Zhou, C. Lin, K. Wang, Y. Zhang, Y. Yang, W. Wang, J. Li and S. Guo, *Adv Mater*, 2018, **30**, e1800036.
73. W. N. KATSUHIKO NAOI, SHINTARO AOYAGI, JUN-ICHI MIYAMOTO, TAKEO KAMINO, 2013, **46**, 1075–1083.
74. M. R. Lukatskaya, B. Dunn and Y. Gogotsi, *Nat Commun*, 2016, **7**, 12647.
75. L. Shi, C. Pang, S. Chen, M. Wang, K. Wang, Z. Tan, P. Gao, J. Ren, Y. Huang, H. Peng and Z. Liu, *Nano Lett*, 2017, **17**, 3681-3687.
76. Y. Jin, S. Li, A. Kushima, X. Zheng, Y. Sun, J. Xie, J. Sun, W. Xue, G. Zhou, J. Wu, F. Shi, R. Zhang, Z. Zhu, K. So, Y. Cui and J. Li, *Energy & Environmental Science*, 2017, **10**, 580-592.

77. J. Wang, Y. Cui and D. Wang, *Adv Mater*, 2018, DOI: 10.1002/adma.201801993, e1801993.
78. Y. Liu, N. Zhang, C. Yu, L. Jiao and J. Chen, *Nano Lett*, 2016, **16**, 3321-3328.
79. Q. Xu, J. K. Sun, G. Li, J. Y. Li, Y. X. Yin and Y. G. Guo, *Chem Commun (Camb)*, 2017, **53**, 12080-12083.
80. X. Wang, Y. Liu, Y. Wang and L. Jiao, *Small*, 2016, **12**, 4865-4872.
81. D. P. Dubal, N. R. Chodankar, A. Vinu, D. H. Kim and P. Gomez-Romero, *Chemsuschem*, 2017, **10**, 2742-2750.
82. D. P. Dubal, N. R. Chodankar, G. S. Gund, R. Holze, C. D. Lokhande and P. Gomez-Romero, *Energy Technology*, 2015, **3**, 168-176.
83. D. P. Dubal, R. Holze and P. Gomez-Romero, *Sci Rep*, 2014, **4**, 7349.
84. Y. Shao, M. F. El-Kady, J. Sun, Y. Li, Q. Zhang, M. Zhu, H. Wang, B. Dunn and R. B. Kaner, *Chem Rev*, 2018, **118**, 9233-9280.
85. A. Singh and A. Chandra, *Sci Rep*, 2015, **5**, 15551.
86. J. Cheng and M. Sprik, *Phys Chem Chem Phys*, 2012, **14**, 11245-11267.
87. , 1986.
88. C. A. Pan and T. P. Ma, *Applied Physics Letters*, 1980, **37**, 714-716.
89. J. Chang, M. Jin, F. Yao, T. H. Kim, V. T. Le, H. Yue, F. Gunes, B. Li, A. Ghosh, S. Xie and Y. H. Lee, *Advanced Functional Materials*, 2013, **23**, 5074-5083.
90. M. T. Greiner, M. G. Helander, W. M. Tang, Z. B. Wang, J. Qiu and Z. H. Lu, *Nat Mater*, 2011, **11**, 76-81.
91. Z. Viskadourakis, M. L. Paramês, O. Conde, M. Zervos and J. Giapintzakis, *Applied Physics Letters*, 2012, **101**.
92. J. Sun, C. Wu, X. Sun, H. Hu, C. Zhi, L. Hou and C. Yuan, *Journal of Materials Chemistry A*, 2017, **5**, 9443-9464.
93. F. Beguin, V. Presser, A. Balducci and E. Frackowiak, *Adv Mater*, 2014, **26**, 2219-2251, 2283.
94. Z. Yu, L. Tetard, L. Zhai and J. Thomas, *Energy & Environmental Science*, 2015, **8**, 702-730.
95. L. L. Zhang and X. S. Zhao, *Chem Soc Rev*, 2009, **38**, 2520-2531.
96. , 2000.
97. E. Raymundo-Piñero, K. Kierzek, J. Machnikowski and F. Béguin, *Carbon*, 2006, **44**, 2498-2507.
98. P. Z. Qunting Qu, Bin Wang, Yuhui Chen, Shu Tian, Yuping Wu, Rudolf Holze, 2009.
99. Z. Wen, W. She, Y. Li and R. Che, *J. Mater. Chem. A*, 2014, **2**, 20729-20738.
100. D. P. Dubal, J. G. Kim, Y. Kim, R. Holze and W. B. Kim, *Energy Technology*, 2013, **1**, 125-130.
101. L. Zhang, P. Zhu, F. Zhou, W. Zeng, H. Su, G. Li, J. Gao, R. Sun and C. P. Wong, *ACS Nano*, 2016, **10**, 1273-1282.
102. J. Tao, N. Liu, L. Li, J. Su and Y. Gao, *Nanoscale*, 2014, **6**, 2922-2928.
103. D. P. Dubal and P. Gomez-Romero, *Materials Today Energy*, 2018, **8**, 109-117.
104. C. Niu, E. K. Sichel, R. Hoch, D. Moy and H. Tennent, *Applied Physics Letters*, 1997, **70**, 1480-1482.
105. H. Pan, J. Li and Y. Feng, *Nanoscale Res Lett*, 2010, **5**, 654-668.
106. R. A. Fisher, M. R. Watt and W. Jud Ready, *ECS Journal of Solid State Science and Technology*, 2013, **2**, M3170-M3177.
107. B. Kim, H. Chung and W. Kim, *Nanotechnology*, 2012, **23**, 155401.

108. M. Saghafi, F. Mahboubi, S. Mohajerzadeh and R. Holze, *Synthetic Metals*, 2014, **195**, 252-259.
109. Y. J. Kang, H. Chung and W. Kim, *Synthetic Metals*, 2013, **166**, 40-44.
110. J. Tao, N. Liu, W. Ma, L. Ding, L. Li, J. Su and Y. Gao, *Sci Rep*, 2013, **3**, 2286.
111. F. Su and M. Miao, *Nanotechnology*, 2014, **25**, 135401.
112. X. Cheng, J. Zhang, J. Ren, N. Liu, P. Chen, Y. Zhang, J. Deng, Y. Wang and H. Peng, *The Journal of Physical Chemistry C*, 2016, **120**, 9685-9691.
113. K. S. Novoselov, V. I. Fal'ko, L. Colombo, P. R. Gellert, M. G. Schwab and K. Kim, *Nature*, 2012, **490**, 192-200.
114. M. F. El-Kady, V. Strong, S. Dubin and R. B. Kaner, *Science*, 2012, **335**, 1326-1330.
115. S. Stankovich, D. A. Dikin, G. H. Dommett, K. M. Kohlhaas, E. J. Zimney, E. A. Stach, R. D. Piner, S. T. Nguyen and R. S. Ruoff, *Nature*, 2006, **442**, 282-286.
116. J. M. Héctor A. Becerril, Zunfeng Liu, Randall M. Stoltenberg, Zhenan Bao, Yongsheng Chen, 2008.
117. A. G. Pandolfo and A. F. Hollenkamp, *Journal of Power Sources*, 2006, **157**, 11-27.
118. Z. Pan, Y. Qiu, J. Yang, F. Ye, Y. Xu, X. Zhang, M. Liu and Y. Zhang, *Nano Energy*, 2016, **26**, 610-619.
119. H. Jiang, P. S. Lee and C. Li, *Energy Environ. Sci.*, 2013, **6**, 41-53.
120. Y. Shao, H. Wang, Q. Zhang and Y. Li, *J. Mater. Chem. C*, 2013, **1**, 1245-1251.
121. G. L. Jie Yang, Zhenghui Pan, Meinan Liu, Yuan Hou, Yijun Xu, Xinluo Zhao, Hong Deng, LeiMei Sheng, Yongcai Qiu, and Yuegang Zhang, *ACS Appl. Mater. Interfaces*, 2015, **40**, 22172-22180.
122. H. Gao, F. Xiao, C. B. Ching and H. Duan, *ACS Appl Mater Interfaces*, 2012, **4**, 7020-7026.
123. B. G. Choi, S. J. Chang, H. W. Kang, C. P. Park, H. J. Kim, W. H. Hong, S. Lee and Y. S. Huh, *Nanoscale*, 2012, **4**, 4983-4988.
124. Y. Liu, X. Xu, Z. Shao and S. P. Jiang, *Energy Storage Materials*, 2020, **26**, 1-22.
125. D. Tian, X. Lu, Y. Zhu, M. Li and C. Wang, *Journal of Power Sources*, 2019, **413**, 50-58.
126. Y. Zhao, C. Huang, Y. He, X. Wu, R. Ge, X. Zu, S. Li and L. Qiao, *Journal of Power Sources*, 2020, **456**.
127. R. Hou, G. S. Gund, K. Qi, P. Nakhanivej, H. Liu, F. Li, B. Y. Xia and H. S. Park, *Energy Storage Materials*, 2019, **19**, 212-241.
128. G. S. Gund, D. P. Dubal, N. R. Chodankar, J. Y. Cho, P. Gomez-Romero, C. Park and C. D. Lokhande, *Sci Rep*, 2015, **5**, 12454.
129. N. R. Chodankar, D. P. Dubal, A. C. Lokhande, A. M. Patil, J. H. Kim and C. D. Lokhande, *Sci Rep*, 2016, **6**, 39205.
130. P. Yang, Y. Ding, Z. Lin, Z. Chen, Y. Li, P. Qiang, M. Ebrahimi, W. Mai, C. P. Wong and Z. L. Wang, *Nano Lett*, 2014, **14**, 731-736.
131. X. Lu, T. Zhai, X. Zhang, Y. Shen, L. Yuan, B. Hu, L. Gong, J. Chen, Y. Gao, J. Zhou, Y. Tong and Z. L. Wang, *Advanced Materials*, 2012, **24**, 938-944.
132. Z. Yu, J. Moore, J. Calderon, L. Zhai and J. Thomas, *Small*, 2015, **11**, 5289-5295.
133. T. Gu and B. Wei, *Journal of Materials Chemistry A*, 2016, **4**, 12289-12295.
134. X. Lu, G. Wang, T. Zhai, M. Yu, S. Xie, Y. Ling, C. Liang, Y. Tong and Y. Li, *Nano Lett*, 2012, **12**, 5376-5381.
135. A. Achour, J. B. Ducros, R. L. Porto, M. Boujtita, E. Gautron, L. Le Brizoual, M. A. Djouadi and T. Brousse, *Nano Energy*, 2014, **7**, 104-113.
136. Y. Yue, P. Han, X. He, K. Zhang, Z. Liu, C. Zhang, S. Dong, L. Gu and G. Cui, *Journal of Materials Chemistry*, 2012, **22**.

137. K. Y. Yongcai Qiu, Shihe Yang, Limin Jin, Hong Deng, Weishan Li, *ACS Nano*, 2010, **4**, 6515–6526.
138. Y. X. Fang Tian, Hongxiu Du, Yingzhi Zhou, Chi Xia, Wei Wang *RSC Adv.*, 2014, **4**, 41856–41863.
139. C. Zhu, P. Yang, D. Chao, X. Wang, X. Zhang, S. Chen, B. K. Tay, H. Huang, H. Zhang, W. Mai and H. J. Fan, *Adv Mater*, 2015, **27**, 4566-4571.
140. M. Naguib, M. Kurtoglu, V. Presser, J. Lu, J. Niu, M. Heon, L. Hultman, Y. Gogotsi and M. W. Barsoum, *Adv Mater*, 2011, **23**, 4248-4253.
141. B. Anasori, M. R. Lukatskaya and Y. Gogotsi, *Nature Reviews Materials*, 2017, **2**.
142. V. M. Hong Ng, H. Huang, K. Zhou, P. S. Lee, W. Que, J. Z. Xu and L. B. Kong, *Journal of Materials Chemistry A*, 2017, **5**, 3039-3068.
143. J.-C. Lei, X. Zhang and Z. Zhou, *Frontiers of Physics*, 2015, **10**, 276-286.
144. Y. X. Babak Anasori, Majid Beidaghi, Jun Lu, Brian C. Hosler, Lars Hultman, Paul R. C. Kent, Yury Gogotsi, Michel W. Barsoum, *ACS Nano*, 2015, **9**, 9507–9516.
145. M. R. Lukatskaya, O. Mashtalir, C. E. Ren, Y. Dall'Agnese, P. Rozier, P. L. Taberna, M. Naguib, P. Simon, M. W. Barsoum and Y. Gogotsi, *Science*, 2013, **341**, 1502-1505.
146. M. Ghidiu, M. R. Lukatskaya, M. Q. Zhao, Y. Gogotsi and M. W. Barsoum, *Nature*, 2014, **516**, 78-81.
147. Q. Jiang, N. Kurra, M. Alhabeb, Y. Gogotsi and H. N. Alshareef, *Advanced Energy Materials*, 2018, **8**.
148. J. W. Park, D. Y. Lee, H. Kim, J. S. Hyeon, M. J. de Andrade, R. H. Baughman and S. J. Kim, *MRS Communications*, 2019, **9**, 114-121.
149. G. A. Snook, P. Kao and A. S. Best, *Journal of Power Sources*, 2011, **196**, 1-12.
150. Y. Zhang, H. Feng, X. Wu, L. Wang, A. Zhang, T. Xia, H. Dong, X. Li and L. Zhang, *International Journal of Hydrogen Energy*, 2009, **34**, 4889-4899.
151. C. Yang and D. Li, *Materials Letters*, 2015, **155**, 78-81.
152. S. Ghosh, T. Maiyalagan and R. N. Basu, *Nanoscale*, 2016, **8**, 6921-6947.
153. K. D. Fong, T. Wang and S. K. Smoukov, *Sustainable Energy & Fuels*, 2017, **1**, 1857-1874.
154. L. Fu, Q. Qu, R. Holze, V. V. Kondratiev and Y. Wu, *Journal of Materials Chemistry A*, 2019, **7**, 14937-14970.
155. R. Holze and Y. P. Wu, *Electrochimica Acta*, 2014, **122**, 93-107.
156. N. Kurra, R. Wang and H. N. Alshareef, *Journal of Materials Chemistry A*, 2015, **3**, 7368-7374.
157. X. F. Lu, X. Y. Chen, W. Zhou, Y. X. Tong and G. R. Li, *ACS Appl Mater Interfaces*, 2015, **7**, 14843-14850.
158. Y. Jin, H. Chen, M. Chen, N. Liu and Q. Li, *ACS Appl Mater Interfaces*, 2013, **5**, 3408-3416.
159. Z. Zhang, K. Chi, F. Xiao and S. Wang, *Journal of Materials Chemistry A*, 2015, **3**, 12828-12835.
160. H. Yang, H. Xu, M. Li, L. Zhang, Y. Huang and X. Hu, *ACS Appl Mater Interfaces*, 2016, **8**, 1774-1779.
161. Q. Zong, Q. Zhang, X. Mei, Q. Li, Z. Zhou, D. Li, M. Chen, F. Shi, J. Sun, Y. Yao and Z. Zhang, *ACS Appl Mater Interfaces*, 2018, **10**, 37233-37241.
162. Z. Fan, Y. Wang, Z. Xie, D. Wang, Y. Yuan, H. Kang, B. Su, Z. Cheng and Y. Liu, *Adv Sci (Weinh)*, 2018, **5**, 1800750.
163. S. Mallick, P. P. Jana and C. R. Raj, *ChemElectroChem*, 2018, **5**, 2348-2356.

164. G. Sun, X. Zhang, R. Lin, J. Yang, H. Zhang and P. Chen, *Angew Chem Int Ed Engl*, 2015, **54**, 4651-4656.
165. Z. Chen, L. Zheng, T. Zhu, Z. Ma, Y. Yang, C. Wei, L. Liu and X. Gong, *Advanced Electronic Materials*, 2019, **5**.
166. Z. Pan, J. Yang, Q. Zhang, M. Liu, Y. Hu, Z. Kou, N. Liu, X. Yang, X. Ding, H. Chen, J. Li, K. Zhang, Y. Qiu, Q. Li, J. Wang and Y. Zhang, *Advanced Energy Materials*, 2019, **9**.
167. Q. Zhang, X. Wang, Z. Pan, J. Sun, J. Zhao, J. Zhang, C. Zhang, L. Tang, J. Luo, B. Song, Z. Zhang, W. Lu, Q. Li, Y. Zhang and Y. Yao, *Nano Lett*, 2017, **17**, 2719-2726.
168. Z. Zhang, F. Xiao and S. Wang, *Journal of Materials Chemistry A*, 2015, **3**, 11215-11223.
169. W. Zilong, Z. Zhu, J. Qiu and S. Yang, *J. Mater. Chem. C*, 2014, **2**, 1331-1336.
170. J. Qin, S. Wang, F. Zhou, P. Das, S. Zheng, C. Sun, X. Bao and Z.-S. Wu, *Energy Storage Materials*, 2019, **18**, 397-404.
171. Z. Zhang, F. Xiao, J. Xiao and S. Wang, *Journal of Materials Chemistry A*, 2015, **3**, 11817-11823.
172. N. R. Chodankar, D. P. Dubal, G. S. Gund and C. D. Lokhande, *Energy Technology*, 2015, **3**, 625-631.
173. A. V. Shinde, N. R. Chodankar, V. C. Lokhande, A. C. Lokhande, T. Ji, J. H. Kim and C. D. Lokhande, *RSC Advances*, 2016, **6**, 58839-58843.
174. T. Chen, Y. Tang, Y. Qiao, Z. Liu, W. Guo, J. Song, S. Mu, S. Yu, Y. Zhao and F. Gao, *Sci Rep*, 2016, **6**, 23289.
175. A. S. I. Varakin, and V. Menukhov, *Pat. WO97/07518 and US patent 5,986,876*, 14 August, 1995.
176. L. Feng, Y. Zhu, H. Ding and C. Ni, *Journal of Power Sources*, 2014, **267**, 430-444.
177. H. Wang, W. Zhang, H. Chen and W. Zheng, *Science China Technological Sciences*, 2015, **58**, 1779-1798.
178. C. Yuan, X. Zhang, Q. Wu and B. Gao, *Solid State Ionics*, 2006, **177**, 1237-1242.
179. Y. V. T. Yining Hu, Daniel A. Scherson *Journal of Electroanalytical Chemistry* 1999, **468** 64–69.
180. J. X. Feng, S. H. Ye, X. F. Lu, Y. X. Tong and G. R. Li, *ACS Appl Mater Interfaces*, 2015, **7**, 11444-11451.
181. D. Ghosh, M. Mandal and C. K. Das, *Langmuir*, 2015, **31**, 7835-7843.
182. D. P. Dubal, G. S. Gund, C. D. Lokhande and R. Holze, *ACS Appl Mater Interfaces*, 2013, **5**, 2446-2454.
183. G. S. Gund, D. P. Dubal, S. S. Shinde and C. D. Lokhande, *ACS Appl Mater Interfaces*, 2014, **6**, 3176-3188.
184. Y. Jiao, W. Hong, P. Li, L. Wang and G. Chen, *Applied Catalysis B: Environmental*, 2019, **244**, 732-739.
185. C. Zhang, S. Wang, S. Tang, S. Wang, Y. Li and Y. Du, *Applied Surface Science*, 2018, **458**, 656-664.
186. J. C. Y. Lizhi Zhang, Maosong Mo, Ling Wu, Quan Li, Kwan Wai Kwong, *J Am Chem Soc*, 2004, **126**, 8116–8117.
187. L. L. Feng, G. Yu, Y. Wu, G. D. Li, H. Li, Y. Sun, T. Asefa, W. Chen and X. Zou, *J Am Chem Soc*, 2015, **137**, 14023-14026.
188. Z. Chen, L. Jin, W. Hao, W. Ren and H. M. Cheng, *Materials Today Nano*, 2019, **5**.
189. A. Ye, Y. Sui, J. Qi, F. Wei, Y. He, Q. Meng, Y. Ren and Z. Sun, *Journal of Electronic Materials*, 2018, **47**, 7002-7010.

190. Y. Wang, X. Lin, T. Liu, H. Chen, S. Chen, Z. Jiang, J. Liu, J. Huang and M. Liu, *Advanced Functional Materials*, 2018, **28**.
191. H. Pang, X. Li, Q. Zhao, H. Xue, W.-Y. Lai, Z. Hu and W. Huang, *Nano Energy*, 2017, **35**, 138-145.
192. C. Guan, W. Zhao, Y. Hu, Z. Lai, X. Li, S. Sun, H. Zhang, A. K. Cheetham and J. Wang, *Nanoscale Horizons*, 2017, **2**, 99-105.
193. S. Dai, Y. Yuan, J. Yu, J. Tang, J. Zhou and W. Tang, *Nanoscale*, 2018, **10**, 15454-15461.
194. X. Rui, H. Tan and Q. Yan, *Nanoscale*, 2014, **6**, 9889-9924.
195. Q. W. Jing Xu, Xiaowei Wang, Qingyi Xiang, Bo Liang, Di Chen, Guozhen Shen, *ACS Nano*, **7**, 5453-5462.
196. K. Zhao, Y. Wang, L. Han, Y. Wang, X. Luo, Z. Zhang and Y. Yang, *Nano-Micro Letters*, 2019, **11**.
197. N. Yu, M.-Q. Zhu and D. Chen, *Journal of Materials Chemistry A*, 2015, **3**, 7910-7918.
198. Z. Zheng, M. Retana, X. Hu, R. Luna, Y. H. Ikuhara and W. Zhou, *ACS Appl Mater Interfaces*, 2017, **9**, 16986-16994.
199. Z. Gao, N. Song and X. Li, *Journal of Materials Chemistry A*, 2015, **3**, 14833-14844.
200. J. Wen, B. Xu, J. Zhou and Y. Chen, *Journal of Power Sources*, 2018, **402**, 91-98.
201. D. Kong, C. Cheng, Y. Wang, J. I. Wong, Y. Yang and H. Y. Yang, *Journal of Materials Chemistry A*, 2015, **3**, 16150-16161.
202. D. P. Dubal, P. Gomez-Romero, B. R. Sankapal and R. Holze, *Nano Energy*, 2015, **11**, 377-399.
203. Y. Zhang, L. Li, H. Su, W. Huang and X. Dong, *Journal of Materials Chemistry A*, 2015, **3**, 43-59.
204. X. Liu, S. Shi, Q. Xiong, L. Li, Y. Zhang, H. Tang, C. Gu, X. Wang and J. Tu, *ACS Appl Mater Interfaces*, 2013, **5**, 8790-8795.
205. X. Wang, X. Han, M. Lim, N. Singh, C. L. Gan, M. Jan and P. S. Lee, *The Journal of Physical Chemistry C*, 2012, **116**, 12448-12454.
206. Z. Gao, W. Yang, J. Wang, N. Song and X. Li, *Nano Energy*, 2015, **13**, 306-317.
207. X. Wang, J. Sun, J. Zhao, Z. Zhou, Q. Zhang, C.-p. Wong and Y. Yao, *The Journal of Physical Chemistry C*, 2018, **123**, 985-993.
208. D. Kong, W. Ren, C. Cheng, Y. Wang, Z. Huang and H. Y. Yang, *ACS Appl Mater Interfaces*, 2015, **7**, 21334-21346.
209. C. Zhou, T. Gao, Y. Wang, Q. Liu, Z. Huang, X. Liu, M. Qing and D. Xiao, *Small*, 2019, **15**, e1803469.
210. J. Sun, P. Zan, L. Ye, X. Yang and L. Zhao, *Journal of Materials Chemistry A*, 2017, **5**, 9815-9823.
211. W. Ma, H. Nan, Z. Gu, B. Geng and X. Zhang, *Journal of Materials Chemistry A*, 2015, **3**, 5442-5448.
212. W. Xiao, J. S. Chen, C. M. Li, R. Xu and X. W. Lou, *Chemistry of Materials*, 2010, **22**, 746-754.
213. B. Liu, S. H. Yu, L. Li, Q. Zhang, F. Zhang and K. Jiang, *Angew Chem Int Ed Engl*, 2004, **43**, 4745-4750.
214. H. Gao, F. Wu, X. Wang, C. Hao and C. Ge, *International Journal of Hydrogen Energy*, 2018, **43**, 18349-18362.
215. Y. Chen, B. Liu, Q. Liu, J. Wang, Z. Li, X. Jing and L. Liu, *Nanoscale*, 2015, **7**, 15159-15167.

216. F. Lu, M. Zhou, K. Su, T. Ye, Y. Yang, T. D. Lam, Y. Bando and X. Wang, *ACS Appl Mater Interfaces*, 2019, **11**, 2082-2092.
217. Y. Zhao, X. He, R. Chen, Q. Liu, J. Liu, D. Song, H. Zhang, H. Dong, R. Li, M. Zhang and J. Wang, *Applied Surface Science*, 2018, **453**, 73-82.
218. C. Wang, Z. Guan, Y. Shen, S. Yu, X.-Z. Fu, R. Sun and C.-P. Wong, *Chemical Engineering Journal*, 2018, **346**, 193-202.
219. V. S. Kumbhar, N. R. Chodankar, K. Lee and D. H. Kim, *J Colloid Interface Sci*, 2019, **557**, 423-437.
220. S. G. Mohamed, I. Hussain and J. J. Shim, *Nanoscale*, 2018, **10**, 6620-6628.
221. S. Liu, Y. Yin, K. S. Hui, K. N. Hui, S. C. Lee and S. C. Jun, *Adv Sci (Weinh)*, 2018, **5**, 1800733.
222. M. Wei, C. Wang, Y. Yao, S. Yu, W.-H. Liao, J. Ren, R. Sun and C.-P. Wong, *Chemical Engineering Journal*, 2019, **355**, 891-900.
223. J. Song, Y. Chen, K. Cao, Y. Lu, J. H. Xin and X. Tao, *ACS Appl Mater Interfaces*, 2018, **10**, 39839-39850.
224. M. S. Javed, H. Lei, J. Li, Z. Wang and W. Mai, *Journal of Materials Chemistry A*, 2019, **7**, 17435-17445.
225. W. Sun, Y. Du, G. Wu, G. Gao, H. Zhu, J. Shen, K. Zhang and G. Cao, *Journal of Materials Chemistry A*, 2019, **7**, 7138-7150.
226. L. Su, C. Ma, T. Hou and W. Han, *RSC Advances*, 2013, **3**.
227. Y. Xiao, D. Su, X. Wang, S. Wu, L. Zhou, Z. Sun, Z. Wang, S. Fang and F. Li, *Electrochimica Acta*, 2017, **253**, 324-332.
228. F. He, Z. Hu, K. Liu, H. Guo, S. Zhang, H. Liu and Q. Xie, *Journal of Solid State Electrochemistry*, 2014, **19**, 607-617.
229. J. Xu, S. Gai, F. He, N. Niu, P. Gao, Y. Chen and P. Yang, *Dalton Trans*, 2014, **43**, 11667-11675.
230. X. Wang, H. Li, H. Li, S. Lin, J. Bai, J. Dai, C. Liang, X. Zhu, Y. Sun and S. Dou, *Journal of Materials Chemistry A*, 2019, **7**, 2291-2300.
231. X. Gao, X. Liu, D. Wu, B. Qian, Z. Kou, Z. Pan, Y. Pang, L. Miao and J. Wang, *Advanced Functional Materials*, 2019, DOI: 10.1002/adfm.201903879.
232. R. Zhao, M. Wang, D. Zhao, H. Li, C. Wang and L. Yin, *ACS Energy Letters*, 2017, **3**, 132-140.
233. A. Tyagi, M. Chandra Joshi, K. Agarwal, B. Balasubramaniam and R. K. Gupta, *Nanoscale Advances*, 2019, **1**, 2400-2407.
234. F. Wang, T. Wang, S. Sun, Y. Xu, R. Yu and H. Li, *Sci Rep*, 2018, **8**, 8908.
235. J. Zhao, M. Zheng, Z. Run, J. Xia, M. Sun and H. Pang, *Journal of Power Sources*, 2015, **285**, 385-392.
236. J. Zhao, S. Wang, Z. Run, G. Zhang, W. Du and H. Pang, *Particle & Particle Systems Characterization*, 2015, **32**, 880-885.
237. Q. Wang, Y. Zhang, H. Jiang, X. Li, Y. Cheng and C. Meng, *Chemical Engineering Journal*, 2019, **362**, 818-829.
238. N. R. Chodankar, G. S. Rama Raju, B. Park, P. A. Shinde, S. Chan Jun, D. P. Dubal, Y. S. Huh and Y.-K. Han, *Journal of Materials Chemistry A*, 2020, **8**, 5721-5733.
239. N. R. Chodankar, D. P. Dubal, S. H. Ji and D. H. Kim, *Small*, 2019, **15**, e1901145.
240. J. Liu, G. Shen, S. Zhao, X. He, C. Zhang, T. Jiang, J. Jiang and B. Chen, *Journal of Materials Chemistry A*, 2019, **7**, 8184-8193.
241. T. T. Nguyen, J. Balamurugan, V. Aravindan, N. H. Kim and J. H. Lee, *Chemistry of Materials*, 2019, **31**, 4490-4504.
242. Z.-B. Zhai, K.-J. Huang and X. Wu, *Nano Energy*, 2018, **47**, 89-95.

243. G. Ma, F. Hua, K. Sun, E. Fenga, H. Peng, Z. Zhang and Z. Lei, *R Soc Open Sci*, 2018, **5**, 171186.
244. B. Yang, A. Nie, Y. Chang, Y. Cheng, F. Wen, J. Xiang, L. Li, Z. Liu and Y. Tian, *Journal of Materials Chemistry A*, 2018, **6**, 19409-19416.
245. N. Zhang, Y. Li, J. Xu, J. Li, B. Wei, Y. Ding, I. Amorim, R. Thomas, S. M. Thalluri, Y. Liu, G. Yu and L. Liu, *ACS Nano*, 2019, **13**, 10612-10621.
246. T. T. Nguyen, J. Balamurugan, N. H. Kim and J. H. Lee, *Journal of Materials Chemistry A*, 2018, **6**, 8669-8681.
247. Y. Tang, Y. Li, W. Guo, J. Wang, X. Li, S. Chen, S. Mu, Y. Zhao and F. Gao, *Journal of Materials Chemistry A*, 2018, **6**, 623-632.
248. J. Cao, Y. Wang, Y. Zhou, J.-H. Ouyang, D. Jia and L. Guo, *Journal of Electroanalytical Chemistry*, 2013, **689**, 201-206.
249. W. Guo, Y. Li, Y. Tang, S. Chen, Z. Liu, L. Wang, Y. Zhao and F. Gao, *Electrochimica Acta*, 2017, **229**, 197-207.
250. P. Senguttuvan, G. Rousse, M. E. Arroyo y de Dompablo, H. Vezin, J. M. Tarascon and M. R. Palacin, *J Am Chem Soc*, 2013, **135**, 3897-3903.
251. C. S. J. Liam D. Noailles, John T. Vaughey, Michael M. Thackeray, 1999, **81**, 259–263.
252. Q. Zhang, Y. Wei, H. Yang, D. Su, Y. Ma, H. Li and T. Zhai, *ACS Appl Mater Interfaces*, 2017, **9**, 7009-7016.
253. R. Fang, K. Chen, L. Yin, Z. Sun, F. Li and H. M. Cheng, *Adv Mater*, 2019, **31**, e1800863.
254. X. Lu, M. Yu, G. Wang, T. Zhai, S. Xie, Y. Ling, Y. Tong and Y. Li, *Adv Mater*, 2013, **25**, 267-272.
255. X.-H. L. Longyan Yuan, Xu Xiao, Teng Zhai, Junjie Dai, Fengchao Zhang, Bin Hu, Xue Wang, Li Gong, Jian Chen, Chenguo Hu, Yexiang Tong, Jun Zhou, Zhong Lin Wang, 2012, **6**, 656–661.
256. C.-H. Yang, I. W. Sun, C.-T. Hsieh, T.-Y. Wu, C.-Y. Su, Y.-S. Li and J.-K. Chang, *Journal of Materials Chemistry A*, 2016, **4**, 4015-4018.
257. F. E. Michel Armand, Douglas R. MacFarlane,, Hiroyuki Ohno, Bruno Scrosati, *Nature Materials*, 2009, **8**, 621−629.
258. C. Zhong, Y. Deng, W. Hu, J. Qiao, L. Zhang and J. Zhang, *Chem Soc Rev*, 2015, **44**, 7484-7539.
259. X. Wang, B. Liu, R. Liu, Q. Wang, X. Hou, D. Chen, R. Wang and G. Shen, *Angew Chem Int Ed Engl*, 2014, **53**, 1849-1853.
260. M.-J. Deng, T.-H. Chou, L.-H. Yeh, J.-M. Chen and K.-T. Lu, *Journal of Materials Chemistry A*, 2018, **6**, 20686-20694.
261. X. Lu, M. Yu, T. Zhai, G. Wang, S. Xie, T. Liu, C. Liang, Y. Tong and Y. Li, *Nano Lett*, 2013, **13**, 2628-2633.
262. J. B. Cook, H.-S. Kim, T. C. Lin, C.-H. Lai, B. Dunn and S. H. Tolbert, *Advanced Energy Materials*, 2017, **7**.
263. C. Nagaraju, C. V. V. Muralee Gopi, J.-W. Ahn and H.-J. Kim, *New Journal of Chemistry*, 2018, **42**, 12357-12360.
264. H. Hwang, H. Kim and J. Cho, *Nano Lett*, 2011, **11**, 4826-4830.
265. Y. Liang, R. Feng, S. Yang, H. Ma, J. Liang and J. Chen, *Adv Mater*, 2011, **23**, 640-643.
266. S. S. Karade, D. P. Dubal and B. R. Sankapal, *RSC Adv.*, 2016, **6**, 39159-39165.
267. S. S. Karade, D. P. Dubal and B. R. Sankapal, *ChemistrySelect*, 2017, **2**, 10405-10412.

268. X. Yang, H. Niu, H. Jiang, Q. Wang and F. Qu, *Journal of Materials Chemistry A*, 2016, **4**, 11264-11275.
269. S. Liu, Y. Yin, M. Wu, K. S. Hui, K. N. Hui, C. Y. Ouyang and S. C. Jun, *Small*, 2019, **15**, e1803984.
270. N. R. Chodankar, S. J. Patil, G. S. Rama Raju, D. W. Lee, D. P. Dubal, Y. S. Huh and Y. K. Han, *ChemSusChem*, 2019, DOI: 10.1002/cssc.201902339.
271. S. Liu, Y. Zeng, M. Zhang, S. Xie, Y. Tong, F. Cheng and X. Lu, *J. Mater. Chem. A*, 2017, **5**, 21460-21466.
272. J. Zhang, J. Sun, Y. Hu, D. Wang and Y. Cui, *Journal of Alloys and Compounds*, 2019, **780**, 276-283.
273. D. Li, W. Guo, Y. Li, Y. Tang, J. Yan, X. Meng, M. Xia and F. Gao, *Journal of Power Sources*, 2019, **413**, 34-41.
274. F. Chen, H. Wang, S. Ji, V. Linkov and R. Wang, *Materials Today Energy*, 2019, **11**, 211-217.
275. N. R. Chodankar, D. P. Dubal, S. J. Patil, G. S. Rama Raju, S. V. Karekar, Y. S. Huh and Y.-K. Han, *Electrochimica Acta*, 2019, **319**, 435-443.
276. W. G. Wenru Zou, Xinyi Liu, Yunli Luo, Qinglan Ye, Xuetang Xu, Fan Wang, *Chem. Eur. J.* , 2018, **24**, 19309 – 19316.
277. J. Zhao, J. Chen, S. Xu, M. Shao, Q. Zhang, F. Wei, J. Ma, M. Wei, D. G. Evans and X. Duan, *Advanced Functional Materials*, 2014, **24**, 2938-2946.
278. C. Wei, C. Cheng, B. Zhou, X. Yuan, T. Cui, S. Wang, M. Zheng and H. Pang, *Particle & Particle Systems Characterization*, 2015, **32**, 831-839.
279. Y. Zhao, X. He, R. Chen, Q. Liu, J. Liu, J. Yu, J. Li, H. Zhang, H. Dong, M. Zhang and J. Wang, *Chemical Engineering Journal*, 2018, **352**, 29-38.
280. Y. Gao, J. Zhao, Z. Run, G. Zhang and H. Pang, *Dalton Trans*, 2014, **43**, 17000-17005.
281. H. Pang, Y. Zhang, W.-Y. Lai, Z. Hu and W. Huang, *Nano Energy*, 2015, **15**, 303-312.
282. X. He, Y. Zhao, R. Chen, H. Zhang, J. Liu, Q. Liu, D. Song, R. Li and J. Wang, *ACS Sustainable Chemistry & Engineering*, 2018, **6**, 14945-14954.
283. H. Gao, C. Hao, Y. Qi, J. Li, X. Wang, S. Zhou and C. Huang, *Journal of Alloys and Compounds*, 2018, **767**, 1048-1056.
284. Y. Zhang, M. Zheng, M. Qu, M. Sun and H. Pang, *Journal of Alloys and Compounds*, 2015, **651**, 214-221.
285. J. Li, C. Hao, S. Zhou, C. Huang and X. Wang, *Electrochimica Acta*, 2018, **283**, 467-477.
286. J. Balamurugan, C. Li, V. Aravindan, N. H. Kim and J. H. Lee, *Advanced Functional Materials*, 2018, **28**.
287. H. Xie, S. Tang, J. Zhu, S. Vongehr and X. Meng, *Journal of Materials Chemistry A*, 2015, **3**, 18505-18513.
288. L. Yue, H. Guo, X. Wang, T. Sun, H. Liu, Q. Li, M. Xu, Y. Yang and W. Yang, *J Colloid Interface Sci*, 2019, **539**, 370-378.
289. Y. Liu, N. Liu, L. Yu, X. Jiang and X. Yan, *Chemical Engineering Journal*, 2019, **362**, 600-608.
290. X. Wu, M. Lian and Q. Wang, *Electrochimica Acta*, 2019, **295**, 655-661.
291. A. M. Zardkhoshoui and S. S. H. Davarani, *Journal of Alloys and Compounds*, 2019, **773**, 527-536.
292. Y.-N. Liu, J.-N. Zhang, H.-T. Wang, X.-H. Kang and S.-W. Bian, *Materials Chemistry Frontiers*, 2019, **3**, 25-31.

293. Y. Liu, X. Wang, X. Jiang, X. Li and L. Yu, *Nanoscale*, 2018, **10**, 22848-22860.
294. W. Yan, J. Y. Kim, W. Xing, K. C. Donavan, T. Ayvazian and R. M. Penner, *Chemistry of Materials*, 2012, **24**, 2382-2390.

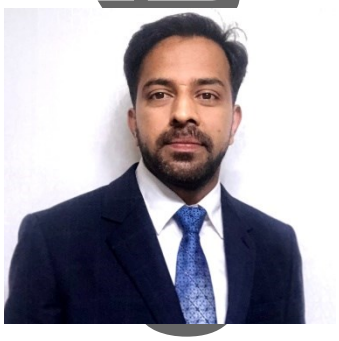

Dr. Nilesh R. Chodankar is currently working as Assistant Professor at Department of Energy and materials Engineering, Dongguk University, Seoul, South Korea. He received his PhD from Shivaji University, Kolhapur, India, in 2016 and joined as Post-doctoral researcher at Chonnam National University, South Korea. So far, Nilesh have co-authored more than 52 research articles and recived over 1700 citations with 'h' index of 22 and 'i10' index 33. His current research interests include the engineering of atomically thin 2D nanomaterials for energy storage devices including the supercapacitor and aqueous batteries.

Dr. Hong Duc Pham received his BSc degree in Chemical Engineering from Ho Chi Minh University of Technology, Vietnam. Subsequently, he earned his master degree from Pukyong National University, South Korea in 2013. He then received his Ph.D. from Queensland University of Technology (QUT), Australia. He is a recipient of Higher Achiever

Award from Science and Engineering Faculty, QUT for his excellent research performance during his PhD. Currently, he is working as Post-Doctoral Research Fellow with Dr. Deepak P. Dubal. His research interests is developing low-cost materials, biomass, biofuels and energy storage devices.

Dr. Deepak Dubal is working as Australian Future Fellow (Senior Lecturer) at Queensland University of Technology, Australia. He received his PhD in 2011 from Shivaji University Kolhapur, India and worked as Post-doctoral Fellow at GIST, South Korea. He is a recipient of Alexander von Humboldt (Germany), Marie Curie (Spain) and Vice Chancellor (Australia) Fellowships. He is recently appointed as visiting international professor at Mid Sweden University, Sweden and elected as Foreign Young Associate Fellow of Maharashtra Academy of Sciences (MASc). He is editorial board member of NPG-Scientific Reports and guest editor of several special issues. His research is emphasized on design and development of advanced materials for clean energy conversion and storage technologies with special focus on supercapacitors, lithium-ion batteries (LIBs), Biowaste and Recycling of Li-ion batteries.